Application of Ion Beam Methods in Biomedical Research

Quantitative Microscopy with Trace Element Sensitivity

Von der Fakultät für Physik und Geowissenschaften

der Universität Leipzig

genehmigte

DISSERTATION

zur Erlangung des akademischen Grades

Doctor rerum naturalium

Dr. rer. nat.

vorgelegt von

M. Sc. Nirav Dinkar Barapatre

geboren am 15.03.1982 in Ahmedabad

Gutachter: Prof. Dr. Tilman Butz
                        Prof. Dr. Philippe Moretto

Tag der Verleihung: 14. Oktober 2013

Bibliographic description

Barapatre, Nirav

Application of Ion Beam Methods in Biomedical Research - Quantitative Microscopy with Trace Element Sensitivity

Universität Leipzig, Dissertation
147 P., 125 Lit., 36 Fig.

Referat:

The figures of merit of nuclear microscopy are compared with the other spatially resolved techniques of chemical microanalysis. The significance of trace elements is the human body is discussed. The physical basis of the nuclear microscopy is explained and the technical setup of the ion beam laboratory LIPSION is described. A novel, non-interceptive, and non-blanking method of beam current monitoring is presented. The applications of nuclear microscopy in biomedical research range from neurobiology to cognitive sciences. The iron overload hypothesis in Parkinson's disease is investigated by a differential analysis of human substantia nigra. The trace element content is quantified in neuromelanin, in microglia cells, and in extraneuronal environment and a comparative study of six Parkinsonian cases with six control cases is presented. The electrolyte elements are quantified in various organs associated with the olfactory signalling in *Drosophila melanogaster*, namely the brain, the antenna and its sensilla hairs, the mouth parts, and the compound eye. The determination of spatially resolved element concentrations is useful in preparing the organ specific Ringer's solution, an artificial lymph that is used in disruptive neurobiological experiments. The role of trace elements in the progression of atherosclerosis is examined in a pilot study by differentially quantifying the element content in an induced murine atherosclerotic lesion. The high-definition quantitative elemental maps of large samples are generated by measuring in segments and at high beam current. The feasibility of generating a quantitative elemental rodent brain atlas by Large Area Mapping is investigated

Dedicated to my mother
Chandrika Dinkar Barapatre

In loving memory of my father-in-law
Mr. Kalyan Kumar Bose

Table of Contents

Abstract

The methods of analysis with a focused ion beam, commonly termed as nuclear microscopy, include quantitative physical processes like PIXE and RBS. The element concentrations in a sample can be quantitatively mapped with a sub-micron spatial resolution and a sub-ppm sensitivity. Its fully quantitative and non-destructive nature makes it particularly suitable for analysing biological samples. The applications in biomedical research are manifold.

The iron overload hypothesis in Parkinson's disease is investigated by a differential analysis of human substantia nigra. The trace element content is quantified in neuromelanin, in microglia cells, and in extraneuronal environment. A comparison of six Parkinsonian cases with six control cases revealed no significant elevation in iron level bound to neuromelanin. In fact, a decrease in the Fe/S ratio of Parkinsonian neuromelanin was measured, suggesting a modification in its iron binding properties.

Drosophila melanogaster, or the fruit fly, is a widely used model organism in neurobiological experiments. The electrolyte elements are quantified in various organs associated with the olfactory signalling, namely the brain, the antenna and its sensilla hairs, the mouth parts, and the compound eye. The determination of spatially resolved element concentrations is useful in preparing the organ specific Ringer's solution, an artificial lymph that is used in disruptive neurobiological experiments.

The role of trace elements in the progression of atherosclerosis is examined in a pilot study. A differential quantification of the element content in an induced murine atherosclerotic lesion reveals elevated S and Ca levels in the artery wall adjacent to the lesion and an increase in iron in the lesion. The 3D quantitative distribution of elements is reconstructed by means of stacking the 2D quantitative maps of consecutive sections of an artery.

The feasibility of generating a quantitative elemental rodent brain atlas by Large Area Mapping is investigated by measuring at high beam currents. A whole coronal section of the rat brain was measured in segments in 14 h. Individual quantitative maps of the segments are pieced together to reconstruct a high-definition element distribution map of the whole section with a subcellular spatial resolution. The use of immunohistochemical staining enhanced with single elements helps in determining the cell specific element content. Its concurrent use with Large Area Mapping can give cellular element distribution maps.

Chapter 1

Introduction

In 1662 Robert Boyle published the second edition of his work from 1660 titled *New Experiments Physio-Mechanicall, Touching the Spring of the Air and its Effects* with an addendum describing the relationship between pressure and volume of a mass of gas at a given temperature, which is now known as Boyle's law. The vacuum pump employed for this work was designed by his assistant Robert Hooke [Wes05]. The subsequent independent work of these two natural philosophers would lead to furtherance, if not creation, of two initially unrelated disciplines of the natural sciences, namely analytical chemistry and microbiology. Laitinen recapitulates in *History of Trace Analysis* that Boyle was first to use the gall-nut powder quantitatively to determine the amount of iron in natural waters with the limit of detection at 160 parts per million (ppm) [Lai88]. He was also first to use the term "chemical analysis" for the litmus test that he had developed to distinguish between acids and bases [Bur82]. Meanwhile Hooke devised a compound microscope to study tiny organisms like fleas, insects etc. He also coined the term "cells" after observing the plant cells in a thin slice of cork. *Micrographia*, published in 1665, documents his detailed drawings of microscopic objects [Hoo65]. Hooke even corroborated the findings of van Leeuwenhoek, who had studied bacteria and blood cells, among others, with the aid of a simple microscope [Ges04]. Generations of scientists drew inspiration from their work to look beyond the resolving power of human eye.

However, the quality of the microscopes improved significantly only after Carl Zeiss with help of Otto Schott and Ernst Abbe started redesigning the optical components of the microscope based on Abbe's theoretical work on the optical principles. Abbe's formula puts the maximum resolving power of a microscope at half the wavelength of the probing light [Abb73]. Structures in nanometre-size range could only be imaged after the developement of the electron microscope and the scanning tunneling microscope in the 20th century. Similarly, a major push in the quantitative measurement of the amount of substances comes only after the discovery of the electron and the measurement of its mass to charge ratio by J. J. Thomson in 1897. This event is considered as the birth of mass spectrometry. The technique of separating masses based on their charges was used in earlier years to gain physical insights in the atomic and molecular structure and later for characterising biomolecules. The evolution of mass spectrometry from determination

of atomic weights of the elements to analysing proteomes was traced recently by Yates III [YI11]. It were the demands of modern day microbiology that spurred the intense collaboration between these two disciplines eventually leading to the formation of the field of spatially resolved microanalysis. Since the measured quantity is either element or molecule concentration, a quantitative map of the chemical composition with sub-micron lateral resolution can be created. Not only the mass spectrometers are able to perform this kind of quantitative imaging or microscopy but also the nuclear microprobes.

The tremendous curiosity and zeal in probing subatomic structure during the first half of the last century also led to the development of accelerator machines. These machines were required to generate a beam of energetic particles for studying the nuclear structure. As the research progressed larger and better machines were built for high-energy experiments aiming to study elementary particles comprehensively. In the process, the old small accelerators were rendered useless. They were but too precious to be discarded. So, the physicists explored outside the realm of pure nuclear physics for their applications. Not surprisingly, they could use these machines with little modification and with the help of then novel semiconductor detectors for quantitative *in situ* analysis. A brief history of the advent of nuclear microprobes can also be found in [JOH95]. The field of nuclear microscopy covers high-resolution measurements of structural, morphological and chemical composition of matter using nuclear microprobes (see chapter 2). The unique properties of nuclear microscopy attracted many applications in environmental sciences, materials analysis, electronics, and biological sciences. The success of nuclear microprobes can be judged by the fact that, nowadays, dedicated accelerator machines, microprobes and auxilliary equipments are being manufactured commercially. Applications of nuclear microprobes in biomedical research are discussed in a book by Llabador and Moretto [LLA96].

1.1   Quantitative microscopy

In biomedical research mostly those imaging techniques are routinely used that are capable of measuring *in vivo*. Modalities like Magnetic Resonance Imaging (MRI), Computed Tomography (CT), Positron Emission Tomography (PET) and Optical Imaging provide functional, anatomical, and molecular information. Traditionally, these techniques are used qualitatively. But, with the advent of digital image acquisition systems extraction of relative or absolute quantitative information with the help of experiment design and/or image processing tools is pursued vigourously. An insight review of imaging systems in molecular biology is given by Weissleder and Pittet [WEI08]. The chemical analysis techniques based on nuclear microprobe or mass spectrometry, on the other hand, provide quantitative data on element, isotope and molecule abundances with very high sensitivity. Few of these methods are described here briefly and compared to nuclear microscopy. The relevant figures of merit are summarised in table 1.1 and represented graphically in fig.1.1. For a detailed description and intercomparison of these methods refer to [LOB06, ORT09, BEC10].

Secondary Ion Mass Spectrometry (SIMS) is one of the most sensitive techniques for surface analysis. A focussed primary ion beam (mainly Cs^+ and O^-) sputters neutral and charged secondary atoms and molecules from the sample surface. The sputtered ions are then transfered to a mass spectrometer for measuring isotope and molecule concentrations with sensitivity in the ng/g range. Depending on the energy of the primary ion beam SIMS can be divided into static SIMS and dynamic SIMS. In static SIMS a low energy primary ion beam sputters just a few atomic layers from the surface, whereas in dynamic SIMS an intense energetic primary ion beam sputters faster and deeper. It is used to record concentration depth profiles. A new type of primary ion source enables a lateral resolution down to 50 nm. This method is destructive as the sample under analysis is progressively sputtered. Further, application of internal standards to the specimen is necessary for quantification.

Inductively Coupled Plasma Mass Spectrometry (ICP-MS) is a widely used solution-based technique for trace analysis with very high sensitivity. When coupled with laser ablation (LA-ICP-MS) it can provide spatial information as well. A tightly focussed laser spot thermally ablates the sample material from a thin tissue section placed on a glass substrate. The ablated material is then transfered by a carrier gas to the ICP-MS, where it is processed by the mass spectrometer. The spatial resolution of this technique ranges from 5 µm to 200 µm [Bec10]. Optimum thickness for biological sections is 20 µm to 30 µm. For quantification matrix-matched standards are required.

Electron Probe Microanalysis (EPMA) is one of the first X-ray microanalysis techniques. It is based on an electron microscope equipped with an energy dispersive X-ray detector. The electron beam excites a finite sample volume to produce characteristic X-rays. These X-rays are analysed spectrometrically to generate quantitative element distribution maps. Although this technique provides excellent spatial resolution in the nm range for thin sections, it suffers from poor sensitivity due to low signal to background ratio because of bremsstrahlung. In bulk analysis the scattering of electrons limits the spatial resolution to below one micrometre. The book by Goldstein et al. on scanning electron microscopy [Gol03] gives an in-depth description of this method.

Particle Induced X-ray Emission (PIXE) is a nuclear microscopy method for element analysis (sec.2.3). It is performed mostly with an energetic proton beam. Similar to EPMA, an energy dispersive detector records the characteristic X-rays emitted after excitation by the proton beam. But, it is far more sensitve than EPMA because of a higher signal to background ratio. The latest generation of microprobes can routinely achieve sub-micrometre spot sizes. Simultaneous measurement of the local mass by Rutherford Backscattering Spectrometry (RBS, sec.2.2) makes it a fully quantitative technique for trace analysis.

In Synchrotron X-ray Fluorescence (SXRF) the sample is irradiated with energetic and highly monochromatic photons. Again, the characteristic X-rays generated during de-excitation are measured to map element distribution quantitatively with high sensitivity. A 100 nm spatial resolution is now possible with latest synchrotron sources. Together with X-ray absorption spectroscopy it can provide the oxidation state of the element in addition.

Table 1.1: Figures of merit of various quantitative imaging methods [Lob06, Ort09, Bec10].

Quantitative imaging methods	Sensitivity ($\mu g\,g^{-1}$)	Spatial resolution (μm)	Depth resolution (μm)	Selectivity
LA-ICP-MS	0.001 - 1	5 - 200	20	Isotope
SIMS (dynamic)	0.1	0.05	0.1	Isotope
EPMA	100 - 1000	0.03 - 0.5	0.1	Element
Nuclear Microscopy	0.3 - 10	0.2 - 2	5	Element
SXRF	0.1 - 1	0.1 - 2	100	Element

1.2   Sensitivity and spatial resolution

Figure 1.1 shows the range of sensitivity and spatial resolution for different quantitative microscopy techniques. In general, higher spatial resolution is achieved at the cost of sensitivity and vice versa for the methods plotted here. The EPMA is the least sensitive technique despite offering a very high spatial resolution. On the other hand LA-ICP-MS offers best sensitivity as it uses ICP-MS for elemental analysis. The laser spot used for ablating the sample, however, can not be focussed more tightly without compromising its intensity, which limits the spatial resolution to $5\,\mu m$. Another mass spectrometry technique, dynamic SIMS, provides the best combination of lateral resolution and sensitivity. However, it is difficult to get fully quantitative information, as the modeling of formation of ions is not accurate and depends heavily on the matrix composition. Further, it is a destructive technique as well.

Among non-destructive techniques only nuclear microscopy is fully quantitative and standardless. SXRF has slightly better sensitivity and lateral resolution than PIXE, but it requires beam time at the synchrotron facilities, which can be expensive and scarce. The main advantage of SXRF is that it can be used in air and has the highest penetration depth of around $1\,mm$. It can, thus, be used for analysing whole cells *in vivo*. The figure quoted in the table 1.1 for the depth resolution of the nuclear microscopy is conservative. A depth profiling far better than $5\,\mu m$ is possible with RBS. The quoted figure is typical for quantitation of elements by PIXE in biological samples, where the local mass density is measured by RBS. The depth resolution here represents the optimum thickness of biological tissue for measurement by nuclear microscopy [Lla96]. In [Lob06] the sensitivity for nuclear microscopy is quoted $1\,\mu g\,g^{-1}$. A sensitivity of $0.3\,\mu g\,g^{-1}$ can be achieved routinely at LIPSION because of its high beam brightness. In case of an appropriate biological matrix a sensitivity of even $0.1\,\mu g\,g^{-1}$ is possible.
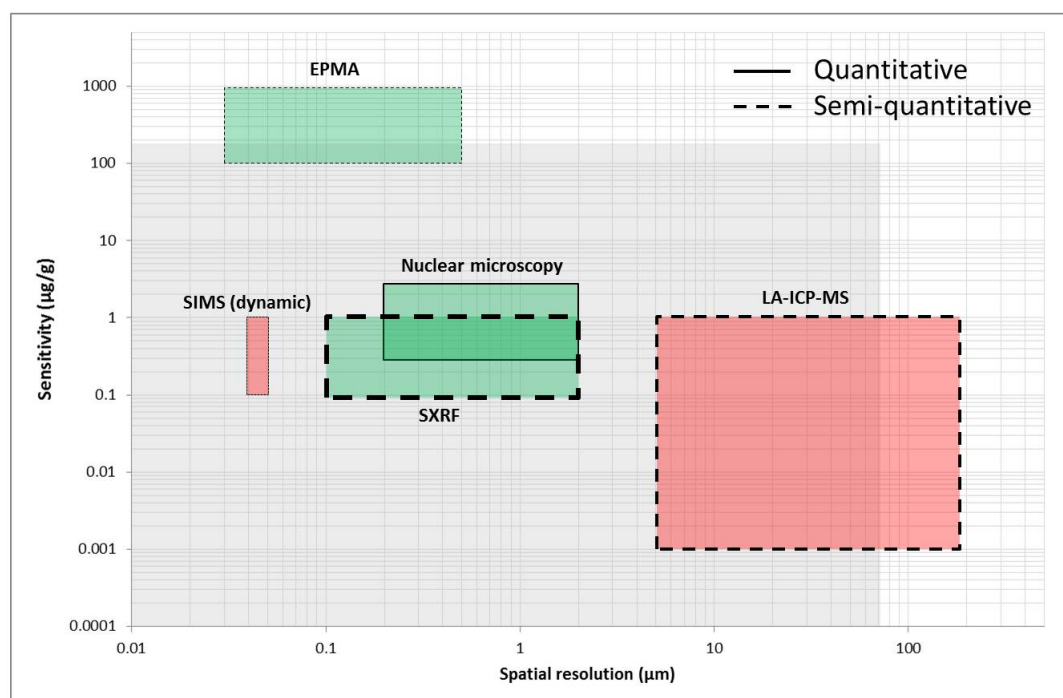
Figure 1.1: Graphical representation of the figures of merit of different quantitative imaging methods. The gray shaded area represents the amount of iron ($\approx 200\,\mu g\,g^{-1}$) in the *substantia nigra* (SN) of healthy adults aged between 40 and 90 years [ZEC02] and the size of a typical dopaminergic neuron in SN ($\approx 70\,\mu m$). The range of sensitivity and spatial resolution of individual methods are depicted with rectangles whose boundary thickness is an indicator of the relative depth resolution. The thinner the boundary, the better the depth resolution. The quantitative nature of the method is represented by a solid line and the dashed line stands for a semi-quantitative nature. The colour red is for a destructive technique and the colour green for non-destructive.

1.3 Trace elements in human body

It is believed that six elements are required for life to exist; hydrogen, carbon, nitrogen, oxygen, phosphorus and sulphur. These elements make up the basic units of life like nucleic acids, proteins, and lipids. Wolfe-Simon et al. were recently able to subsititute arsenic for phosphorus in a naturally occuring bacterium as As is biochemically similar to P [WS11]. This kind of substitution may work in a unicellular living organism like a bacterium. However, as the complexity of an organism increases more elements are required to support life. The Periodic Table of naturally occuring elements can be divided into three groups based on their quantities present in the human body. H, C, N, and O are called major or basic elements and constitute about 99% of all the elements present in the body. Na, Mg, P, S, Cl, K, and Ca are called minor elements, and all other elements are called trace elements [MER81]. Around 26 elements, including major and minor elements, are known to have physiological functions in humans and, hence, are considered

essential elements [MER81, IYE89]. The essential trace elements like Fe, Cu and Zn are indispensible for optimal functioning of biological processes. The concentration of these elements is in the parts per million (ppm) range. Even though the trace elements are present in minute quantities, any subtle difference in their concentration leads to impaired functioning of the physiological processes. A lower concentration, e.g. impedes growth and a higher concentration can be toxic. For proper growth and stable health it is important to maintain the required levels of these elements. In Europe the European Food Safety Authority (EFSA) monitors the research on the significance of trace elements in human health and provides Dietary Reference Values (DRV) for all macro- and micronutrients [Foo06].

The functions of essential trace elments are wide and many. The books edited by Mertz [MER87] give an exhaustive description of the roles of trace elements in biological system. A short review of metals, their toxicity and oxidative stress is presented by Valko et al. [VAL05]. Based on this literature the roles of trace metals Fe, Cu and Zn are outlined here briefly.

Iron is the most abundant trace element in the human body with concentration of around $4\,g$ to $5\,g$ in an average adult. Due to the presence of unpaired electrons in its atomic shell it can readily participate in single-electron-transfer reactions. This property of iron is exploited in many biological processes. It is a structural part of haemoglobin, which transports oxygen and carbon dioxide between lungs and tissues. As part of cytochromes it transports energy within cells and as part of myoglobin it stores oxygen in muscles. It is a cofactor of enzymes involved in synthesis of the neurotransmitters dopamine and serotonin and it is involved in myelination of neurons. Evidently, iron is essential in growth and survival of living organisms. Its deficiency leads to, among others, anemia and cognitive deficits. Free iron is a source of oxidative stress. So, the level of free iron is kept as low as possible in the body. Dietary iron is absorbed from the gastrointestinal tract and sequestered into the iron transport protein transferrin. The transferrin shuttles iron via circulation to the destination cells, where it is hoarded by the storage protein ferritin and made available when required by the cellular processes. An elaborate network of sensing and signalling molecules regulates the overall iron content in the body.

Copper plays an active role in iron metabolism, connective tissue formation, respiration, free radical scavanging etc. Similar to iron, it can participate in single-electron-transfer reactions. It is, thus, part of enzymes that catalyze the movement of electrons within cellular compartments, for example, by cytochrome c oxidase in mitochondria. An adult human body has $15\,mg$ to $20\,mg$ of copper. The dietary copper is taken up in the gastrointestinal tract and is bound to serum albumin for transportation via circulation. In the destination cells it binds to copper chaperons, which transfer it to the target biomolecules. Such chaperons not only regulate the uptake and bioavailability of metal ions, but they also activate the recipient biomolecule. The Cu, Zn-dependent superoxide dismutase (SOD), for example, is activated while it receives copper from cytosolic copper chaperons (CCS). Copper is an essential part of the enzyme ceruloplasmin, which assists in binding iron to transferrin by changing its chemical state from a ferrous to ferric ion. A genetic disorder that disrupts the copper pathways leads to Menkes disease and Wilson's

disease.

Among all trace metals **zinc** plays the most extensive role in biology. After iron, it is the most abundant transition metal in brain. It has structural and catalytical functions in at least 3000 zinc proteins. Around $2\,g$ of zinc is found in an average human body, of which 90% is found in skeletal muscles and bones. Among the major functions of zinc are cell membrane integrity, maintenance of the immune system and wound healing. It structurally stabilises the CuZnSOD while copper dismutates the superoxide ion. It is an indispensible part of the antioxidant mechanism. The oxidative stress experienced by cells is directly linked to the levels of zinc. Its deficiency is implicated in lipid oxidation, which is one of the early steps in atherogenesis. Zinc is also actively involved in signal transduction. It interferes in many ways in calcium regulation.

Oxidative stress and antioxidants
The book by Halliwell and Gutteridge [HAL07] provides comprehensive knowledge on free radicals, oxidative stress and antioxidant mechanisms. A very short description of these phenomena is presented here.

Atoms, molecules, and ions with unpaired electrons are considered free radicals as they are highly reactive. The ability of iron and copper to participate in single-electron-transfer reactions makes them also a source of radical generation. Iron and copper in free state readily decompose hydrogen peroxide to generate reactive oxygen species (ROS) via the Fenton reaction (eq.1.1). The ROS can then damage biomolecules like proteins, lipids and DNA. Although the rate of reaction for copper is higher than for iron, the sheer abundance of iron makes it a major source of oxidative stress.

$$\mathrm{Fe^{+2}(Cu^+) + H_2O_2 \rightarrow Fe^{+3}(Cu^{+2}) + OH^{\cdot} + OH^-} \tag{1.1}$$
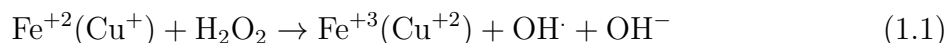
Zinc does not participate in redox reactions, rather protects biomolecules from oxidative damage due to iron and copper ions. By binding to proteins it changes their conformation and renders them incapable of participating in redox reactions. Therefore, it is a constituent of antioxidant enzymes like superoxide dismutase and the non-enzymatic protein metallothioneins that scavenge free radicals.

The functions of trace elements are so extensive, complex, and interdependent that any imbalance in one of them will necessarily lead to disrupted physiological processes. Non-physiological levels or a non-specific accumulation of trace elements is reflected in various diseases. A highly sensitive method is therefore required to discern the subtle differences in the concentrations of elements that themselves are present only in trace amounts. The methods of nuclear microscopy have the right sensitivity to measure such differences. Further, the characteristics like the fully quantitative nature, no requirement of internal standards, non-destructive, ease in sample handling, and measurement etc. make nuclear microscopy the method of choice.
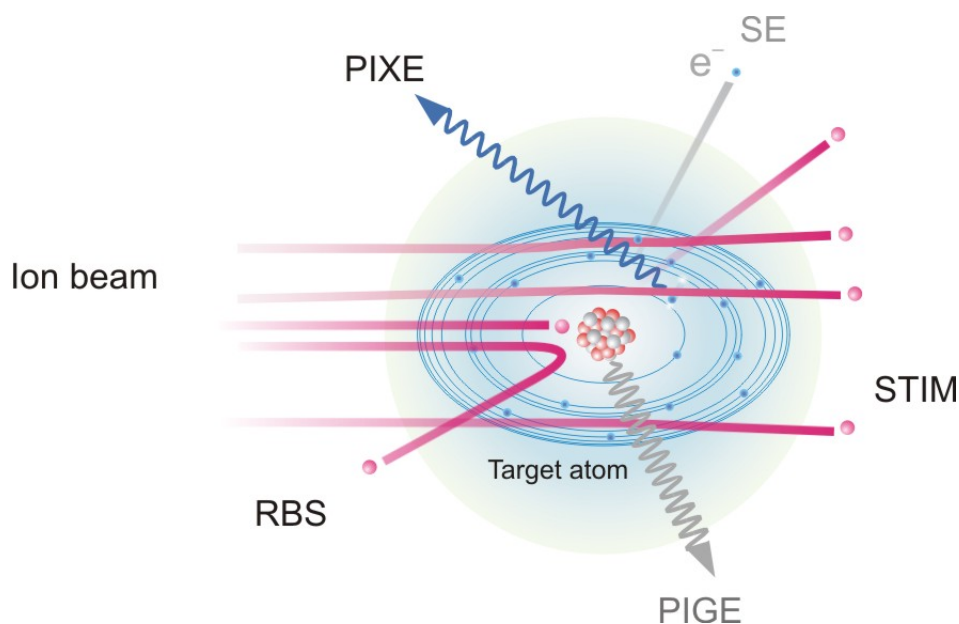
Chapter 2

Nuclear Microscopy

Figure 2.1: A schematic representation of various methods of nuclear microscopy based on the interaction of energetic ion beam with target material (adopted from [REI01A]).

All matter is made up of atoms of one or more elements. An atom has a nucleus, made up of protons and neutrons, and a cloud of electrons orbiting around the nucleus. These electrons occupy discrete energy levels, also called electron shells, around the nucleus dictated by quantum physical rules. The farther the electron from the nucleus, the higher the energy of the level occupied by it. Conventionally, the shells are named $K, L, M, ...$, where K represents the innermost shell. Each shell is defined by three quantum numbers, namely principal number $n \geq 1$, orbital angular momentum $l = (0, ..., n-1)$, and the magnetic quantum number $m = (-l, ..., +l)$. The coupling between the spin of the electron $(s = -\frac{1}{2}, \frac{1}{2})$ and the orbital angular momentum l to the total angular momentum $j =$

$(l + s, l + s - 1, ..., |l - s|)$ leads to the splitting of the energy level into $2l + 1$ degenerate states. Except for the K-shell, each shell consists of subshells. Each element possesses a unique electronic configuration. When incident upon matter, a beam of energetic charged ions interacts in many ways with the target electrons and nuclei. This interaction leads to atomic inelastic processes like excitation and ionisation, and nuclear elastic and inelastic collisions. The probability of any such kind of interaction taking place is expressed in terms of a cross-section with units in barn ($1\,\mathrm{b} = 10^{-28}\,\mathrm{m}^2$). It represents an effective area available for an incident particle to produce an interaction with 100% probability. Obviously, the larger the cross-section, the more events are produced for any particular interaction. The nuclear and atomic processes relevant to this study are explained briefly in the following sections.

2.1 STIM – Scanning Transmission Ion Microscopy

Mapping of mass density distribution of a thin target by measuring the energy loss incurred by the ion beam after passing through a target material is defined as STIM.

Theory

While traversing matter the incident ions lose energy due to collisions with the target electrons and nuclei. Attempts to describe the electronic energy loss quantitatively were first made in 1913 by Bohr [Boh13] using classical mechanics and later by Bethe using quantum mechanics for both non-relativistic [Bet30] and relativistic cases [Bet32]. Felix Bloch generalised this description in 1933 [Blo33]. The Bethe-Bloch formula for an ion with charge number z and velocity v incident upon a target of charge number Z is given by eq. 2.1, where N is the number density and I the mean excitation potential of target atoms, m_e is the rest mass of electron, e the elementary charge and $\beta = \frac{v}{c}$ being the relativistic factor.

$$-\frac{\mathrm{d}E}{\mathrm{d}x} = \frac{4\pi}{m_e v^2} N Z z^2 \left(\frac{e^2}{4\pi\epsilon_0}\right)^2 \left[\ln\frac{2m_e v^2}{I} - \ln(1 - \beta^2) - \beta^2\right] \tag{2.1}$$

The property of the target material to decelerate the incoming ions is called Stopping Power and is defined as specific energy loss per unit length incurred by an incoming ion inside the target material of density ρ. It is given by equation 2.2.

$$S(E) = -\frac{1}{\rho}\frac{dE}{dx} \tag{2.2}$$

Conversely, the range of ions in a specimen is defined as the distance traveled before losing all initial kinetic energy in the target. Since the energy loss process underwent by a single ion is statistical in nature, only the mean range of all the ions can be stated. It is given by equation 2.3.

$$\bar{R} = \frac{1}{N} \int_0^{E_0} \frac{\mathrm{d}E}{S(E)} \tag{2.3}$$

The stopping power is a characteristic of the composition of the material. Hence, the stopping power of a compound is to a very good approximation the sum of stopping powers of the individual elements S_Z in the compound weighted by their relative mass content in the sample c_Z (Bragg's Rule),

$$S(E) = \sum_Z c_Z S_Z(E) \tag{2.4}$$

A closer look at equation 2.2 reveals that the stopping power is not only a function of energy but also of the areal mass density μ of the target with $d\mu = \rho \cdot dz$. The areal mass density of a specimen can be calculated by measuring the loss of energy of ions after their passage through the specimen.

Since the Bethe-Bloch formula is based on an idealised model that assumes full ionisation of the ion inside the target and takes only electronic energy loss into account, its use with Bragg's rule, which itself is of limited accuracy, results in non-precise values of specific energy loss in the low-energy region. The semi-empirical approach of Ziegler [Zie85] provides more accurate results, as it includes experimental values for stopping powers from numerous ion-target pair experiments. The Monte Carlo simulation program (SRIM) based on this data-set gives stopping powers for compounds within 5% accuracy [Zie].

Signal Detection and Data Processing

The STIM detector measures the residual energy of the protons. Due to the stochastic nature of the energy loss in the sample, more than one proton has to be measured per pixel to get a statistically relevant output. In general, a median of five protons per pixel provides a reliable measure of the energy loss in the sample. STIM measurements are typically performed at low beam currents in order to avoid high dead time during the measurement. The energy spectrum needs no further processing as the mass density distribution can be calculated from the energy loss map by solving equation 2.5.

$$\mu = \int_{E_0}^{E_t} \frac{\mathrm{d}E}{S(E)} \tag{2.5}$$

A simple software developed for this work reads the event file of the measurement and produces spatially resolved two-dimensional maps of energy loss in the sample. If the incident energy of the protons is kept the same, the areal mass density of different samples can be compared relative to one another. However, an energy per channel calibration is needed for the determination of the absolute energy loss in the sample. This can be performed by measuring multiple layers of partially overlapping Mylar foils of known areal density. A SRIM calculation gives the residual energy for individual thicknesses of this layered structure. A linear fit then provides the energy value for the corresponding channel number.

2.2 RBS – Rutherford Backscattering Spectrometry

In BS the structural and the compositional information of a sample is derived by measuring the energy of incident ions that are scattered backwards from the sample's nuclei at a given angle. Figure 2.2 depicts schematically the process of backscattering.
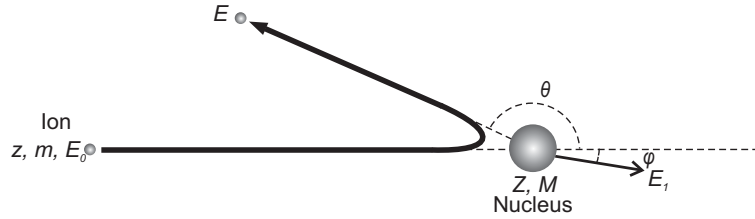

Figure 2.2:   An illustration of the backscattering phenomenon. A light projectile is deflected backwards from a massive nucleus. In an elastic collision for a given incident energy the energy of the backscattered projectile is dependent only on the mass of the scatterer and the angle.

Theory

In 1909 Geiger and Marsden noticed the unexpected deflection of alpha particles from a gold foil to angles greater than 90°. Since this observation could not be explained with the then prevalent plum pudding model of the atom, Rutherford put forward his model of the atom in 1911, in which all the positive charge is concentrated in the center of the atom. When a positively charged ion penetrates matter it is scattered by the Coulomb potential of the nuclei of target atoms. The scattering angle can be as large as 180°. If the scattering is elastic and the angle of deflection θ is $90° < \theta \leq 180°$ it is called Rutherford Backscattering. A comprehensive description of the method can be found in [CHU78].

For a projectile ion of mass m the kinematic factor K, which is the ratio of projectile's final energy E to its initial energy E_0, is given by eq. 2.6. Here, M is the mass of the target atom.

$$K = \frac{E}{E_0} = \left[\frac{\cos\theta + \sqrt{\left(\frac{M}{m}\right)^2 - \sin^2\theta}}{\frac{M}{m} + 1} \right]^2 \tag{2.6}$$

For a given m and θ the K-Factor depends only on the mass M of the target atom. The higher the ratio M/m, the higher the backscattered energy E. In general, hydrogen or helium ions are used as projectiles.

The differential cross-section $d\sigma/d\Omega$ is a measure of the probability with which an incoming ion of energy E will be scattered by the angle θ in the solid angle $d\Omega$. For

elastic scattering it is given by equation 2.7.

$$\frac{d\sigma}{d\Omega} = \left(\frac{zZe^2}{16\pi\epsilon_0 E_0}\right)^2 \frac{4}{\sin^4\theta} \frac{\left(\sqrt{1 - [(m/M)\sin\theta]^2} + \cos\theta\right)^2}{\sqrt{1 - [(m/M)\sin\theta]^2}} \tag{2.7}$$

In case the ion has sufficient energy to overcome the Coulomb barrier of the nucleus the nuclear forces also influence the scattering of the ion. The result is a substantial deviation from the above equation. For light elements the deviation can already be seen with MeV protons as projectiles. These cross-sections are determined empirically, and are called non-Rutherford cross-sections (fig.2.4).
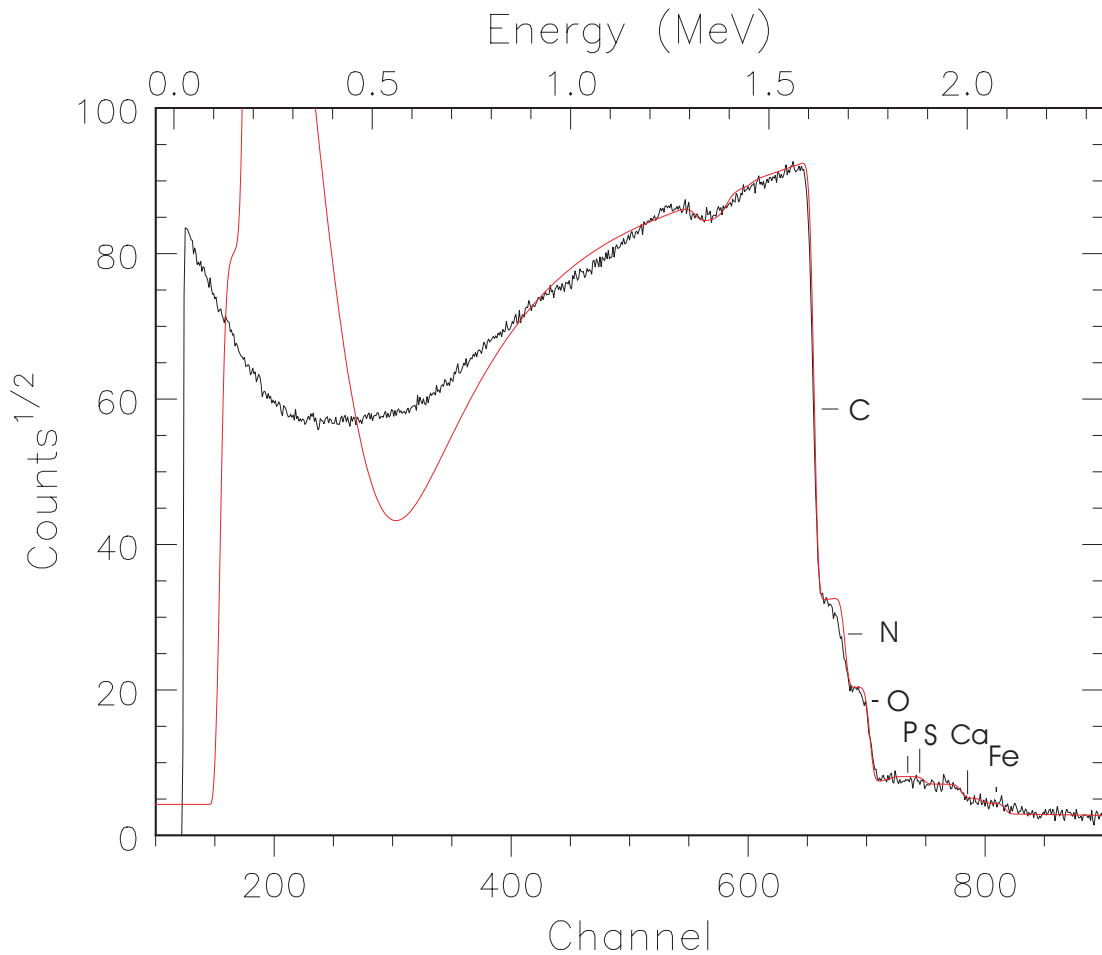
Figure 2.3: A representative BS spectrum of a biological tissue embedded in a polymer resin. In black is the measured signal and in red is a simulation by RUMP. The edges of matrix elements (C, N, O) are distinctly visible. Note: Below 1 MeV ions come from greater depth of the sample, where the simulation is increasingly less accurate due to multiple scatter events.

Signal Detection and Data Processing

The signal from the detector undergoes a two-stage amplification and is subsequently digitized and recorded by the data acquisition system (DAQ). Figure 2.3 shows a representative BS spectrum of a biological tissue. Edges of the matrix elements (C, N, O) are clearly discernible in the graph. To determine the stoichiometry of the sample quantitatively the algorithm of Doolittle is used [Doo85]. The program RUMP based on this algorithm simulates a backscattering spectrum for a given set of constant and variable input parameters. The constant parameters include type, charge and energy of the ion, the scattering angle θ, and the solid angle and the resolution of the detector. The number of incident ions N_p (total charge), the thickness, and the composition of the sample (areal mass density) are varied until there is a good match between the simulated and the measured spectrum. It is important to use non-Rutherford cross-sections for the light elements. These can be obtained from a web-program called SigmaCalc developed by Gurbich and hosted on the website of the International Atomic Energy Agency (IAEA) [Gur]. It uses a validated theoretical model for computing the cross-sections. The theoretical model was developed based on the already published empirical cross-sections and is validated by posterior measurements and benchmark tests. Figure 2.4 shows the non-Rutherford cross-section for protons incident on a carbon target as calculated by this model.

The simulation fails in the lower energy regions due to indeterminate factors like multiple scattering, etc. The total charge $Q = N_p \cdot e$ and the areal mass density of the sample simulated by RUMP is used in the analysis by PIXE.
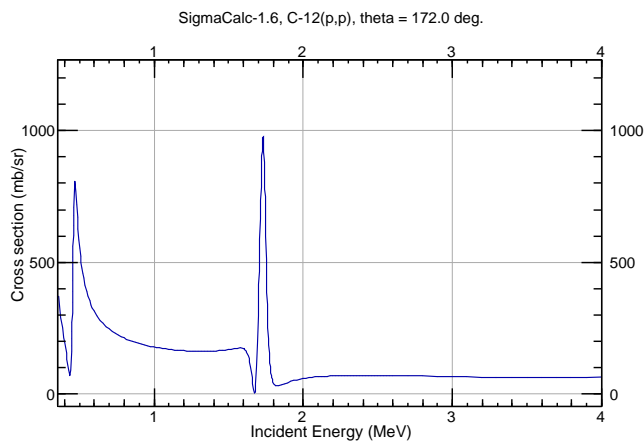

Figure 2.4: Non-Rutherford cross-section for MeV protons on carbon target.

2.3 PIXE – Particle Induced X-ray Emission

PIXE is a method for quantitative determination of the elemental composition of a specimen with $\mu g\,g^{-1}$ sensitivity.

Theory

Henry Moseley was first to discover in 1913 that the energy of X-rays produced by various elements were related to the nuclear charge Z of that specific element. When an incident ion knocks out one of the inner shell electrons of a target atom, the vacancy created is filled immediately by an electron from an outer shell. Since this transition takes place from a higher energy level to the lower energy level, the excess energy can either be released by emitting an X-ray photon or, in a non-radiative way, by transferring the energy to a peripheral electron and, thereby, ejecting it from the atom. The former process is called Particle Induced X-ray Emission (PIXE) and the latter Auger Emission. The emitted photon in PIXE has an energy that is characteristic of the fluorescing atom, since each element has a unique arrangement of electronic energy levels. By measuring the energy of the emitted photon the fluorescing atom can readily be identified. The intensity of the photons indicates the concentration of the element. The book by [Joh95] gives a comprehensive description of this method.
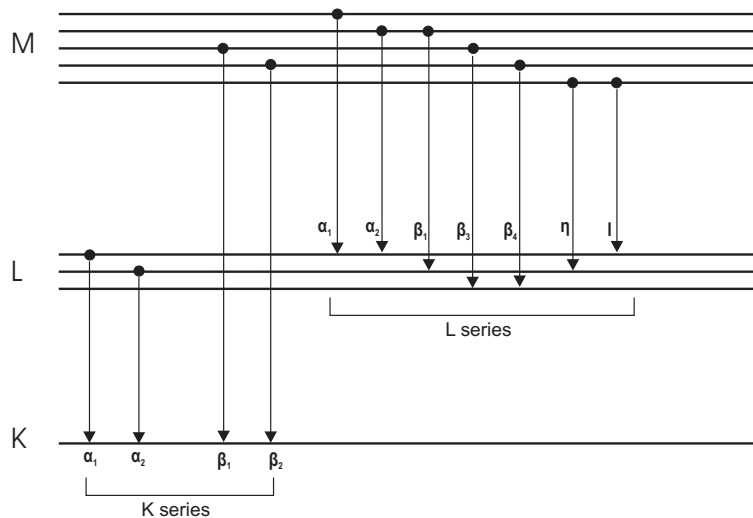

Figure 2.5: Energy levels of an atom and X-ray line series generated after electronic transitions to vacancies in K and L shells.

PIXE can be considered as a two-step physical process; primary inner shell ionisation and the subsequent fluorescence with yield ω due to electron transitions. The transition of an electron can only take place if $\Delta n \geq 1, \Delta l = \pm 1$ and $\Delta j = 0, \pm 1$. Figure 2.5 shows the possible electron transitions that can occur as a result of vacancies in K and L

shells. For any given shell the number of vacancies created will directly be proportional to the number of incident protons N_p, and the shell ionisation cross-section σ for the given proton energy E. In a target of considerable thickness the incident protons will lose part of their initial energy as they traverse the target specimen as described by the Bethe-Bloch formula (eq.2.1). The trajectory of the protons can be considered, to a fair approximation, a straight line, since most of the interactions are with the light electrons. However, the probability of ionisation and fluorescence will vary with the penetration of protons in the sample, as σ is dependent on the proton energy. Similarly, the X-rays generated inside the specimen undergo attenuation on their way to the detector due to interactions with the major elements constituting the specimen. This phenomenon is called the Matrix Effect. A transmission factor is defined to take into account this matrix effect. It is given by eq. 2.8, where (μ/ρ) is the mass attenuation coefficient of the sample, α the incidence angle of protons to the normal of the sample surface and β the X-ray detection angle to the normal of the sample surface (fig.2.6).

$$T_Z(E) = exp\left\{-\left(\frac{\mu}{\rho}\right)_Z \frac{\cos\alpha}{\sin\beta} \int_{E_0}^{E} \frac{dE'}{S(E')}\right\} \tag{2.8}$$
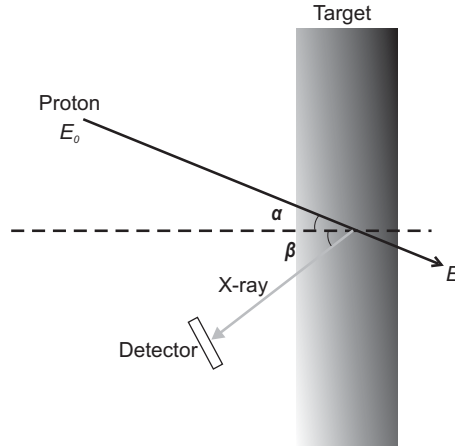

Figure 2.6: The geometrical parameters in the transmission factor are illustrated in this diagram.

If the specimen is so thin that the proton energy loss and the X-ray attenuation can be neglected ($\Delta E <10\%$) the transmission term reduces to unity. During the experiments the angles were always $\alpha = 0°$ and $\beta = 45°$.

Considering the case of K-shell excitation the total X-ray yield is given by eq. 2.9. Here, c_Z is the concentration of the constituent element of charge number Z and atomic mass A, and b_X is the line intensity fraction. ϵ characterises the detection efficiency.

$$Y_X(Z) = \frac{N_A \omega_Z b_X \epsilon N_p c_Z}{A_Z} \int_{E_0}^{E} \frac{\sigma_Z(E)T_Z(E)}{S(E)} dE \tag{2.9}$$

The values for fluorescence yields ω_Z and the relative line intensities b_X are published in [KRA79]. The empirical ionisation cross-sections $\sigma_Z(E)$ [PAU89] correlate very well with the values calculated theoretically [CHE85, CHE89]. For K-shell the uncertainty is less than 3% [CAM90].

Signal Detection and Data Processing

In order to keep the energy spectrum clean from contributions due to backscattered ions a 60 μm thick polyethylene foil is placed in front of the detector window. It facilitates the absorption of backscattered ions in the 25 μm thick Be window of the detector. Whereas this arrangement protects the expensive detector crystal from damage, which is a primary concern, it has a negative effect on the detection efficiency ϵ for the low-energetic photons, i.e. ϵ is strongly reduced for photons with energy $E_X < 2$ keV. Hence, the detection of elements with $Z < 12$ is not possible with this setup

A representative PIXE spectrum of a biological tissue is shown in fig.2.7. The characteristic peaks lie above the background signal due to bremsstrahlung from secondary electrons. For trace elements like Fe, Cu, and Zn the background is almost negligible. Hence, these elements can be measured with high sensitivity.
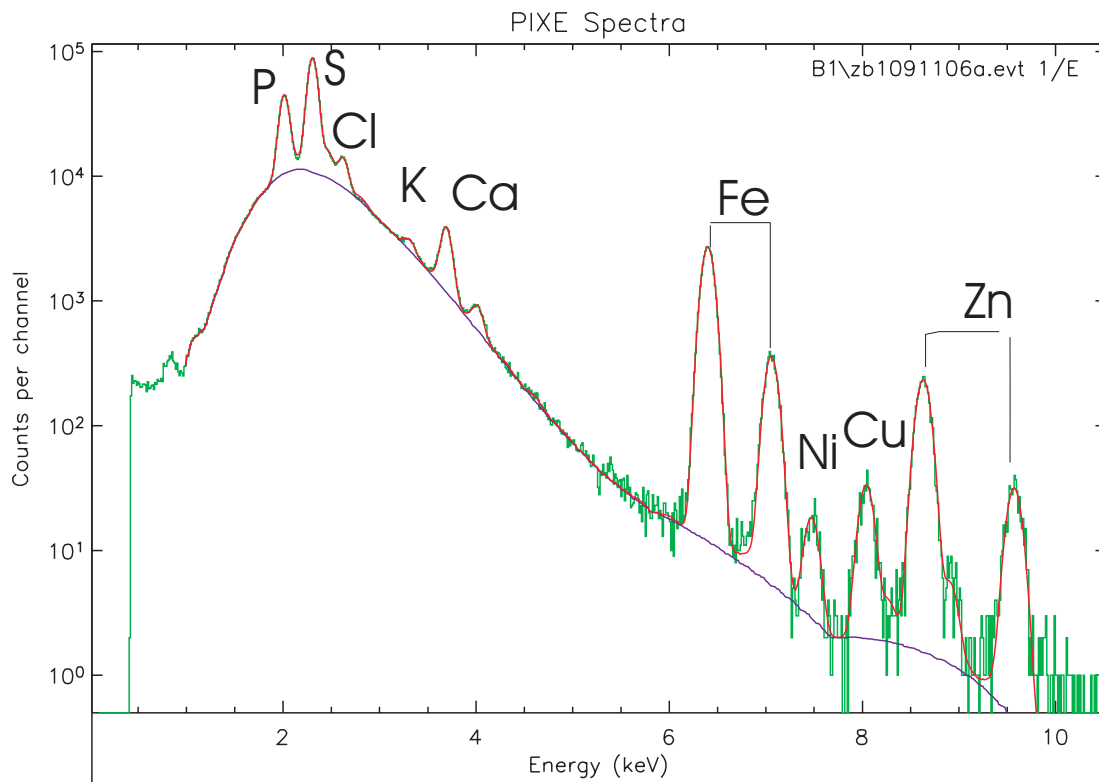

Figure 2.7: A representative PIXE spectrum of a biological tissue. In green is the measured signal, in red an analytical fit, and in blue the background. The signal to background ratio is particularly high in the region of trace elements Fe, Ni, Cu and Zn.

On rearranging equation 2.9 for c_Z we get,

$$c_Z = \frac{Y_X(Z)}{Q} \cdot \frac{A_Z \cdot e}{N_A \omega_Z b_X \epsilon} \cdot \frac{1}{\int_{E_0}^{E_t} \frac{\sigma_Z(E)T_Z(E)}{S(E)} dE} \tag{2.10}$$

where $Q = N_p \cdot e$ is the total integrated charge incident upon the sample. This equation lends itself to a standard-free quantitation of elements. There are powerful computer programs available to perform the calculation for a measured spectrum. The input parameters required for solving the equation are the total charge Q, the detection efficiency ϵ, the energy E_t of transmitted protons and the stopping $S(E)$. The initial energy of protons E_0 is defined by the accelerator settings. The total charge Q can either be measured electrically in a Faraday cup or can be determined from the BS spectrum. The latter also provides quantitative information on the matrix elements. Together with the sample thickness, which is known from the preparation procedures, this information is used to calculate E_t.

The quantitative imaging and analysis software GeoPIXE II developed by Ryan [Ryan01] was used to process the PIXE data. This software is based on a method called Dynamic Analysis [Ryan95]. The various components of the PIXE spectrum such as element line shape, continuum background, pulse pile-up, escape peaks, etc. are described by a non-linear least-squares fit to the spectrum using a model function. The main advantage of this method lies in resolving strongly overlapping energy peaks [Ryan00]. The fit-routine thus calculates the concentration of element from the yield Y_X without the artefacts from the detection system and inhomogeneous background. The tabulated output contains, besides c_Z, the fitting error and the element-specific minimum detection limit (MDL). The MDL is the level of concentration above which the element can be detected with a confidence level of 99%. The limit of quantification (LOQ) is at three times the MDL. The calculated concentration values are projected in the element maps by sorting the PIXE events according to their spatial coordinates. The element maps so generated are quantitative and give a true spatial distribution of the elemental concentration.

Chapter 3

Technical Aspects of Nuclear Microscopy

Die Wende is a german word for 'change' or 'turning point' and now also refers to the events in the years 1989 and 1990 that led to the fall of the socialist regime in eastern Germany and eventually to the formation of a single German state. After reunification a lot of money flowed in the 'newly formed states' for the development of the infrastructure. The renewal of the universities was also a part of this drive. This provided an opportunity to scrap the old Van de Graaff accelerator machine operational since 1963 at the University of Leipzig and build an entirely new state-of-the-art ion beam laboratory right from scratch. Aware of the potential of an ion microprobe as a unique and powerful analytical tool, it was decided to build a system for analysis and modification with spatial resolutions at a sub-micron scale [BUT97]. The laboratory went into operation in 1998 and is named LIPSION in accordance with *Lipsk*, the Slavic origin of the name Leipzig, meaning 'settlement about the lime trees'. The first results were published in early 2000 [BUT00].

The ion beam laboratory mainly consists of an electrostatic linear accelerator and two beam lines for experiments. The 45° beam line is used for experiments with an unfocused, collimated ion beam, whereas the high-resolution work is done at the 90° beam line, also called the nanoprobe. Since this work is solely based on the experiments done at the nanoprobe, only the features of the accelerator and the nanoprobe are outlined here. Figure 3.1 shows a schematic drawing of LIPSION.

3.1 The Accelerator

For the microanalysis with a sub-micron spatial resolution on routine basis, drastic improvements in the energy stability and the beam brightness were needed. So, a novel accelerator machine was designed especially to meet the demands of a nanoprobe. Since the building, where the laboratory was to be housed, was being restructured at the same time, the construction work could be influenced to provide an optimal environment for the new facility. The accelerator and the nanoprobe stand on separate massive found-
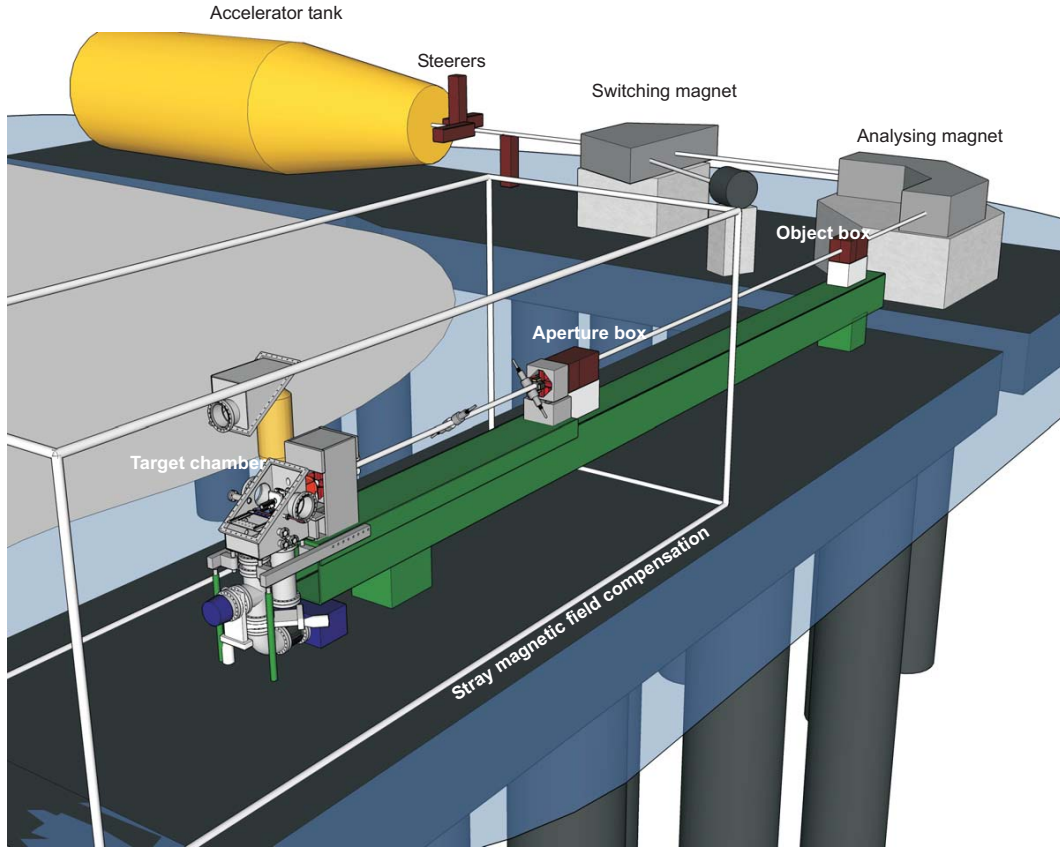
Figure 3.1: A schematic diagram of LIPSION.

ations rooted on a vibration-dampening layer of underground, decoupled from the rest of the building. The facility room is equipped with a powerful air conditioning system, which keeps the room temperature constant at (23 ± 0.5)°C with a relative humidity of 45% to avoid thermal drifts of the system and prevent water vapour from condensating on the water-cooled parts. The stray magnetic fields from the trams passing by near the laboratory had a degrading effect on the lateral resolution. A system which actively compensates these fields by sensing them and producing a weak magnetic field to counter it, was installed later [Spe03].

The accelerator is a 3.5 MV Singletron$^{\text{TM}}$machine built by High Voltage Engineering Europa. It has an energy stability of $\approx 10^{-5}$ and a beam brightness of $30\,\text{A}/(\text{rad}^2\,\text{m}^2\,\text{eV})$ [Mou97]. It is a linear accelerator of the Van de Graff type. The positive ions of charge q are accelerated in the uniform electric field of voltage U to a kinetic energy given by $E_{\text{kin}} = q \cdot U$. The traditional Van de Graff machines use a rotating belt made either of rubber or metal cylinders as charge transporters for the generation of high voltages. The vibrations and inhomogeneities from the rotating components severely limit the energy stability of the accelerator. In contrast, the Singletron has no moving parts, except for power generator for the ion source, and the high voltage is generated with a diode cascade using Cockcroft and Walton method [Coc32].

The accelerator tank is divided into two parts; the rear part generates the high voltge and the front part accelerates the positive ions H^+, H_2^+ and He^+. The ion source sits closer to the center of the accelerator tank. As per requirement hydrogen or helium gas is let in a glass tube and ionised to a plasma by a high-frequency electromagnetic field. The application of a probe voltage injects the positive ions from this plasma into the extraction channel of the acceleration tube, where the extraction voltage together with the electrodes allows to focus the particles onto the object plane of the downstream 90° analysing magnet. Two pairs of electrostatic steerers provide finer adjustments of the beam trajectory in horizontal and vertical direction, so that the loss in transportation is minimised. A switching magnet in front of the 90° analysing magnet can bend the ion beam into the 45° beamline. The ion beam is transferred under high vacuum conditions (10^{-7} mbar) to the desired target chamber.

3.2   The Nanoprobe

The nanoprobe is preceded by a 90° analysing magnet, which acts as an energy discriminator. The positive ions moving perpendicular to the direction of the homogeneous magnetic field B inside the magnet experience the Lorentz force $F = q \cdot v \cdot B$ and are subjected to circular motion. The magnetic field strength is chosen such that only ions with desired energy are directed into the nanoprobe and projected onto its object diaphragms. The task of a nanoprobe is to provide a demagnified image of the object diaphragm at the specimen position. The nanoprobe installed at LIPSION enables scanning of the specimen in the sample chamber with a highly focused ion beam. It was constructed by MARC Melbourne and consists of object and aperture diaphragms, four magnetic quadrupole lenses for demagnification and a beam deflection unit for scanning.

A single steel girder supports the nanoprobe in a most rigid manner. The object diaphragms define the initial beam size and the aperture diaphragms give the divergence of the ion beam. Both are separated by a distance of 4.9 m. The object diaphragms are available in diameters of 5 µm, 10 µm, 20 µm, 50 µm, 100 µm, 150 µm, 200 µm and 300 µm. The aperture box has an additional 30 µm diaphragm at the expense of 150 µm. Both sets of diaphragms are mounted on copper blocks in two columns of four rows. The movement of the object diaphrags is controlled by conventional micrometre screws in horizontal as well as vertical direction. The aperture diaphragms are displaced using digital micrometre screws in both directions.

The quadrupole lenses are positioned downstream of the aperture diaphragms. The magnetic field of a single quadrupole will focus the ion beam in one plane and defocus it in the perpendicular one. Only a consecutive arrangement of two quadrupole pairs will have a combined effect of symmetric demagnification. There are two doublets of quadrupole lenses separated by a distance of 2.49 m which are configured as a separated Russian quadruplet system. Consequently, the demagnification is large and orthomorphic. The experimental demagnification factor $D_{x,y} = 130$ is much better than the theoretically expected value of $D_{x,y} = 104$ after the realignment of the magnetic lenses [ROT09]. Hence,

a sub-micron spot size is achieved with an object diaphragm of $100\,\mu m$. The Russian quadruplet system provides a large working distance of $d = 330\,mm$. It is the distance between the last lens and the focal point of the ion beam.

The space created between the lens and the sample chamber allows to accommodate the scanning unit. The ion beam is deflected by an induced magnetic field due to the flow of current in the copper coils of the scanning unit. A coputer-controlled transconductance amplifier of type Murray Amplifiers MA 534 drives the flow of current in the scanning unit. The scan size is proportional to the winding number $N_{x,y} = 1, 2, 4, ..., 256$ of the coil and can be as small as $3.2\,mm \times 3.2\,mm$ and as large as $3.2\,mm \times 3.2\,mm$.

3.3   The Sample Chamber

The sample chamber houses the devices for sample positioning and observation, event detectors, and charge measurement. To address the growing needs of more precise and novel experiments, the old sample chamber was replaced in 2006 with a larger multi-purpose chamber [Nil07]. It has the form of a rectangular box with removable hood and has a volume of 64.8 litre. An exit nozzle can now be mounted for in-air single cell experiments. The hood is then replaced with a covering plate of Plexi glass during the course of cell irradiation experiments to ease the frequent changing of samples. The design of the new chamber also allowed for the installation of additional detection and sample manipulation devices.

The Stage and the Microscopes

The sample positioning is performed by a 7-axes stage from Feinmess, Dresden. It includes x-, y- and z-translational movements and θ-, ϕ-, x'- and y'-goniometric motion. The vertical y-motion is controlled by a stepper motor with an accuracy of $1\,\mu m$. All other motions are driven by piezoelectric motors. The overall x, z positioning accuracy is $0.5\,\mu m$ and $0.015°$ and $0.005°$ for θ and ϕ, respectively. The total travel along the x-axis is $50\,mm$ and along the z-axis $25\,mm$. All stage movements are triggered by a software installed on the computer managing the data acquisition. The sample can be monitored all the time by means of digital cameras that process the signals from two custom-made optical microscopes (Thalheim Spezial Optik, Germany) installed in the chamber. The microscope for front view of the sample is at $45°$ off beam axis, just above the RBS detector. It has a field of view of $6.0\,mm \times 4.5\,mm$ at a working distance of $65\,mm$ and is corrected for the tilted plane of focus. The microscope for the rear view is fixed behind the sample on a support that also hosts the STIM detector and the Faraday cup and that can be moved using a linear motion feedthrough. The rear microscope has a better resolution ($1\,\mu m$) than the front microscope. An LED (cold light) ring illuminates the sample for visualisation.
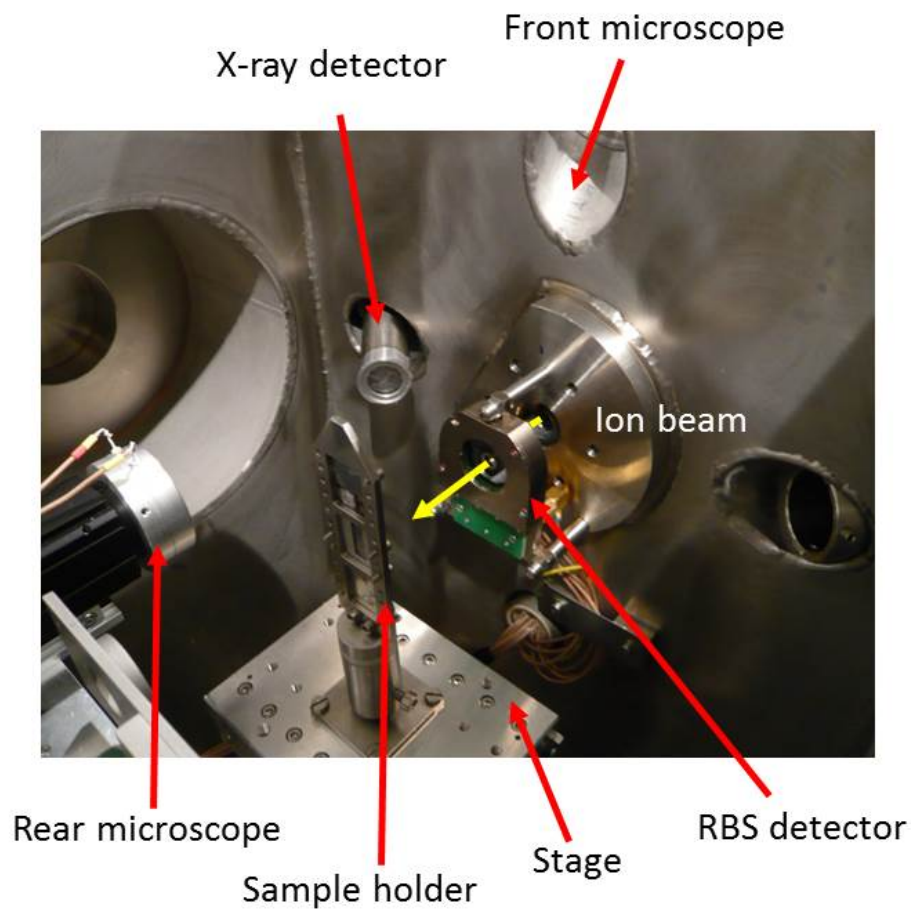
Figure 3.2: The interior of the sample chamber.

The Detectors

A Positive Intrinsic Negative (PIN) diode S1223 from Hamamatsu is employed as the STIM detector. The preamplifier based on Amptek A250 is housed in the same box as the PIN diode to provide mimimum capacitance and effective shielding yielding an energy resolution of 5.4 keV for measurements in vacuum with 2.25 MeV protons. As the STIM detector sits on an adjustable support together with the microscope and the Faraday cup, it can be used both for on-axis and off-axis measurements.

A custom-designed segmented annular Passivated Implanted Planar Silicon (PIPS) detector from Canberra is placed at 180° to the beam direction for registering the backscattered particles. The total solid angle subtended by all five segments is 100 msr. It has an energy resolution of 20 keV for 2.25 MeV protons.

The new chamber was designed to accommodate two PIXE detectors at positions symmetric to the beam axis, namely at 135° and −135°. Simultaneous use of two detectors will increase the solid angle of detection and, consequently, the sensitivity of the method

for lower irradiation time. Since the old EG&G Ortec IGLET-X photon detector could not be repaired satisfactorily after its breakdown, only the newly purchased Canberra GUL0110 was available for X-ray detection. It is a liquid nitrogen-cooled high-purity germanium (HPGe) semiconductor detector with an active area of $100\,mm^2$ and an energy resolution of $144\,eV$ for $5.9\,keV$ photons. It is mounted at $135°$ to the ion beam using a sealed retractable bellow with a scale. The solid angle thus subtended by the detector can be controlled by the linear displacement on this scale, i.e. the distance between the detector crystal and the focal point of the ion beam. The maximum solid angle is $\Omega = 150\,msr$. At this position, however, four of the five segments of the RBS detector are partly shadowed by the detector tube. Only the fifth segment is then used in RBS analysis.

Charge Measurement

The total charge applied to the sample is derived by integrating the beam current over the period of measurement. Three possibilities of charge measurement are available at the nanoprobe. Two of them are available in the chamber and the third so-called pre-aperture current pick-up method is installed in the aperture box and explained in chapter 4. Since the sample holder is electrically isolated from the rest of the chamber, the beam current can directly be measured from the sample holder. The reading is, however, enhanced by $20-30\%$ due to the emission of secondary electrons. Another way of current measurement is by means of a Faraday cup. The cup is constructed entirely from graphite and is embedded in a teflon housing. Its shape of a long cylinder with closed base reduces significantly the falsification due to secondary electrons. The choice of graphite as the conducting material is a conscious one as any metallic conductor will result in unwanted contributions to the PIXE spectrum.

3.4   Data Acquisition System

Together with the nanoprobe the Micro Probe Data Acquisition System (MPDAS) was purchased from MARC Melbourne as well. The system can process data from four different detectors simultaneously. It has four analog-to-digital converters, which digitize the height of the amplified analog signals from the detectors. Each event in the detectors is coded with the detector that generated the event, the energy of the quantum, and x and y coordinates of the beam. The events are transferred in order of their occurrence to the computer that controls the MPDAS and saved there in a list mode file. The same computer is used to visualise the data online. The element maps can be generated from the energy spectrum, while still being recorded. Since this computer also drives the scanning unit, the position of the beam is always known and shared with MPDAS. The program MpScan controls how the ion beam is scanned over the sample surface. A common scanning pattern is the raster scan. But triangle shaped scans are possible as well. The triggering of the beam from one pixel to another can be defined based on dwell

time, amount of charge collected per pixel or any external trigger. A total of 4096×4096 pixels can be generated, where the central pixel has the coordinates (2047, 2047).

Chapter 4

A Novel Method of Charge Measurement

4.1 Introduction

The precise determination of the total incident charge upon the sample is the basis of quantitative microanalysis. A general approach for measuring the charge while scanning biological samples is to put the Faraday cup behind the sample, since the thin tissues are transparent for the energetic ion beam. However, the total integrated charge in the Faraday cup is influenced by the secondary electrons knocked out from the sample by the traversing ion beam. Another option would be to first measure the beam current directly in the Faraday cup without the sample and then deriving the total charge just by integrating the beam current over the measurement time. The accuracy of this method depends on the stability of the beam current, which is rather difficult to judge. This inaccuracy can be compensated either by periodic measurement of the backscattering yield from a beam chopper [Bar00] or by deflecting the ion beam periodically into a Faraday cup [Auz06]. This reduces effective beam current and still relies on the assumption that current is stable during intervalls.

4.2 Pre-aperture Current Pick-up

A novel, non-interceptive, and non-blanking way of measuring charge was developed in the course of this work [Bar10] (appendix A). The idea was to make use of the variation of beam brightness with the divergence and the spatial extent of the beam. It has been found that the brightness is not homogeneous across the spatial extent of the beam, rather it peaks in the paraxial region [Szy97]. The brightness is higher in the central part of the beam compared to the periphery. It is suggested that the distribution of plasma in the ion source and the subsequent acceleration of ions are responsible for this distinguished shape of the brightness. The brightness is influenced mainly by accelerator parameters and beam collimating object and aperture diaphragms. Once the beam has

been formed, the shape of the brightness distribution should not vary. Therefore, for a given accelerator and collimator configuration the ratio of central brightness to peripheral brightness should remain constant. After determining this ratio the beam current in the paraxial region can be inferred by monitoring the current in the peripheral region. The idea is implemented with a set of copper plates placed just before the aperture diaphragm as shown schematically in figure 4.1.
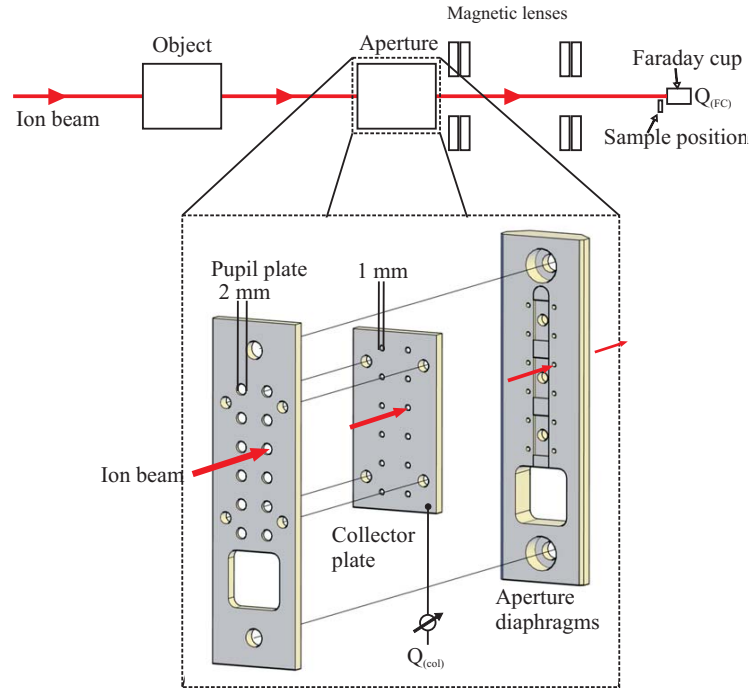

Figure 4.1: A novel approach for measuring and monitoring the beam current. A pair of Cu plates in front of the aperture diaphragms measures the current from the peripheral region of the beam.

A front plate (the pupil plate) collimates the ion beam through a 2 mm hole followed by a rear plate (the collector plate) with a 1 mm hole. This collector plate measures the peripheral current and lets the central part of the beam go unobstructed through the aperture diaphragm. A Faraday cup placed behind the sample holder without the intervening sample measures the current from the paraxial region of the ion beam. The ratio of total integrated charge at both positions Q_{Col}/Q_{FC} is determined. This ratio should stay constant if the beam parameters are not changed. Test measurements showed that this ratio was constant over the whole day. For $100\,\mu m/300\,\mu m$ object/aperture setting Q_{Col}/Q_{FC} was determined at an interval of 30 min for a period of 7 h (fig.4.2). The ratio must be determined for each object/aperture settings or if the accelerator settings are changed. Figure 4.3 shows the effect of changing the extraction voltage by $0.1\,kV$ on the Q_{Col}/Q_{FC} ratio. Due to the technical implementation of the pre-aperture plates, the

ratio is always above 10. This facilitates the fluence determination for low beam current ($< 1\,\text{pA}$) applications (e.g. proton beam writing) where conventional charge/current measurements are no longer appropriate [MEN07]. In this way, the minimum measurable fluence can be decreased by the ratio $Q_{\text{Col}}/Q_{\text{FC}}$.
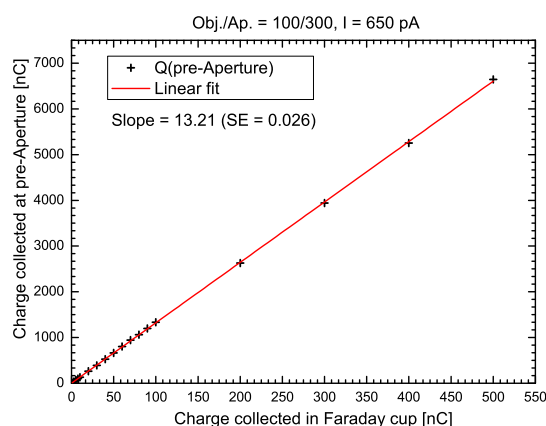

Figure 4.2: Total charge measured at the collector plate compared to the measurement of charge in a Faraday Cup at sample position without intervening sample. The ratio is constant over the whole day.
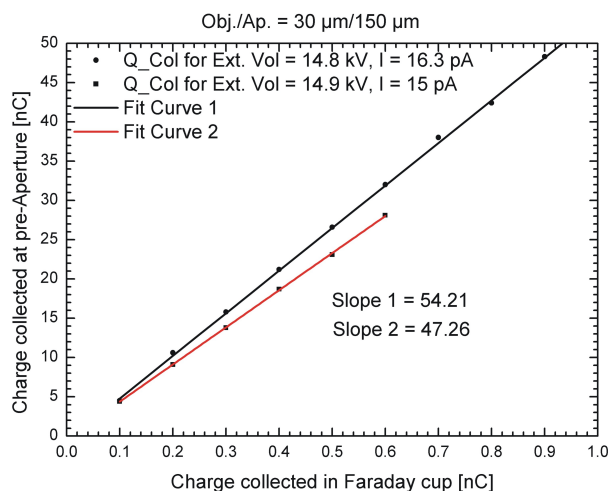

Figure 4.3: Effect of changing the accelerator parameters on the ratio $Q_{\text{Col}}/Q_{\text{FC}}$. Here, the extraction voltage is changed by $0.1\,\text{kV}$.

Chapter 5

The Workflow

The nuclear microscopy investigations of the biological specimens require elaborate planning and preparation. There is no unique standard operating procedure for the quantitative analysis of organic matter. Depending on the type of the specimen and the property to be measured the sample preparation and the measurement workflow has to be devised. In general, the sample preparation involves the fixation, the mounting and the preparation of thin sections of the specimen. The measurement workflow includes identification of the optimal ion beam parameters like the beam current, the scan size, the spatial resolution etc., estimation of the measurement time and measurement of the local mass density and the element concentration. The large specimens are measured segment-wise and their quantitative element maps are reconstructed based on the sample stage co-ordinates and/or feature recognition.

5.1   Sample Preparation

The book by [Lla96] discusses at length a variety of specimen preparation methods for biological materials. A very brief description of a selection of methods is presented here.

Fixation

In order to map the element distribution that is representative of the true *in vivo* state, it is important to keep the *ex vivo* time to a minimum and to avoid contaminations due to external reagents. Cryofixation is a process that preserves the morphology and the element distribution by rapidly freezing the specimen. For the quantification of diffusible electrolyte elements in the *drosophila* head (sec.7.2) the specimens were cryofixed. However, often a single specimen has to be analysed by different techniques. So, it is not desirable to freeze the specimen as it may lead to the formation of ice crystals, which may rupture the cellular barriers and alter the structure of proteins. Though this does not hamper the analysis by ion beam methods, it may render the specimens unsuitable for biochemical analysis. The formation of ice crystals can be restricted by rapidly freez-

ing the specimen with a cooling rate of $10^4\,\mathrm{K\,s^{-1}}$ and above. The specimens can also be preserved by dehydration or fixation by aldehydes (sec.6.2). A drawback of such methods is the possible redistribution or washing out of the mobile substances like electrolyte elements from the specimen.

Sectioning

In principal, the section thickness for nuclear microscopy can vary from a couple of hundreds of nanometres to the bulk analysis of an unsectioned specimen. The sections are considered thin if the loss in energy incurred by the traversing ions can be neglected and the X-ray absorption is negligible. In bulk analysis the ion beam looses its entire kinetic energy within the sample. Figure 5.1 shows the range of 2.25 MeV protons in a biological tissue of composition $C_{24}H_{62}NO_{13}$ and of density $0.99\,\mathrm{g\,cm^{-3}}$. The simulation gives a mean range of around 90 µm. It is evident from the simulation that the beam resolution deteriorates as the ion beam traverses deeper in the sample. The lateral straggling of the proton beam is just over 2 µm. The thinner the sections, the less is the spreading of the ion beam. However, the X-ray fluorescence yield decreases, too, as the integrated cross-section for electronic excitations decreases with the decreasing thickness. In practice, the lower limit of the section thickness is dictated by the technical possibilities to prepare such thin sections and the integrity of the specimen. In most of the cases the specimen sections are between 5 µm to 15 µm. This ensures a robust section, homogeneous beam resolution along the beam trajectory and excludes overlapping cellular structures.

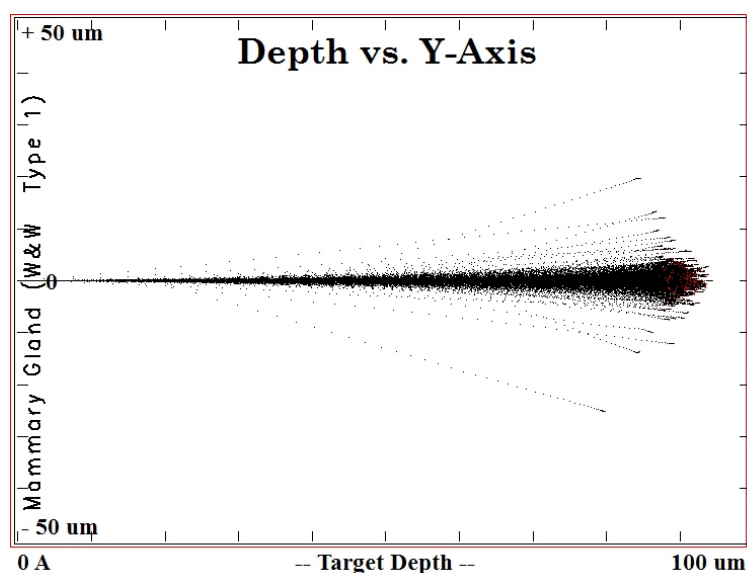Figure 5.1: A simulation of the range and the straggling of 2.25 MeV protons in a biological tissue of density $0.99\,\mathrm{g\,cm^{-3}}$ by SRIM.

The cryofixed specimens are sectioned in the frozen hydrated state in a cryomicrotome,

where the knife and the ambient temperature is around $-20\,°C$. The chemically fixed specimens are commonly mounted in paraffin to provide a stable substrate for preparing thin sections. These sections then have to be deparrafinised before the final embedding in a polymer foil for the quantitative analysis.

Supporting foils

The specimen sections are embedded in thin supporting polymer foils like Mylar, PE, PET, Formvar etc. These specimen backings stabilise the thin sections for analysis by an energetic ion beam. Obviously, the foils should be free of any elements that are to be quantified in the specimen. There are few ways of picking the sections on the foil. In cryomicrotomy the frozen sections can be picked on a pre-cooled foil and let to thaw and dehydrate at the room temperature. The sections can also be picked on a fresh coating polymer resin like DePeX on a glass slide that is still viscous and let to dry. Again, if the redistribution of the diffusible elements is a concern, the sections should be freeze-dried before mounting them on the supporting foils. However, the freeze-dried sections are particularly fragile and require enhanced stabilisation. The freeze-dried *drosophila* sections (sec.7.2) were sandwiched between two thin layers of a plastic film, Parafilm. The sections from paraffin mounted specimens are taken on glass slides first for deparafinisation. Afterwards, a coating of a DePeX is applied on the top of the glass slides and is let to dry. Subsequently, the dried film is peeled-off from the glass slide and the specimen comes along with it.

5.2   Measurement

Table 5.1: Typical beam spot sizes and currents for different object and aperture diaphragm settings.

Object diaphragm (µm)	Aperture diaphragm (µm)	Beam spot size (µm)	Beam current (nA)
50	200	0.5	0.120
100	300	0.8	1.0
200	300	1.5	4.5
200	500	1.6	8.3
300	500	2.2	17

The beam current can be regulated by the object and the aperture diaphragms and the beam spot size is defined by the object diaphragm and the demagnification factor. Table 5.1 lists typical beam spot sizes and currents for various combinations of object

and aperture diaphragms. The choice of a particular setting depends on the size of the sample region to be analysed, the desired spatial resolution and the sensitivity, and the measurement time. For example, small sample areas like the drosophila eye and antenna were measured with 0.5 µm beam spot at 120 pA, whereas the macro-dimensional section of rat brain was measured with the object and aperture diaphragm setting of 200 µm and 300 µm, respectively. Table 5.2 lists typical MDLs for various elements quantified in a dopaminergic neuron. The total charge accumulated on the sample was 0.31 µC for a scan area of 50 µm × 50 µm. The measurement time was around 43 min.

Table 5.2: Typical MDLs for various elements quantified in a dopaminergic neuron in µmol/l.

Charge	P	S	Cl	K	Ca	Fe	Ni	Cu	Zn
0.31 µC	256	601	95	63	56	41	7	12	52

Sensitivity is, among others, a function of total charge. The higher the total charge, the lower is the MDL. Table 5.3 lists the MDL for three representative elements, phosphorus, potassium and iron in three different measurements with a varying amount of total charge. As the total charge increases, the sensitivity increases. The improvement in the sensitivity is directly proportional to the square root of the increase in charge. A section of the drosophila head was measured with a sensitivity of 5 µmol/l for Fe. However, the effective sensitivity per unit area is relatively poor in the drosophila head section, as the scan area is large and the charge per unit area is very low. For a spatial resolution of 1 µm, the MDL in a single pixel ($1\,\mu m^2$) for Fe is $5\,\mu mol/l \times \sqrt{800 \times 800} = 4\,mmol/l$. In spatially resolved analyses the areal charge density is a very important factor. A neuron, though measured with a relatively poor sensitivity of 41 µmol/l for iron, has a higher effective sensitivity per unit area (0.45 mmol/l) for a spatial resolution of 0.5 µm.

Table 5.3: Minimum detection limit as a function of total charge.

Sample	Scan area	Charge	Charge density	P	K	Fe
	(µm)	(µC)	(pC/µm²)	(µmol/l)	(µmol/l)	(µmol/l)
Neuron	50 × 50	0.31	122	256	63	41
Rat brain	3200 × 3200	6	0.6	160	72	11
Drosophila head	800 × 800	7	11	57	31	5

In case of the section of rat brain, the scan area is in square millimeters. It is difficult to achieve the same spatial sensitivity as in the case of neuron, since the total charge required would be very high. The measurement time then would be very long. In such cases, the measurement time can be reduced by measuring at higher current. In Large Area Mapping (chap.9) high beam currents are required for a time-efficient processing of

the samples. Increasing the beam current also helps in improving the MDL in small area scans. The neuron in table 5.3 was measured at $120\,\mathrm{pA}$ and required $43\,\mathrm{min}$. Another neuron that was measured at $240\,\mathrm{pA}$ for $32\,\mathrm{min}$ had a MDL of $25\,\mathrm{\mu mol/l}$ for Fe. Single neuron measurements have been performed with an areal charge density of up to $1\,\mathrm{nC/\mu m^2}$ [BAR07].

Areal density

The element concentrations determined by PIXE are normalised to the areal mass density for a better intercomparability of areas with varying mass densities. There are two methods with which the areal mass density of a specimen can be determined, namely STIM and RBS. The physical basis of these methods has been explained in section 2.1 and section 2.2, respectively. In STIM just few ions per pixel are sufficient to obtain information on the areal mass density, whereas in RBS significantly more charge needs to be accumulated on the specimen for a statistically secure determination of the local matrix composition. The accuracy of both these techniques has been compared by measuring standard foils and cultured cells in a published study [DEV01]. The authors concluded that for the standard foils both techniques give results with reliable accuracy, whereas STIM provides more accurate results for the cultured cells. One of the advantages of the backscattering method is that it can be employed simultaneously with PIXE and its spectrum can be used to deduce the amount of accumulated charge during the sample irradiation.

Simultaneous PIXE and RBS measurements were used in all the applications reported in this work. Additionally, a software was developed for the visualisation of the areal mass density of various specimens measured by STIM. This program was mostly used in the analysis of cultured single cells [KOL08, WER09].

5.3   Analysis

The measurement data is recorded in an event-file. As described in section 2.2 and section 2.3 the BS events and the PIXE events are sorted and processed by RUMP and GeoPIXE II, respectively. The charge and the matrix composition is determined by RUMP. This information is used by GeoPIXE II to generate quantitative elemental images of the specimen. Apart from the depiction of the spatial distribution of the element concentration in false colours, the software also offers various tools for the region-of-interest analysis and the extraction of concentration profiles.

High-definition PIXE

The maximum deflection of the ion beam is $\pm 1.6\,\mathrm{mm}$ along both the x and y axes. This gives a maximum scan size of $3.2\,\mathrm{mm} \times 3.2\,\mathrm{mm}$. Larger specimens, as in chapter 9, can only be measured segment-wise. For a faithful reconstruction of the entire element distribution map an area of overlap is to be maintained between the adjacent scans.
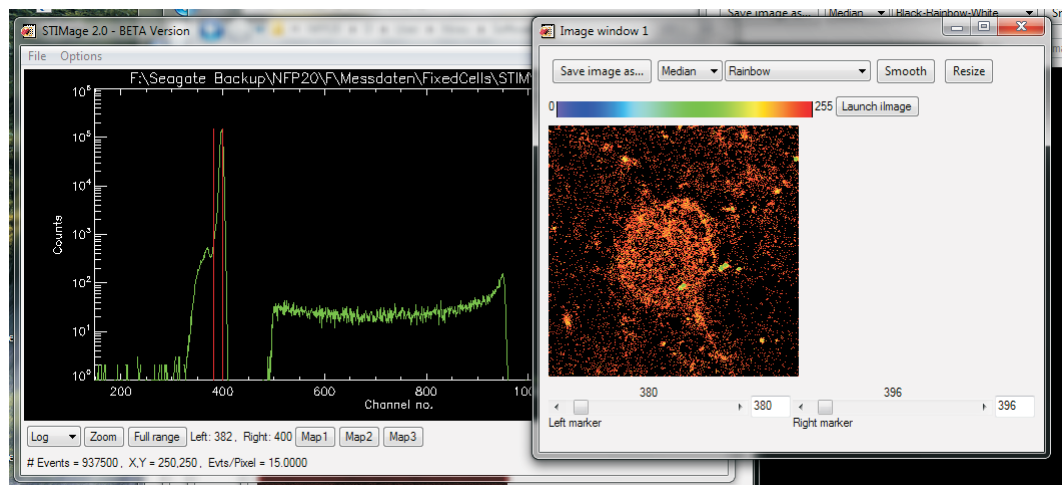
Figure 5.2: A screenshot of the STIMage software developed for creating energy loss maps from STIM spectrum. On the left is a STIM spectrum of a single cultured cell using 2.25 MeV protons. On the right is an energy loss map of the same cell. The events between the two red markers in the spectrum are mapped in the image.
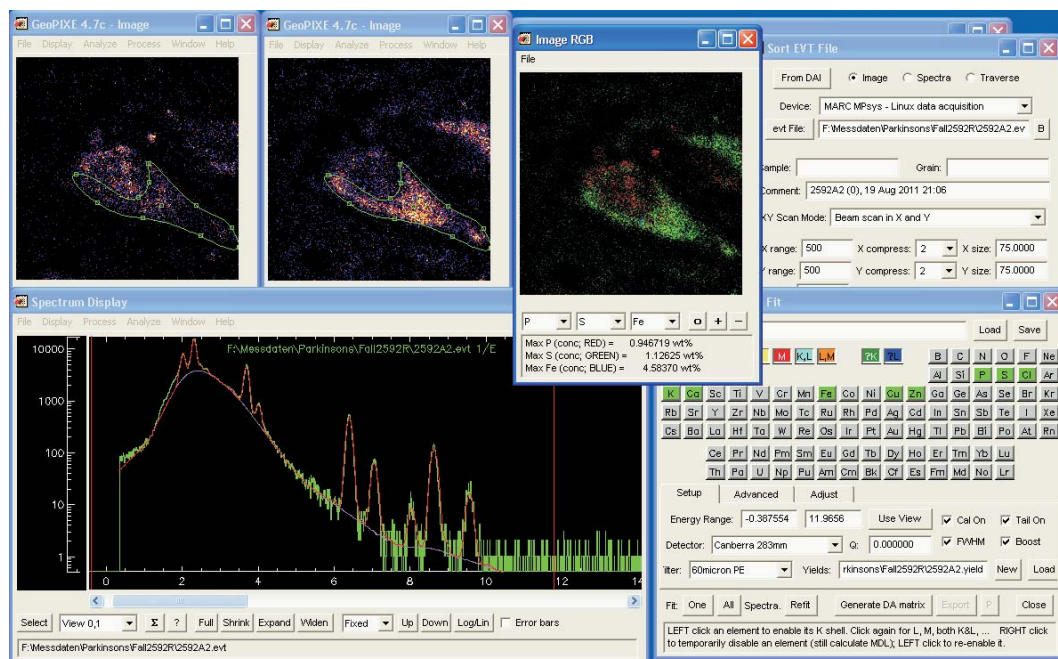

Figure 5.3: A screenshot of the GeoPIXE software shows the typical flow of PIXE data. The PIXE spectrum is first fitted to calculate the concentration of elements. The event-file is then sorted to generate quantitative element maps.

In order to process the large specimens in a time-efficient manner, the measurements are performed at high beam currents. The technical setup at LIPSION allows a high beam current density in a micrometre-sized beam spot (tab.5.1). Since in a single scan

a maximum of 4096×4096 pixels can be set, the resulting elemental mosaic has a high density of pixels. With the spatial resolution in low-micrometre region the quantitative elemental images of the macro-dimensional specimen are of high-definition.

PIXE Stacking

3d elemental maps of the specimen can be created with tomographic PIXE measurements [ROT10]. However, the calculation of accurate element concentration in PIXE tomography (PIXE-T) gets complicated as one has to correct for the beam broadening effects, changes in the ionisation cross-section along the ion track and the attenuation of the fluorescence yield within the sample [SAK97, MH05, BEA08]. On one hand, the samples have to be prepared free standing in order to avoid inaccuracies due to the mounting media. On the other hand, a free-standing sample would deteriorate readily as a result of high fluences employed in PIXE-T. Andrea et al. performed limited angle tomography of single cells grown on a substrate to overcome the sample preparation limitations [AND10].

PIXE-stacking is an alternative way for creating 3d element maps of biological specimens that cannot be prepared free standing. In this, thin serial sections of the specimen are prepared and measured by conventional 2d PIXE. The resulting quantitative maps are then stacked consecutively on each other and aligned to reconstruct a quantitative element distribution volume. For thick samples that cannot be measured by PIXE-T, PIXE-stacking is the only alternative. An induced atherosclerotic lesion in a murine coronal artery has been measured by PIXE-stacking at LIPSION (chap.8), and the results are published in [SIC12].

5.4   Sources of error

In general, the nuclear microscopy is considered as a non-destructive analytical technique. However, the interaction of the energetic ions with the target specimen leads to certain changes in the specimen that can influence the quantification procedure. As described in chapter 2 the energetic particles deposit a part or the whole of their kinetic energy in a thin or thick target specimen, respectively. The deposition of energy can lead to, among others, a rise in the local temperature of the specimen, breaking of the chemical bonds, a loss of the volatile elements from the specimen and the shrinkage of the specimen. Depending on the beam current density and the measurement time these effects can be grave or negligible. The damages in organic matter due to MeV ions have been described in detail in [LLA96, WAT97, REI01a].

In biological specimens, apart from the optical changes like charring and shrinkage that are observed in the irradiated areas [WAT88], compositional changes occur as well. Mainly a loss in oxygen and hydrogen content has been observed [WAT97, REI01a]. The evaporation of residual water content in the biological specimens is considered as one of the reasons for it. Fortunately, no change in the concentration of minor and trace elements was observed [WAT97]. However, the loss in H and O content changes the areal mass

density of the specimen. The knowledge of the exact areal mass density is essential for an accurate quantitation. Further, the spatial resolution of the element maps suffers due to the shrinkage of the specimen.

It is suggested to determine the native areal mass density of the sample by the more conservative STIM, before doing the PIXE analysis. The areal mass density is required in the analysis of PIXE spectra to correct for the matrix effects. Since the loss of matrix elements occurs mainly in the initial short period of the scanning time, pre-analysis STIM would lead to an overestimation of the areal mass density and the subsequent matrix correction factor.

Thin sections of the specimens should be prepared to minimise the heating up of the sample and the absorption of X-ray in the sample. Increasing the solid angle for PIXE increases the detection efficiency, and hence, reduces the scan time. Also, the highest possible scanning frequency should be preferred. Further, optimising the proton energy for maximised X-ray output helps in reducing the scan time. The general rules for measuring biological samples in a conservative way are outlined in [Lla96].

In spite of observing these general rules, the analysis is not free from error. The systematic error stems from the uncertainties in the parameters like the total charge, the sample thickness, the fluorescence yield, the stopping power, the detection efficiency etc. The statistical error, on the other hand, stems from the uncertainty in determining the element peak area. This error can be neglected when the number of events in the peak is relatively large. In a blind test the accuracy of analysis by GeoPIXE II was found to be within 3% [Fed95]. However, the systematic error is higher in the analysis of biological specimens as the effects of beam damage are difficult to judge. Also, the variability of the local areal mass density that is inherent to the biological specimens adds to the uncertainty in the quantitation. In general, the systematic error is assumed to be around 10%. The comparision of element ratios from different measurements can lower the error in analysis.

Chapter 6

Parkinson's disease

6.1 Introduction

Parkinson's disease (PD) is the second most common neurodegenerative disease after Alzheimer's disease in the industrialised nations. It affects around 1% of the general population above the age of 60 years and every year 8 to 18 new cases are reported per 100 000 persons [Lau06]. It is projected that by 2030 around 8.67 million persons will be suffering from PD world wide [Dor07]. This disease was first described by an English physician Sir James Parkinson in 1817 in a book called "An essay of shaking palsy". The early symptoms are unilateral resting tremor, slowness in movements (bradykinesia), muscle rigidity and postural instability. Within few years of the onset all the symptoms are visible. Depression, sleep disturbance, and difficulty in speech are also caused by the disease. The pathological hallmarks of this disease are selective loss of dopaminergic neurons in *substantia nigra* (SN), loss in striatal dopamine content and the intracytoplasmic presence of numerous Lewy bodies. Both striatum and SN are part of basal ganglia that are located in the mid-brain region. The basal ganglia is involved in the regulation of posture and muscle tonus with dopamine as the main neurotransmitter. Striatum, which has the highest level of dopamine in the brain [Car59], receives dopamine from the SN. Degeneration of 50 to 60% of dopaminergic neurons in the SN and depletion of 70 to 80% of striatal dopamine is manifested in people dying with overt parkinsonism [Ehr60] [Mar90]. Since the aetiology of the PD is unknown, only the symptoms are treated. The levels of dopamine in striatum are restored by administration of the drug levodopa. The pathogenesis of PD and its treatment are reviewed by Olanow and colleagues in [Ola99, Ola04].

Neuromelanin

The literal translation of *substantia nigra* is 'dark substance'. The presence of a browny-black pigment called neuromelanin (NM) makes the SN appear dark. NM is present mainly in the SN and locus coeruleus region of the human brain. The absolute concen-

tration of NM in SN *pars compacta* (SNpc) increases with age and can go up to 3.5 µg/g [Zec02]. The same study also found that in age-matched Parkinsonian subjects more than 50% of NM is lost. The most vulnerable dopaminergic neurons in PD are pigmented with NM. There is a direct correlation between the degree of NM pigmentation of dopaminergic neurons and their vulnerability [Hir88]. This makes NM a subject of investigation for the role it plays in the pathogenesis of PD. It has been suggested that NM chelates metal ions, which otherwise would induce oxidative stress and damage neurons [Fed05]. While NM has a protective role during its synthesis, it may induce chronic neuroinflammation and neuronal loss once the host neuron dies and sets its pigment free. The protective and toxic characteristics of neuromelanin are discussed by Zecca et al. in [Zec03].

Role of Iron

The mechanisms that trigger the selective death of pigmented dopaminergic neurons in SN have not yet been identified unambiguously. Of many possibilities, an elevated oxidative stress as a cause for the disease onset has been studied extensively. See [Jen03] for a review of the oxidative stress hypothesis in PD. Indeed, the pars compacta region of substantia nigra is vulnerable to oxidative stress due to high dopamine metabolism, which results in hydrogen peroxide formation. As described in section 1.3 iron and copper are capable of producing cytotoxic radicals by reacting with peroxide. As iron is the most abundant metals in brain, an overload or availability of free reactive iron will result in oxidative stress. Increased oxidative stress in SNpc has been evidenced by postmortem studies. Riederer et al. observed a significant increase in total iron and a significant decrease in antioxidant glutathione in the severe cases of PD [Rie89]. A range of histochemical, spectroscopic, anatomical and atomic techniques have since measured qualitatively, semi-quantitatively and quantitatively a selective increase in total iron content in the Parkinsonian SNpc with varying sensitivities. Interestingly, few studies reported no change in iron content in Parkinsonian SN compared to control. Götz et al. have reviewed these studies in [Göt04]. However, there is a lack of cellular classification in these studies. Mostly, the iron content is determined in whole SN or in the zona compacta of SN [Rie89, Dex89]. Good et al. measured the element content bound to NM granules, whereas Hirsch et al. differentiated between NM and NM free regions in SN. There are different stores for iron in the brain. Iron can be stored as ferritin in neurons, microglia, oligodendrocytes, and NM granules. Zecca et al. have reviewed the relevance of iron in brain ageing and neurodegenerative disorders [Zec04]. No studies are known that have differentially measured these iron depots. Nonetheless, there is a general belief that iron is increased in SNpc in PD.

   The present study was undertaken to investigate the iron overload hypothesis in PD. In order to assess the location and the factor of increase in iron in Parkinsonian brains differential measurements of SNpc were performed with nuclear microscopy techniques.

6.2   Materials & Methods

Thirteen brain samples were obtained from the Brain Bank of the University of Leipzig. Six brains were from patients with idiopathic PD (aged 75(5) years), six were non-demented controls (aged 68(4) years) and one was a demented control. Non-demented control brains were from subjects without any history of neuropsychiatric disorders or mental impairment and the demented control brain was from a patient with Alzheimer's disease (AD). In AD the SN is not affected. The Ethical Committee of the University of Leipzig has approved the case study. Brains were preserved by fixation with 4% para-formaldehyde in 0.1 M phosphate-buffered saline (PBS) at pH 7.4. The mid-brain region encompassing the substantia nigra was dissected and processed for sample preparation. The dissected material was mounted in paraffin using conventional protocols for paraffin embedding and block mounting. Paraffin blocks containing the substantia nigra were sectioned in 6 µm thick sections. These sections were deparaffinised with xylene and rinsed with ethanol. The sections were mounted on glass slides with DePeX (Merck) as mounting medium. After 24 hours the sections were brought on the sample holders by peeling them off with the help of double sided adhesive tapes.

The SNpc was analysed differentially using quantitative ion beam microscopy. A 2.25 MeV proton beam at 250 pA with a beam diameter below 1 µm was used. The element content was quantified in neuromelanin aggregates, extraneuronal environment and the microglia cells by simultaneous PIXE and RBS measurements. The element concentration is calculated in mmol/l, and the results for both groups were pooled and analysed using a two-tailed Student's t test. Differences in element content are considered significant for $p < 0.05$.

6.3   Results

Figure 6.1 shows an optical image of a dopaminergic melanised neuron, its phosphorus and sulphur element maps, and a three-element RGB map of phosphorus, sulphur and iron. The RGB map shows an overlap of green and blue colour in the area with neuromelanin. It means that iron is mainly bound to sulphur rich neuromelanin. The phosphorus map is an indicator of cellular structures. The nucleus, its membrane and the cell membrane are seen distinctly in the phosphorus map. Cell bodies like microglia are also rich in phosphorus and can be easily identified in the P map. For differentiated quantification of element distributions ROIs were placed around neuromelanin, microglia and in the extraneuronal space devoid of any visible cellular structures.

Neuromelanin

The precise structure of neuromelanin is not yet known. In PIXE maps sulphur is observed to be strongly correlated with the neuromelanin extent. This suggests that sulphur is one of the major constituents of neuromelanin. Figure 6.2 shows element profiles along a
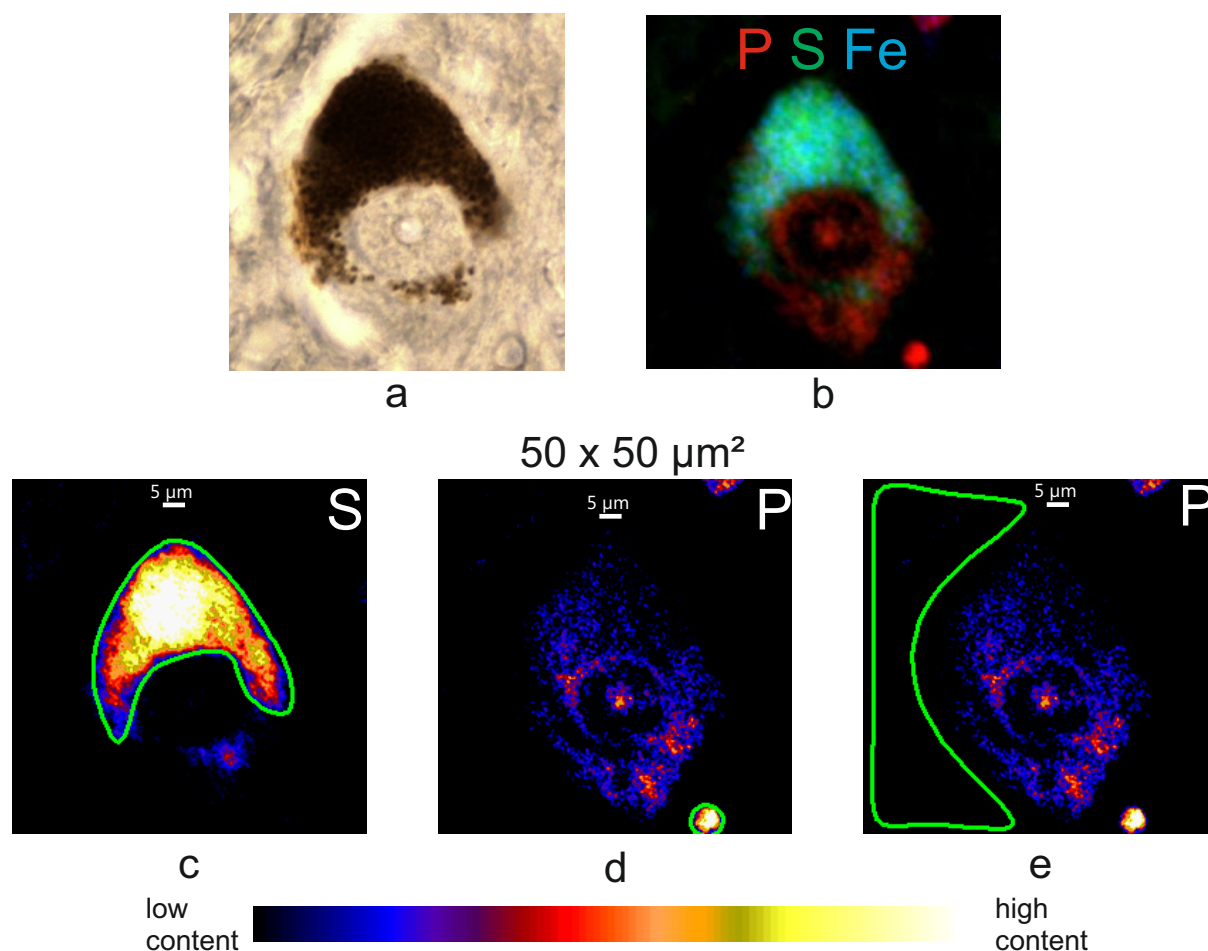
Figure 6.1: (a) An optical image of a melanised neuron in SNpc. (b) A 3-element RGB image of the same neuron showing co-localisation of S and Fe in NM. (c) S map as NM indicator for region of interest (ROI, in green) analysis of NM. (d) P map as indicator for microglia cells (bottom right) and cell body. (e) Extraneuronal ROI.

traverse through three NM containing neurons. A strong co-localisation of sulphur and iron in the NM granules is seen. Hence, the sulphur map is used to define a region of interest (ROI) for quantification of elements bound to neuromelanin. Table 6.1 lists average molar concentrations of various elements in neuromelanin of PD and controls. The values are presented as mean $\pm$ standard error of mean (SEM) for a total of 65 neurons from six Parkinsonian cases, 46 neurons from six non-demented control cases and 16 neurons from one demented non-Parkinsonian (AD) control case.

The phosphorus concentration at around 100 mmol/l is nearly equal in both Parkinsonian and non-demented control cases, whereas it is almost half (55 mmol/l) in the only demented control case.

The sulphur concentration in non-demented control cases is 308 mmol/l. There is a significant increase in the sulphur content of Parkinsonian neuromelanin. At 389 mmol/l
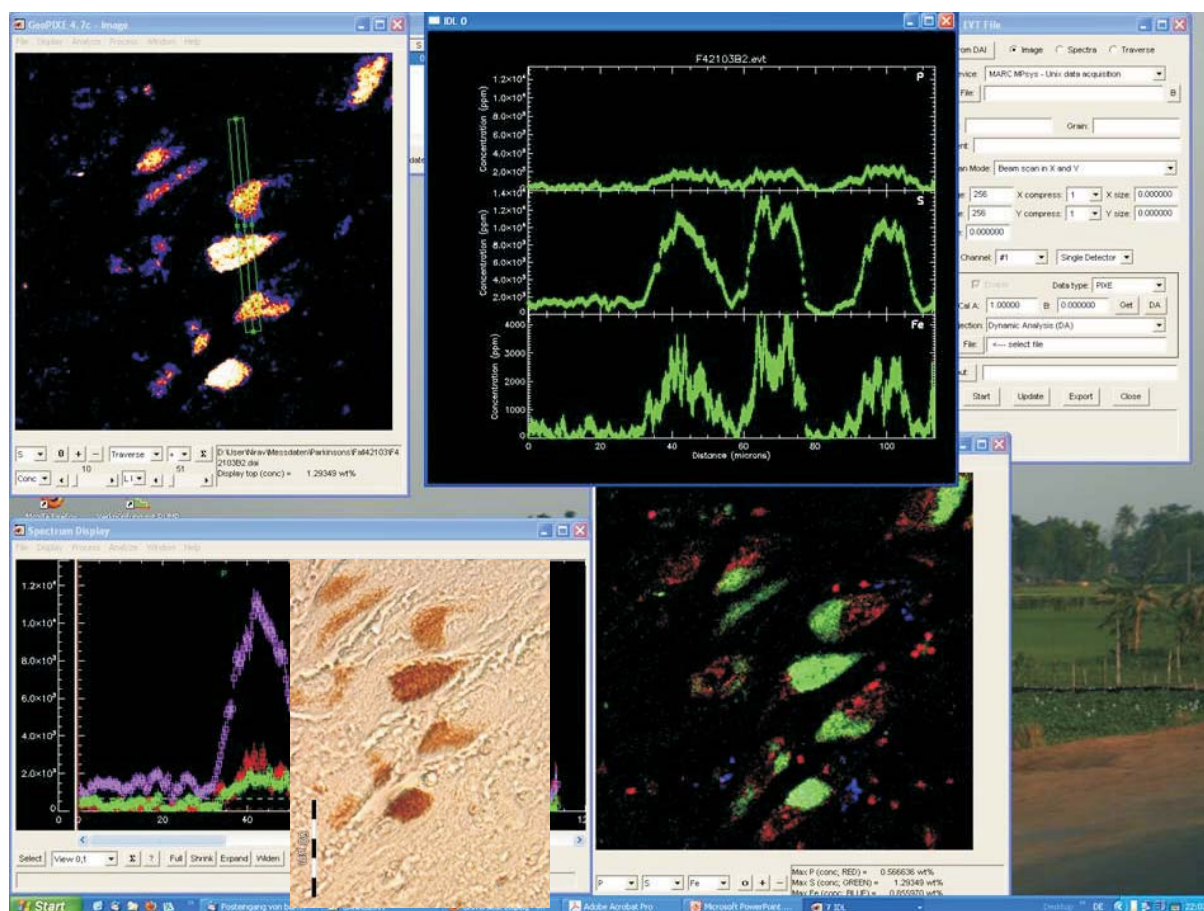
Figure 6.2: Top: A traverse through NM containing cells shows the co-localisation of iron and sulphur in the NM granules. Top of the traverse represents left of the element profile. Bottom: An optical image and a three-element RGB map of P, S and Fe.

the increase is around 26%. Similar to phosphorus, AD has the lowest sulphur content.

A clear trend is seen in the potassium levels. The lowest concentration (2.6 mmol/l) was measured in the non-demented controls. It is around three times and four times higher in AD and PD, respectively.

No significant change was observed in the calcium amount for non-demented controls and Parkinsonian cases. The Ca concentration was found to be less in the AD neuromelanin. At 9.2 mmol/l it is less than half of the other groups.

With an average concentration of around 32 mmol/l the iron content bound to neuromelanin was not significantly elevated in Parkinsonian cases compared to the non-demented controls. Only the AD neuromelanin has slightly less iron bound to it (25 mmol/l).

Copper is present at very low levels in neuromelanin. The mean concentration in the non-demented controls is 0.92 mmol/l and no significant variations were observed in the demented cases.

Zinc was measured to be 3.24 mmol/l in the non-demented control. Twice as much

zinc was found in Parkinsonian neuromelanin and 40% less zinc was present in AD control.

Table 6.1: Element concentration in neuromelanin.

Element	PD	Control (non-demented)	Control (AD)
	mmol/l	mmol/l	mmol/l
P	100±9	101±10	55±6
S*	389±33	308±28	236±16
K*	11.0±1.5	2.6±0.3	8.0±1.5
Ca	20.5±2.2	20.1±2.0	9.2±0.9
Fe	32.6±3.0	32.1±3.4	24.9±2.0
Cu	0.82±0.06	0.92±0.09	0.82±0.09
Zn*	6.53±0.74	3.24±0.40	1.92±0.18
Fe/S	0.085±0.004	0.099±0.003	0.112±0.010

* Student's t-test, $p < 0.05$

Microglia

Microglia cells are macrophages that scavenge dead neurons and foreign bodies. They are an integral part of the immune defense mechanism and respond first to any pathological changes in the brain. Microglia can be identified in the phosphorus map as $\approx 5\,\mu m$ diameter circular objects with a very high phosphorus content. A total of 46 Parkinsonian, 31 non-demented control and 8 AD microglia cells in the vicinity of the dopaminergic cells were analysed. Quantitative results of elements present in microglia are presented in table 6.2.

Phosphorus, the glia indicator, is 1.8 times higher in the Parkinsonian case than in the control. There is no significant difference in phosphorus content between both controls. A 100% increase in sulphur level is measured in Parkinsonian microglias relative to control. Again, both the controls had similar amounts of sulphur. Like in neuromelanin, the trend in potassium content is also reflected in microglia. In Parkinsonian cases the potassium concentration is 12.6 mmol/l and in non-demented control 2.5 mmol/l. 4 mmol/l K was measured in the AD case. Significant elevations in calcium levels are observed in both, the Parkinsonian group, and the AD case. 1.4 times higher Ca content was found in Parkinsonian cases when compared to non-demented controls. Around two times more iron is present in the Parkinsonian group than in controls. As in neuromelanin no significant changes in the copper content are observed across the three groups. A higher level of zinc is observed in Parkinsonian cases than in controls. At 9.3 mmol/l the Zn concentration is 3.5 times higher than control.

Table 6.2: Element concentrations in microglia.

Element	PD	Control (non-demented)	Control (AD)
	mmol/l	mmol/l	mmol/l
P*	236±16	131±10	122±8
S*	146±12	71±6	67±4
K*	12.6±1.0	2.5±0.5	4.0±0.1
Ca*	13.7±1.2	9.9±1.0	12.6±0.9
Fe*	27.7±3.3	13.1±1.6	11.9±2.3
Cu	1.84±0.39	1.16±0.25	1.36±0.19
Zn*	9.30±2.46	2.64±0.50	1.04±0.27

* Student's t-test, $p < 0.05$

Extraneuronal environment

A non-neuronal non-glial area is chosen as extraneuronal environment. Elements quantified in this region are presented in table 6.3. 1.6 times more phosphorus and 1.4 times more sulphur is present in the extraneuronal space in PD than control. However, depleted levels of both these elements are observed in AD. The trend in potassium content is true for the extraneuronal environment as well. In AD 50% more potassium is present than in the controls, in PD it is 3.6 times higher. There is a significant increase in calcium concentration in the Parkinsonian group. 63% more calcium is present in this region than in the control. Although there is a slight increase in Fe content as well, the difference is not significant. Iron is depleted in AD. Copper is present in the extraneuronal region in minute but quantifiable concentration. 0.24 mmol/l Cu is present in the AD case. It is above the limit of quantification, which is three times the minimum detection limit of 50 µmol/l. Zinc is found to be around 6 times higher in the Parkinsonian group than in the non-demented control.

6.4   Discussion

There seems to be increasing evidence of elevated iron levels in the total substantia nigra of patients with Parkinson's disease. The increase ranges from 1.22 to 3.40 times [Göt04]. This evidence is not conclusive as the same review also lists studies from three different groups that did not find any significant changes in the nigral iron content. It is being reasoned that the different stages of PD and varying sensitivities of the detection methods contribute to such discrepant findings. In fact, Riederer et al. measured significant differences in iron content only in the severe cases of PD, but not in the mild forms [Rie89]. Nevertheless, it is a common belief now that iron is increased in SN in PD. However, there

Table 6.3: Element concentrations in extracellular environment.

Element	PD	Control (non-demented)	Control (AD)
	mmol/l	mmol/l	mmol/l
P*	30.7±4.1	19.9±1.3	15.0±2.2
S*	81.9±8.3	58.5±5.3	38.9±4.4
K*	3.3±0.4	0.9±0.1	1.3±0.3
Ca*	5.8±0.6	3.6±0.3	1.8±0.2
Fe	8.2±1.0	6.1±1.2	3.5±0.5
Cu	0.38±0.03	0.32±0.04	0.24±0.03
Zn*	6.20±0.89	1.04±0.16	0.23±0.03

* Student's t-test, $p < 0.05$

is a lack of spatial information on the iron increase. Mostly, the whole SN is homogenised and the iron content is measured by spectroscopy using reference standards. Dexter et al. published concentrations for total SN and zona compacta in SN [DEX89], whereas Good et al. just measured iron and aluminum bound to NM [GOO92]. Distinction was made between element content in the neuromelanin free region and elements bound to neuromelanin in SN in a Wavelength Dispersive X-ray Microanalysis (WDXMA) study by Hirsch and colleagues [HIR91].

Apart from the major elements phosphorus and sulphur, the most abundant elements in SNpc are iron and calcium, whereas potassium, zinc and copper are present in small but quantifiable amounts. In non-demented controls the distribution of these elements is non-uniform. Although the lowest concentration of these elements is found in the extracellular matrix, the distribution of potassium, copper and zinc can be considered as relatively even. Iron and calcium, on the other hand, show markedly uneven distributions. Neuromelanin has most of these elements, followed by microglia and least in the extracellular region. Hence, neuromelanin is a major store of iron in SNpc.

Significantly, the amount of iron bound to neuromelanin is not increased in PD. This result is in contradiction with a Laser Microprobe Mass Analyzer (LAMMA) study on NM granules by Good et al [GOO92]. They measured an average increase of 45% in iron bound to neuromelanin in three Parkinsonian cases. Since iron is stored in NM granules as ferritin [TRI09], the degree of pigmentation will determine the total amount of iron that NM can bind. Also, the degree of NM pigmentation varies from cell to cell. Normalisation of iron content by NM constituent sulphur should provide a better intercomparibility of non-uniformly pigmented neurons. But, they reported no sulphur concentration. In this study, the iron to sulphur ratio is significantly decreased by 16% in PD, whereas no difference is observed in the controls and the AD case. In the X-ray microanalysis study [HIR91] the element contents are reported as ratio to potassium, as the potassium levels did not vary within the SN. Interestingly, they also measure a significant 35% reduction

in iron bound to neuromelanin in Parkinsonian SN.

It is also important to note that there is a significant increase in sulphur content of Parkinsonian NM. The average age of the Parkinsonian subjects was 75 years compared to 68 years for the controls. The increase in sulphur content can be due to the increase in NM with age [Zec02] as sulphur is a building block of NM. It is also possible that, the NM in PD is modified. Indeed, a NMR/EPR study on Parkinsonian NM revealed a change in iron binding properties of NM, suggesting a progressive migration of iron from NM to cytosol [Fas06]. In this case the neuronal death could be triggered even by physiological levels of iron in SN. The increase in sulphur content of NM can be interpreted as synthesis of more NM granules, which could be a compensatory mechanism for checking the loss in its affinity towards iron.

The increase in potassium content in neuromelanin is difficult to interpret given that it is an electrolyte element prone to redistribution in solvent based sample preparation procedures. Since both, control and Parkinsonian samples, are prepared in same manner, the increased potassium concentration has to be native. Potassium ions are mainly required for maintaining the membrane potential and in nerve signalling. Dying neurons in PD might set cytosolic potassium ions free. However, it remains unclear, whether neuromelanin actively chelates the potassium ions from the extraneuronal milieu or they are 'washed' into NM by sample treatment.

An increase in zinc content in SN has been reported by [Dex89]. They found 54% increase in zinc in SNpc. As SN is in a state of heightened oxidative stress, antioxidant activity must also be increased. Zinc is a cofactor of many antioxidant enzymes and its increased concentration can be related to the activity of antioxidants.

Microglias are the resident macrophages in the central nervous system that respond to immune injuries. Once activated, they not only phagocytose invading pathogens, but also scavenge toxic cellular remains and help in tissue repair by secreting growth factors. Neurodegeneration as a result of activated microglias is an alternative hypothesis in PD. The role of microglia in the pathogenesis of PD is reviewed in [LS09]. Except for copper all quantified elements are elevated in Parkinsonian glias. A 100% increase in phosphorus, sulphur and iron content of Parkinsonian microglia is due to its activation and continuos phagocytosis of dead neurons and NM. Significantly, only the potassium and calcium content is increased in the demented control. Since there is no loss of nigral neurons in AD, the levels of phosphorus, sulphur and iron are close to non-demented controls.

The presence of necrotic material in the extracellular region is reflected in the elevated levels of phosphorus, sulphur, potassium and calcium. But the increase in iron is not significant. Again, more zinc in extraneuronal space can be attributed to increased presence of antioxidants.

6.5 Conclusion

The SNpc is analysed with a sub-micron spatial resolution to distinguish between NM, microglia and neuropil (extracellular matrix) element concentrations. The element content

is quantified in neuromelanin, in microglia cells, and in extraneuronal space. Six Parkinsonian cases are compared with six non-demented control cases and one demented-control case (AD). Sulphur maps are used as neuromelanin indicator and phosphorus maps as microglia indicator. The region apparently devoid of any visible cellular structures is considered as extraneuronal space.

Iron was found to be localised in the neuromelanin granules. No significant elevation in iron level bound to neuromelanin was found in Parkinsonian cases. The neuronal iron overload hypothesis in PD cannot be sustained in this spatially resolved analysis. In fact, a significant decrease in the iron to sulphur ratio was observed in the Parkinsonian cases. This suggests a modification of neuromelanin in PD. Perhaps, the neuronal death in PD is caused by free iron that is progressively released from NM due to its altered binding properties.

A significant increase in the content of most of the quantified elements was observed in microglia cells of Parkinsonian cases. This increase in the element content can be attributed to the increased scavenging of dead neurons and free neuromelanin. The presence of neuronal debris is reflected in the increased concentration of P, S, K and Ca in the extraneuronal region. An increase in zinc in the extraneuronal region can indicate augmented presence of the antioxidants.

Chapter 7

Drosophila melanogaster

7.1 Introduction

Drosophila melanogaster, also known as the fruit fly or the vinegar fly, is a widely used model organism in biological research, particularly in the field of genetics. The main reasons for its extensive use are a fully sequenced genome, a short life span, a fast replication cycle, the ease of care, and the cost effectiveness. Since 77% of the human disease genes have similar counterparts in *drosophila*, it is a brilliant model for studying the human diseases [REI01B].

The techniques used in *drosophila* neurobiological experiments are often disruptive. In order to maintain physiological conditions an isotonic solution similar to the Drosophila's body fluid, the lymph, is applied. A common artificial lymph is Ringer's solution. It consists mainly of ions of the electrolyte elements Na, Cl, K and Ca. Its recipe varies according to the organ or the body part to be investigated. For studying the olfactory system of the fruit fly it is of great interest to know the concentration of these ions in the brain, the antenna and its sensilla hairs, and the associated organs like the mouth parts and the compound eye. The methods of ion beam analysis were employed to quantify ion concentrations in these organs with a high spatial resolution. The results are published in [REI11]. A qualitative description of the distribution of elements in the drosophila head is given in the following sections. See appendix B for a full quantitative discussion.

7.2 Materials & Methods

Drosophila melanogaster wild type flies (wild type Berlin) aged 1-3 weeks were used. Since the subject of interest are the electrolyte elements, care has to be taken not to influence the location of these elements while preparing the sample. Any solvent based treatment might lead to a redistribution or flushing out of the electrolyte elements. So, the living flies were put in a custom-made, long cylindrical container and filled with an O.C.T. compound (Tissue-Tek®). This compound is widely used in cryoembedding and cryosectioning. It is a transparent, viscous fluid at room temperature and changes to a

white, opaque solid when frozen. The container with the flies was then snap frozen by immersing it in liquid nitrogen chilled isopentane. Many coronal sections of the head were prepared with a cryomicrotome. The section thickness was either $14\,\mu\text{m}$ or $25\,\mu\text{m}$. The sections were then freeze-dried. The freeze-dried sections are very fragile. To stabilise the sections for ion beam analysis, they were either sandwiched between two layers of thinly stretched-out plastic films or placed on a thin polymer film. The electrostatic force between the film and section ensures that the section does not fall off during the analysis. Given the small size of the drosophila head, it was imperative to use the best possible beam resolution to map the element distribution. The measurements were performed with a beam spot size of $0.5\,\mu\text{m}$ at $250\,\text{pA}$. RBS and PIXE data are acquired simultaneously and processed by RUMP and GeoPIXE II, respectively, to obtain the quantitative element distribution maps of the brain, the compound eye, the antenna and its sensilla hair and the mouth parts.

7.3   Results & Discussion

Apart from the major elements C, H, N and O, phosphorus is the most abundant element in the *drosophila* head followed by potassium, sulphur, chlorine and calcium. The elements iron, zinc and copper are present in trace amounts. The element distribution maps of the cross-sections of the head, the compound eye and the sensilla hair reveal a markedly non-uniform distribution of various elements. The localisation of certain elements in the specific body parts may suggest a functional correlation. Figure 7.1 shows a scanning electron micrograph of the head of drosophila from literature [NIM09] (a), an optical image of a $25\,\mu\text{m}$ thick coronal section through the head (b), a three-element RGB map (P, S, Cl) of this coronal section (c), and the individual element maps. In the RGB map the brain appears largely in orange colour due to the overlap of phosphorus (red) and sulphur (green). The neurons and the glia cells are known to have high phosphorus amount due its presence, among others, in the cell membranes and phosphate molecules like ATP. Sulphur is largely present in the extracellular matrix as a component of the matrix proteoglycans[Ioz98]. Proboscis is a part of mouth used for olfactory and ingestion purposes. Its inner part is rich in sulphur, whereas chlorine is localised in the outer rim of proboscis. Also, increased iron is seen in the mouth parts. It is possible that these characteristic distributions of elements have a functional association in the ingestion processes like the stabilisation of the apparatus. The simple eyes on the top of head and the compound eyes on the lateral sides have a very high calcium concentration. The cornea on the top of eyes are composed of chitin, which is a component of the insect exoskeleton. Calcium is also present in this exoskeleton.

    The eyes located on the lateral sides of the brain of drosophila are compound structures. They are composed of many individual units of vision called the ommatidia. For an anatomical vies see figure 7.3. Within a single ommatidium there is a characteristic distribution of the elements.
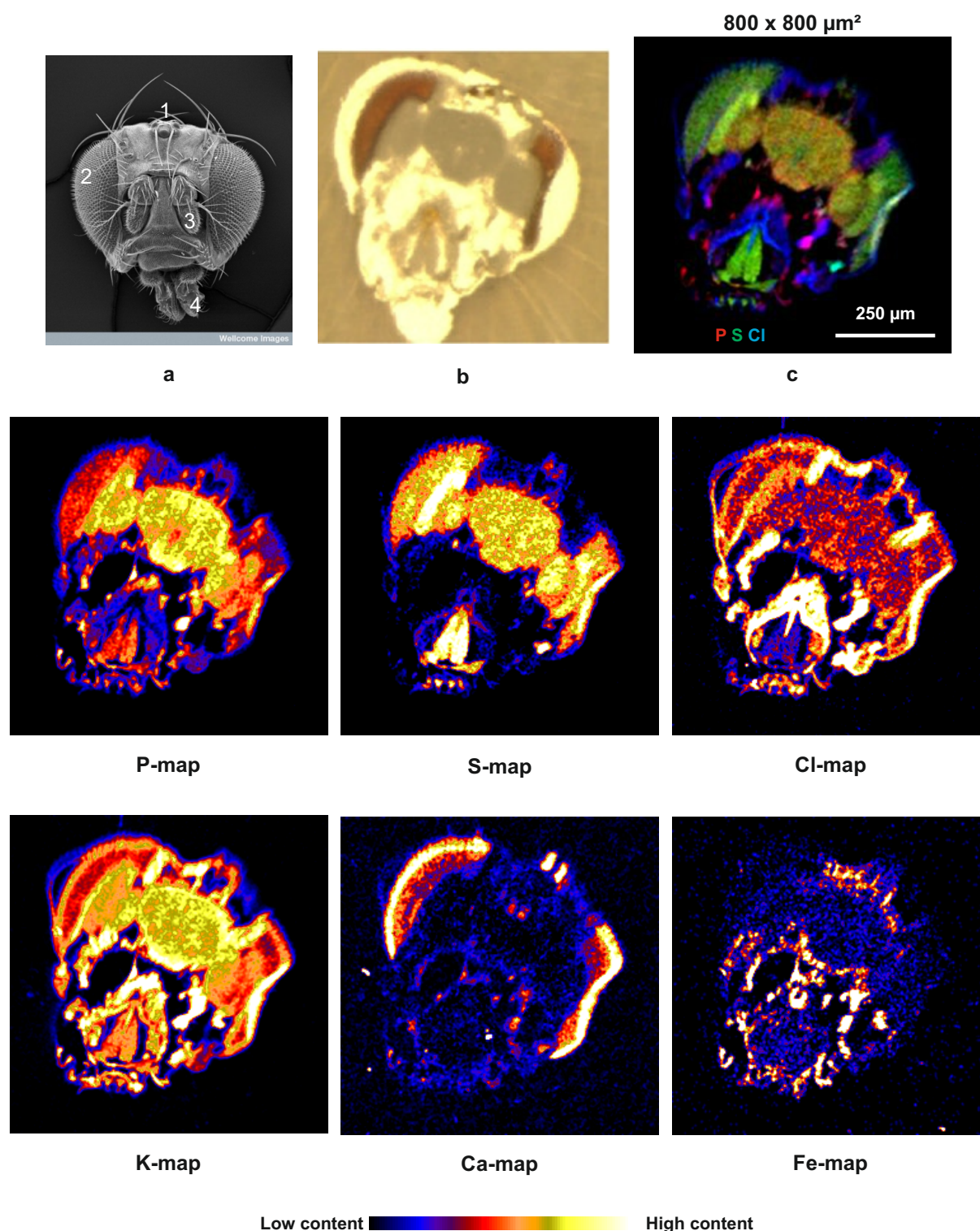
Figure 7.1: **(a)** Scanning electron micrograph of the head of *drosophila* [NIM09] showing the simple eyes (1), the compound eye (2), the antenna with sensilla hair (3), and the proboscis (4). **(b)** An optical image of a 25 µm thick coronal section of the *drosophila* head. **(c)** A three-element RGB map (P, S, Cl) of the same section. The quantitative element distribution maps are presented in the lower two rows.
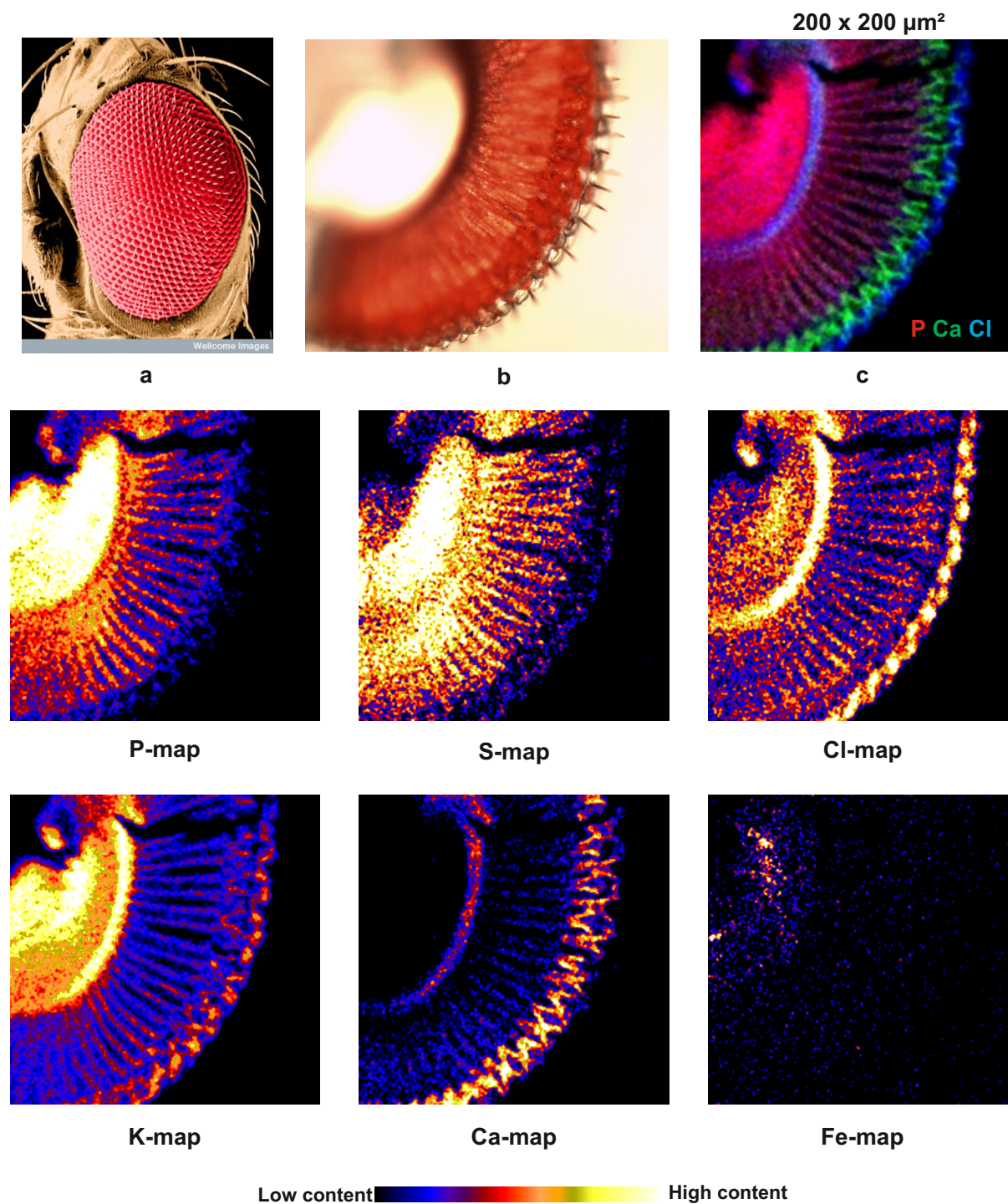
200 x 200 µm²

a

b

P Ca Cl

c

P-map

S-map

Cl-map

K-map

Ca-map

Fe-map

Low content ▬▬▬▬▬▬▬▬▬▬ High content

Figure 7.2: The top row (left to right) shows a scanning electron micrograph of the compound eye from literature [STR], an optical image of a 14 µm thick section through the compound eye of the *drosophila* and a three-element RGB map (P , Ca, Cl) of the same section. The bottom rows show various elemental maps.
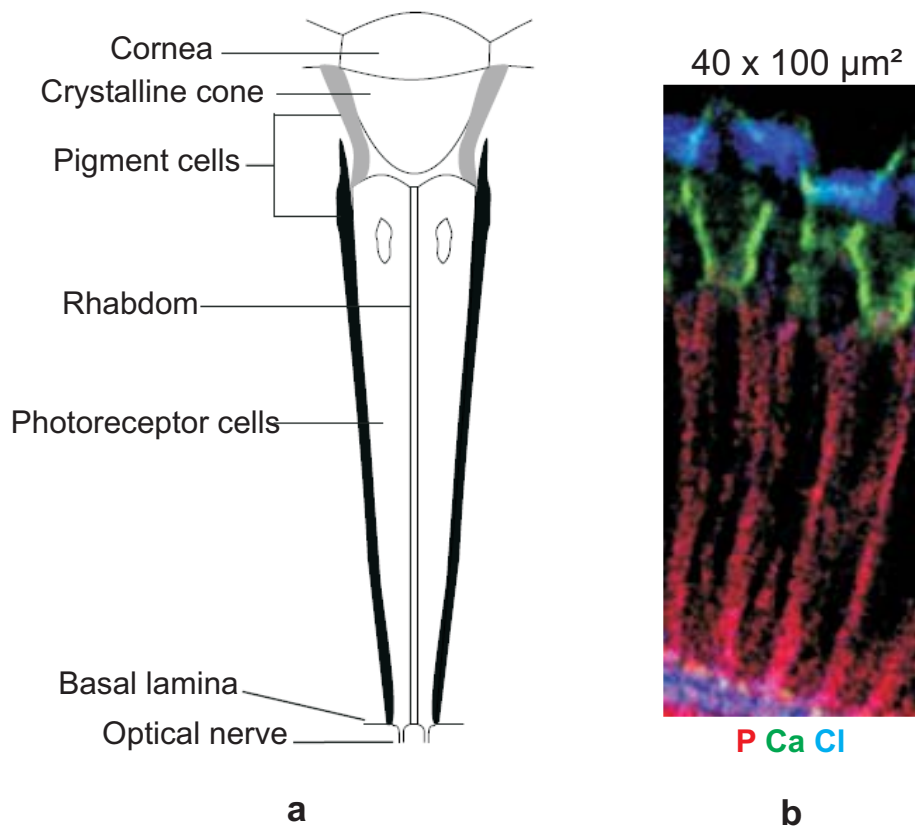
Figure 7.3: **(a)** A simplified illustration of an ommatidium. **(b)** A three-element RGB map (P, Ca, Cl) of a section through the eye reveals the compartmentalisation in ommatidia.

Figure 7.2 shows a scanning electron micrograph of the compound eye from literature [STR] (a), an optical image of an analysed section through the compound eye (b), a three-element RGB map (P, Ca, Cl) (c) as well as the element distribution maps of this section. The three-element RGB image highlights the compartmentalisation of certain elements.

The medulla (left area in red) is rich in phosphorus and potassium. It has, in addition, a high concentration of sulphur. On the other hand, the basal lamina is enriched with the electrolyte elements potassium, chlorine and calcium. The light-sensitive photoreceptor cells are seen in most of the element maps, but contain more phosphorus than the other elements. The crystalline cone has none of the measured elements. It is rather highlighted by a highly localised calcium content in the surrounding pigment cells, and chlorine and potassium content in the corneal lens on the dorsal side.

Figure 7.3 shows a simplified illustration of a single ommatidium with its various sub-units. A high-resolution three-element RGB map reflects the correlation between these sub-units and various elements. Calcium ions are an integral part of the signaling cascade in phototransduction [HAR01]. This may explain the localisation of calcium in the crystalline cone layer.

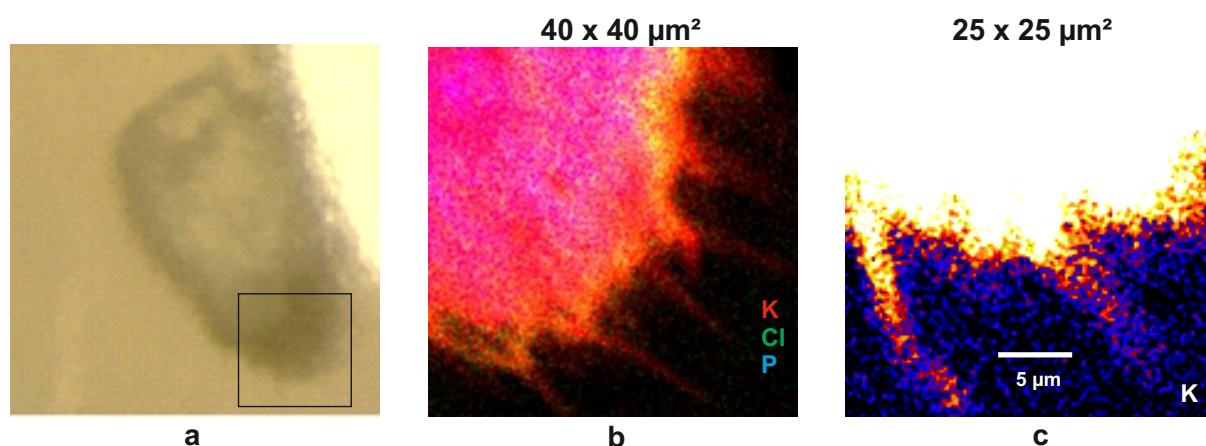The sensilla hair on the antenna are around 2.5 μm in diameter. These olfactory

Figure 7.4: **a.** An optical image of a section through the antenna. **b.** A three element RGB map (K, P, Cl) of a part of antenna showing sensilla hairs. **c.** A high resolution K map of two sensilla hair.

sensors are seen only in the potassium maps. Figure 7.4 shows an optical image of a longitudinal section through the antenna. The high-resolution potassium map reveals some fine sensilla hairs on the outer surface. The RGB map of K, P and Cl shows that though potassium and chlorine are present in the antenna lobe, the sensilla hairs consist mostly of potassium. Sensilla being a sensory organ, the presence of potassium is not surprising as potassium is an inherent part of the nerve signaling.

7.4 Conclusion

The measurement of electrolyte elements in various organs associated with the olfactory signaling in *drosophila melanogaster* was enabled by cryoembedding and non-solvent based sample preparation techniques. The elements could be quantified in their near-native state. The data is useful in preparing organ- or region-of-interest-specific Ringer's solution. The quantitative element maps of the drosophila head, the compound eye and the sensilla hair reveal selective localisation of certain elements. A functional correlation can be inferred from the presence of particular elements in the specific subunits of an organ.

Chapter 8

Atherosclerosis

8.1   Introduction

Atherosclerosis or arteriosclerosis is a multifactorial, progressive inflammatory disease of large and medium-sized arteries that carry oxygen-rich blood. It is characterised by a significant lumen-narrowing in the advanced stages. Stroke or myocardial infarction are the most common clinical manifestations of atherosclerosis. Although the genetical predisposition may play a role in the progression of the disease, atherosclerosis is considered a lifestyle disease as it is one of the major causes of deaths in the industrialised nations. The aetiology of atherosclerosis is not yet fully clear, but there exists a consensus regarding the onset and the progression of the disease. It is explained here briefly. The reviews by Ross [Ros99] and Lusis [Lus00] are considered authoritative sources of detailed information on this subject.

Figure 8.1 illustrates the anatomy of an artery wall [Sti05]. It consists of three distinct layers, the *intima*, the *media* and the *adventitia*. The *intima* is lined with a monolayer of endothelial cells towards the lumen and is separated from *media* by a layer of collagen fibers and an internal elastic lamina. The *media* is made up of smooth muscle cells, and the outermost layer *adventitia* is composed of connective tissues. According to the response-to-injury hypothesis the onset is triggered by a dysfunction of endothelium, which can be caused by several factors like high plasma cholesterol levels, smoking, hypertension etc. At the site of endothelial dysfunction the low-density lipoproteins (LDL) migrate from blood into the artery wall and are oxidised there by free radicals. The elevation of oxidative stress inside the artery wall is followed by the immune response, in which monocytes migrate across the endothelium and differentiate into macrophages. They ingest the oxidised LDL (ox-LDL) to become foam cells. This leads to enhancement of the immune response as the modified ox-LDL in the macrophages is still highly reactive [Mad04]. More and more macrophages penetrate the endothelium and turn into foam cells to form a fatty streak. As a result the smooth muscle cells migrate from media into intima to accommodate the growing amount of the extracellular lipid material by secreting fibrous elements. When the growing size of lesion can no longer be compensated by dilating the blood vessel,

the lesion starts protruding in the lumen volume resulting in high blood pressure. The protrusion is protected by a fibrous cap. Ultimately, the lesion and the arterial wall stiffen due to calcification. A rupture in the fibrous cap will lead to thrombosis and the release of plaque material into the circulation, which eventually is manifested clinically in form of a stroke or an infarction. The progression of atherosclerosis is classified in various stages according to [Sta92, Sta94, Sta95].
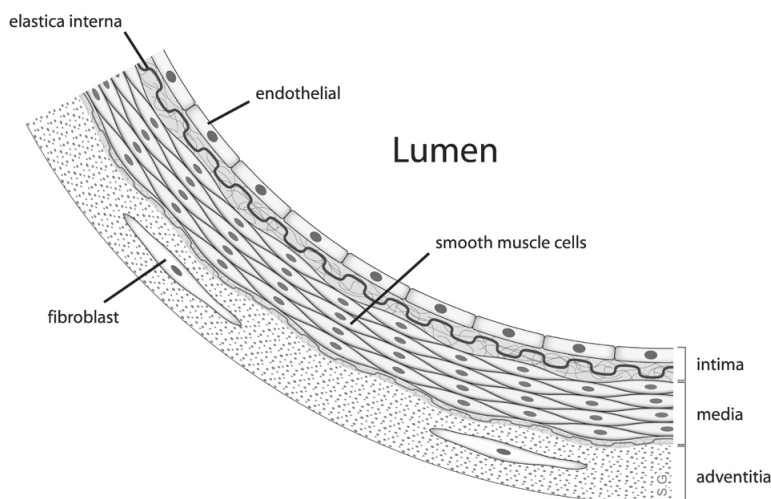

Figure 8.1: An illustration of the anatomy of an artery wall [Sti05].

Since the oxidative stress is strongly involved in atherogenesis, the role of metal ions like iron and copper comes under investigation because of their capability to induce oxidative stress. Given that the incidence and mortality of atherosclerosis is biased towards the male gender it was hypothesised that the menstrual loss of iron is responsible for the lower incidence of cardiovascular diseases in women [Sul81]. A number of studies were undertaken to prove or disprove the iron hypothesis, some of which are reviewed by Yuan and Li [Yua03] and Meyers [Mey00]. Although few studies did find a positive correlation between iron concentration levels and atherosclerosis, many of them could not discern any significant changes. As an example, Stadler et al. detected elevated levels of iron and copper in ex vivo human carotid lesions [Sta04]. However, the same group reported few years later reduced levels of iron, zinc and calcium in the lesions from type 2 diabetes mellitus subjects, who are at an increased risk of developing atherosclerosis [Sta12].

Apart from iron, copper is implicated as well in the progression of atherosclerosis for its oxidative properties. Zinc being part of metallothioneins is considered to be antioxidant, and hence, protective [Pow00]. Depleted levels of zinc may also be inferred as an impaired antioxidant mechanism.

This pilot study at LIPSION was undertaken to assess the applicability of nuclear microscopy in investigating the role of trace elements in the progression of atherosclerosis.

8.2 Materials & Methods

Animal handling

Atherosclerosis can be modeled in mutant rodents and small animals by feeding them on high fat and high cholestrol diet. Apolipoprotein E-deficient or LDL receptor-deficient mice develop atherosclerosis rapidly when raised on a high-fat and high-cholesterol diet. For this study atherosclerosis was induced in a LDL receptor-deficient mouse by raising it on a semisynthetic diet containing 4.3% fat and 0.02% cholesterol according to [TEU03]. This diet induces hypercholesterolemia and atherosclerosis at the aortic root and in the brachiocephalic arteries (BCA), but not in the aorta. The mouse was sacrificed at the age of 20 weeks. The BCA together with the aorta was resected.

Sample preparation

Atherosclerotic plaques were predominantly observed in the aortic root and the BCA. The BCA supplies oxygenated blood to the right arm, the neck and the head, and is a preferred area for lesion formation. It was cut at the branching point from the aorta and 1 mm distal to its bifurcation into the subclavian and carotid arteries (fig.8.2). It was then frozen in the O.C.T compound (Tissue Tek®) for cryosectioning. Starting from the bifurcation point 10 µm slices were sectioned from the frozen block in a cryomicrotome at $-23\,°C$. The cross-sections were picked on glass slides with a fresh coating of a polymer resin DePeX® (Serva). After the resin had dried, the sections were transfered to aluminum frames for the ion beam analysis. A few adjacent sections were processed for the histochemical analysis.

Ion Beam Analysis

A 2.25 MeV proton beam at 600 pA with a beam diameter around 1 µm was used to measure the artery sections. Simultaneous RBS and PIXE measurements provided information on the local matrix composition and the element concentration, respectively. The part of the arterial wall without lesion served as a control to elucidate changes in the element concentration in the lesion. Four cross-sections of the BCA were measured. In each section three regions were analysed for the element content. The lesion area, the artery wall hosting the lesion, and the part of the artery without any lesion as control. Differences in element content were analysed using Student's t-test and were considered significant for $p<0.05$.

8.3 Results

Figure 8.3 shows an optical phase contrast image of a section through the aorta and the quantitative element maps of the area with lesion. Although non-significant, the spread of the lesion is observed in the optical image of the aorta. The phosphorus map reveals
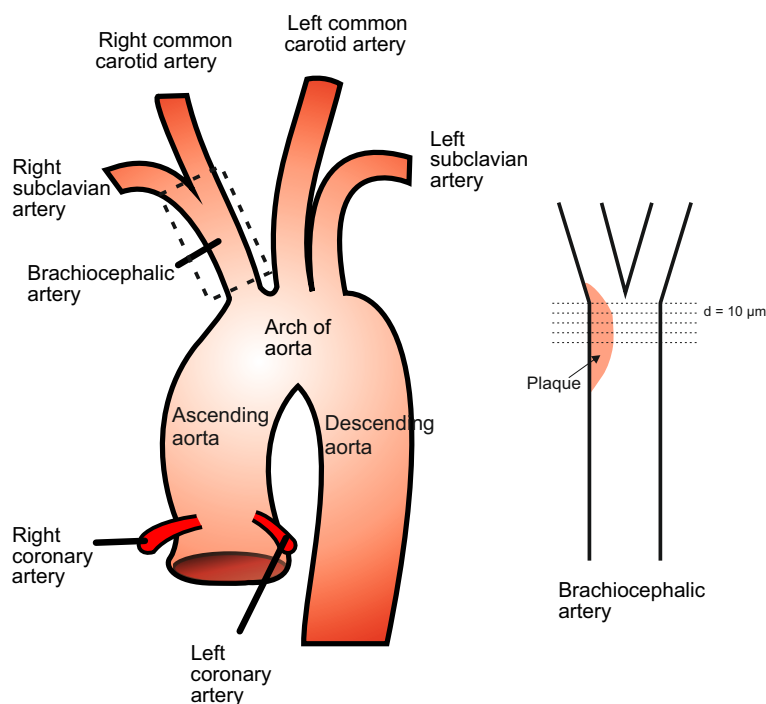
Figure 8.2: Illustration of major arteries branching from the aorta (modified version based on [Rhc]) and the sectioning of brachiocephalic artery.

the layered structure of the arterial wall. The intima is modified due to the lesion. The presence of Ca suggests the onset of calcification of the arterial wall, although the lesion is not advanced. Fe is mostly seen in the distal region of the adventitia that is rich in connective tissues.
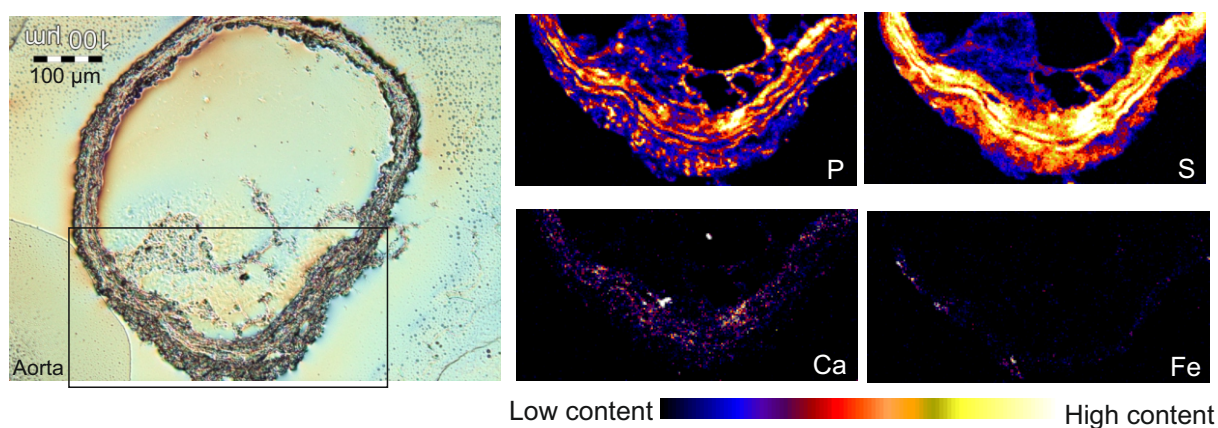

Figure 8.3: An optical image of a cross-section through aorta and the quantitative element-distribution maps of the artery with lesion.

There was a significant lesion formation in the BCA. Figure 8.4 shows an optical

image of a section through the BCA that was used for ion beam analysis. The presence of lipids and macrophages in the lesion is established by the histochemical analysis of adjacent sections. Cluster of Differentiation 68 (CD68) is a glycoprotein expressed in the macrophages. Markers to this protein are used for the identification of macrophages. Light red colour in the staining confirms the presence of macrophages inside the intima. Lipid deposition within the arterial wall is confirmed by the dark red colour due to staining by Oil red O dye.
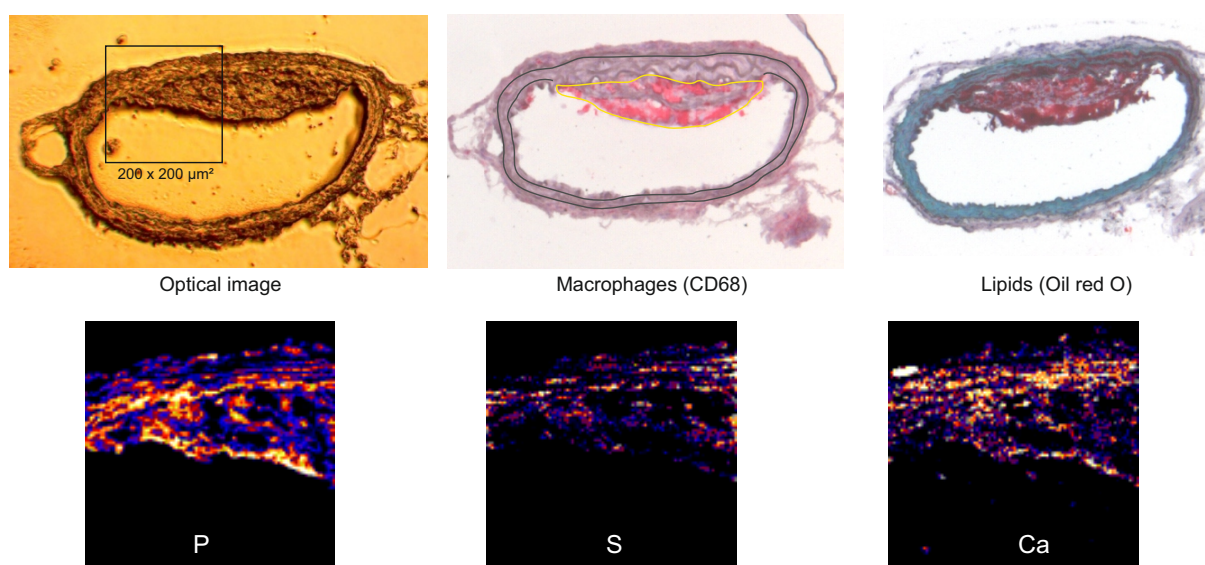
Figure 8.4: Upper row (left to right): An optical image of a cross-section through BCA that is used for ion beam analysis, CD68 stain for the macrophages and Oil red O stain for lipids in the adjacent sections. Lower row: Phosphorus, sulphur and calcium distribution maps of the rectangular region shown in the upper left image.

Table 8.1 lists P, S, Ca, Fe, Cu and Zn content in the lesion, the artery wall with overlying lesion and the control artery wall. There is a non-significant tendential increase in the phosphorus concentration from the control artery wall (40.1 mmol/l) over the lesioned artery wall (47.4 mmol/l) to the lesion area (49.6 mmol/l). Sulphur concentration is significantly enhanced in the artery wall adjacent to the lesion. At 9.97 mmol/l the concentration is three times higher than in the control artery wall. A slight non-significant increase in Ca concentration is observed in the artery wall at the lesion site. The lesion concentration of S and Ca does not vary significantly from the control artery. Iron concentration, on the other hand, is slightly elevated in the lesion (0.39 mmol/l) and no change is observed in the artery wall with lesion (0.26 mmol/l) compared to the control artery wall (0.23 mmol/l). Copper concentration in the lesion (0.021 mmol/l) is near the limit of quantification (LOQ) and hence, not unambiguously quantifiable. A trend is observed in the depletion of Zn concentration. It is highest in the control part of the artery (1.04 mmol/l) and lowest in the lesion area (0.33 mmol/l).

Table 8.1: Mean element concentration in various regions of
the atherosclerotic brachiocephalic artery.

Element	Artery wall (control) mmol/l	Artery wall (lesion) mmol/l	Lesion mmol/l
P	40.1±6.2	47.4±13.6	49.6±5.2
S*	3.38±0.59	9.97±1.44	3.36±0.61
Ca	2.43±0.49	3.80±0.59	2.31±0.42
Fe	0.23±0.09	0.26±0.01	0.39±0.17
Cu	0.060±0.016	0.037±0.018	0.021±0.003
Zn*	1.04±0.21	0.76±0.12	0.33±0.06

* Student's t-test, $p < 0.05$

8.4   Discussion

As discussed by Lusis, the lesion grows initially towards the adventitia until a critical
point is reached. This is accompanied by the production of extracellular matrix, which
is initiated by macrophages by secreting growth factors [Lus00]. Sulphur is a building
block of the extracellular matrix [Ioz98]. The modification of the arterial wall at the
lesion site is reflected in the increased concentration of S.

The increase in Ca concentration in the lesioned artery wall is indicative of the onset
of calcification. The fact that Ca is not elevated in the lesion means that it is not yet
fully advanced. Deposition of microscopic granules of calcium in the lesion is observed in
early stages of the atherogenesis. As the lesion advances the calcium content increases
[Sta00]. Calcification of the artery walls is the hallmark of an advanced lesion. The
causes of calcium deposition are still unknown. Roijers et al. applied the methods of
ion beam analysis to determine the ratio Ca/P. They found it to be between 1.6 and
3.0, corresponding to amorphous calcium phosphate [Roi11]. The Ca/P ratio was found
to be 2.9 in an extended study with advanced lesions [Sic12] (see appendix C). Figure
8.5 shows a three-element map of P, S, and Ca distributions in red, green and blue
colours, respectively, for a section of BCA with an advanced lesion. Further, an element
association map shows the correlation of Ca and P in the section. All the pixels in the
element distribution maps that have a Ca/P ratio of, for example, 2.5 are highlighted in
green colour. The highlighting underlines the deposition of calcified microsopic granules
in the lesion as well as the calcification of outer arterial wall.

Iron is considered as the source of oxidative stress due to its prooxidant properties.
Watt et al. analysed quantitatively the iron, copper and zinc content of the induced
atherosclerotic lesions in New Zealand White rabbits [Wat06]. They report a 7-fold
higher iron concentration in the lesion than the artery wall. When the rabbits were treated
with iron chelating desferrioxamine, the lesion growth was inhibited. Although there was
a tendential increase in the iron concentration in the lesion, it was not significant. Iron
level may increase as the lesion advances. In fact, in a subsequent study with advanced
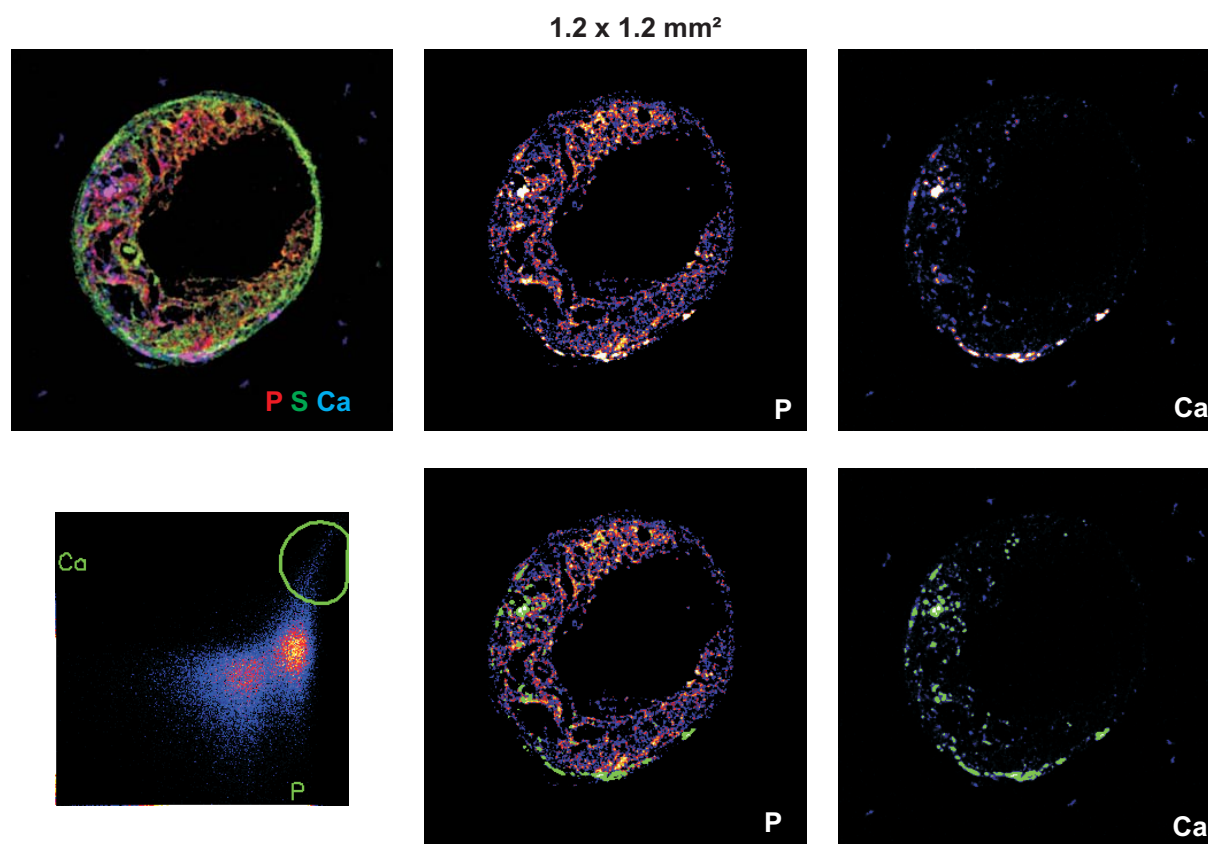
1.2 x 1.2 mm²

Figure 8.5: Upper row (left to right): A three-element map of a section of BCA showing P (red), S (green) and Ca (blue) distributions. A P intensity map, and a Ca intensity map. The brighter the colour, the more is the element concentration. Lower row (left to right): An element association map showing the correlation of Ca and P elements. The centre of green spline in the element association window points to a Ca/P ratio of 2.5. The pixels with the Ca/P ratio of 2.5 are highlighted in green colour in the P and Ca intensity maps.

lesion and a higher number of sections a 4-fold increase in the iron concentration in the lesion was measured [Sic12] (see appendix C).

A significant depletion in zinc content was measured both in the lesion and the artery wall adjacent to it compared to the healthy part of the artery. The Zn/Fe ratio decreases from 5.31 in the control artery to 2.99 in the artery wall with overlying lesion and to 1.18 in the lesion area. A similar trend has been reported in a nuclear microscopy study on apolipoprotein E-deficient mice [Min07]. Zinc is a part of many enzymes that have antioxidant properties [Pow00]. Watt et al. also report that the levels of iron in the lesion went down when the rabbits were treated with zinc supplementation [Wat06]. They concluded that zinc has antiatherogenic effects by reducing the iron level in the lesion. A lower concentration of zinc can imply an impaired antioxidant mechanism. Reiterer et al. have published that zinc deficiency increases plasma lipids and atherosclerotic markers in LDL-receptor deficient mice [Rei01b].

PIXE Stacking

In general, a lesion is spread a few hundreds of micrometers along the artery. The sectional analysis gives just a 2d distribution of the element. To analyse the whole lesion, a collaborative study was undertaken [Sɪᴄ12]. Since the specimen in this study was unsuitable for tomographic experiments, 3d analysis of the lesion was performed by PIXE-stacking. In this, serial sections of the specimen were prepared and measured by conventional nuclear microscopy methods to generate 2d elemental images. These quantitative element maps were then stacked and aligned to reconstruct volumes of element distribution. A total of 49 slices of a murine artery with atherosclerotic lesion were prepared and measured. However, many slices got deformed during the sample preparation. Hence, it was not possible to reconstruct a 3d element volume with all the slices. Figure 8.6 shows stacks of phosphorus and calcium distribution for seven consecutive slices. The composite stack of P and Ca reveals the deposition of calcium on the outer surface of the artery wall. This information would not have been accessible in 2d analysis.
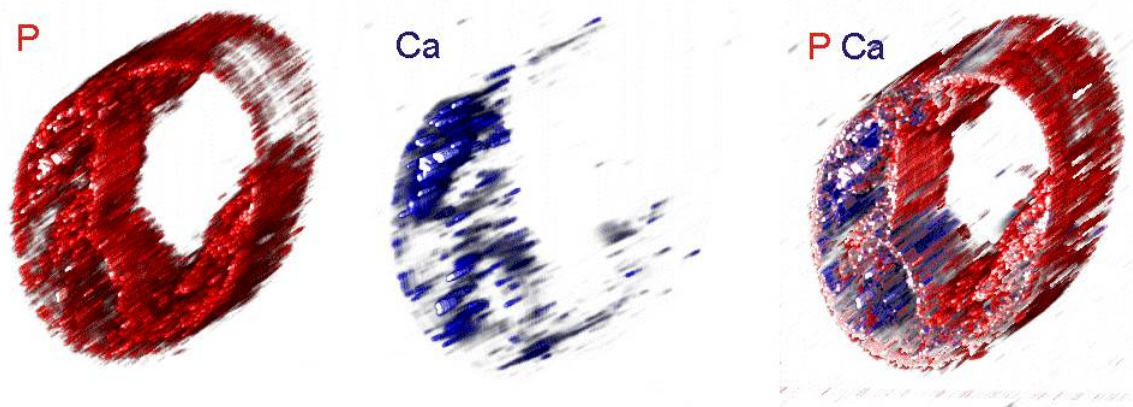
Figure 8.6: Stacks of 2d element distribution maps of P (red) and Ca (blue), and a composite stack of P and Ca. The white regions within the lesion demonstrate a high element concentration.

8.5   Conclusion

In this pilot study on atherosclerosis at LIPSION the applicability of ion beam microscopy in investigating the role of trace elements in atherosclerosis is presented. A mutant mouse model is used to artificially induce atherosclerosis. Ion beam analysis of cross-sections through the brachiocephalic artery reveal the arterial structure and its modification due to the lesion. A differential quantification of the element content in the atherosclerotic lesion reveals elevated S and Ca levels in the artery wall adjacent to the lesion and a slight increase in iron in the lesion. The increase in S concentration in the lesioned artery reflects the presence of extracellular matrix in the growing lesion. A depletion in zinc concentration in the lesion and the adjoining artery wall can be inferred as an impaired antioxidant mechanism, since a zinc-deficient diet can lead to an increase in atherosclerotic markers in mice [Rᴇɪ01ʙ].

This study forms the basis of an extended study, in which the 3D quantitative distribution of elements is reconstructed by means of stacking the 2D quantitative maps of serial sections from BCA [Sic12]. The method of stacking provides an alternative tool for 3D analysis of specimens, which otherwise are unsuitable for tomographic experiments. It can even be a preferred method of analysis, if robust serial sections of the specimen can be prepared, as the quantification of elements is less cumbersome and more accurate than doing PIXE-tomography.

Chapter 9

Elemental Brain Atlas

9.1   Introduction

Brain is the most complex organ in the human body. There are around 86 billion neurons in the human brain [Aze09]. Each neuron communicates synaptically with many neurons in its surrounding. There is a signaling pathway for each function performed by the brain. Given the number of sensory, motor or cognitive tasks that brain does and the numerous possible communication pathways, it is hardly possible to identify the exact signaling cascade for each and every brain function. Despite this complexity the neural circuit is well organised.

The brain can be divided into regions which are associated with specific tasks. A common, simplistic classification is the division of cortex in frontal, parietal, occipital, and temporal lobes. Reference brain atlases have been created with a finer and detailed indexing of brain regions. Depending on the measured property, the brain atlases catalogue anatomical, functional or cellular information. The specificity of immunohistochemical methods has even enabled the visualisation of gene expression. A genome-wide atlas of gene expression throughout the adult mouse brain is available in public domain for open research [Jon09]. A collection of brain atlases of different species can be found at www.brainmaps.org [Jon11].

Apart from brain cartography the reference atlases also serve as control in understanding the pathological changes involved in the neurodegenerative diseases. Many of these diseases can be modeled in laboratory animals like rats and mice, whose brain atlases can be prepared with relative ease. In general, the biochemical state of the brain tissue is investigated with the help of immunohistochemical methods. For example, Nissl stain is used to label the rough endoplasmic reticulum present in the perikaryon of neurons. Figure 9.4a shows a Nissl stained coronal section through a rat brain. This stain shows the distribution of cell bodies in the brain sections. So, any loss of neurons in neurodegenerative diseases can be evidenced by Nissl stain. However, the spatial distribution of trace elements in brain can not be visualised by histochemical methods. A mass-spectrometric approach for such an element atlas has been published by Becker [Bec10]. In this study

a 20 µm thick coronal section of mouse brain was measured by LA-ICP-MS with a spatial resolution of 100 µm in a single scan.

In principle, a fully quantitative element atlas with subcellular spatial resolution can be prepared with the methods of nuclear microscopy. However, the maximum scan size of few square millimetres and relatively long measurement time renders the nuclear microprobe approach to an element atlas time-consuming. A feasibility study was undertaken to differentially determine the distribution of trace elements, particularly iron, in the rat cortex. A thin section through a rat brain is measured piece by piece and the quantitative element maps are subsequently assembled together to create a high-definition element map. Also, glia cells were marked immunohistochemically and were labeled with nickel to analyse the bound trace element content in different types of glia cells in various cortical regions.

9.2 Materials & Methods

An adult Wistar rat (*Rattus norvegicus domestica*) was anaesthetised with CO_2, tran-scardially perfused with saline (0.9% NaCl), followed by a fixative solution of 4% formal-dehyde and 0.1% glutaraldehyde in phosphate-buffered saline (PBS, pH 7.4) for 30 min. The brain was removed immediately, postfixed for 24 h in 4% formaldehyde in PBS, and then mounted in paraffin using conventional protocols. 6 µm thin coronal sections were prepared with a microtome. The sections were deparaffinised and immunohistochemically processed to label astrocytes or microglia. The glial fibrillary acidic protein (GFAP) is used to label the astrocytes and the staining procedure for ionising calcium-binding ad-aptor molecule 1 (Iba1), specifically expressed in macrophages, is followed to label the microglia. The nickel marker helps in differentiating the glial cell bodies, which are around 5 µm in diameter, from the extracellular matrix in the element maps (fig.9.1).
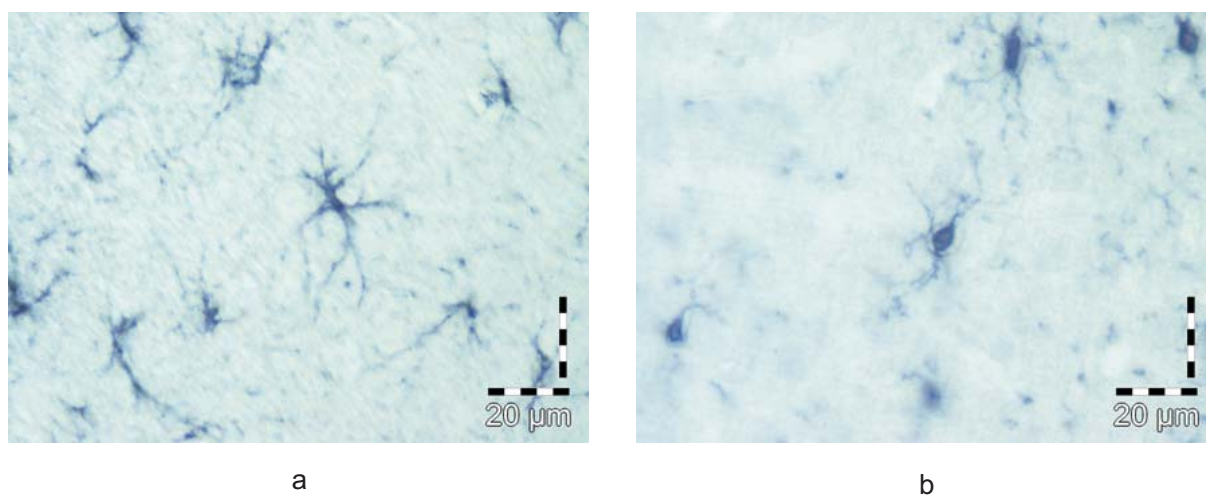

a   b

Figure 9.1: Stained astrocytes (a) and microglia cells (b).

Simultaneous PIXE and RBS measurements were done with a beam spot size of below 1 μm on astrocytes and microglia from the motor-, the somatosensory-, and the association cortex. The nickel map is used to identify the region of interest (ROI) around the glia cells for the quantification of bound elements. To prepare a quantitative element map of the whole coronal section the measurements were done with a beam resolution of 1.2 μm at 1 nA. Since the maximum scan size is 3.2 mm × 3.2 mm, twelve adjacent scans were required to measure the whole cross-section. Each measurement required one hour. The individual element maps were assembled together to create a mosaic element map of the whole section.

9.3   Results & Discussion

Glial specific iron content

The endogenous nickel concentration in a control rat brain was measured to be below the detection limit. Hence, the nickel map of the cells can be used as a proxy for the cellular extent. Figures 9.2 and 9.3 show phosphorus and nickel maps of an astrocyte and a microglia cell, respectively. A distinction can be made in the iron content in these cells based on the brain regions they reside in. An indicative Fe concentration of microglias in the motor cortex is 1.0 mmol/l, in the somato-sensory cortex 2.8 mmol/l and in the association cortex 0.7 mmol/l. Similarly, the iron concentration in astrocytes varies from 0.6 mmol/l in the motor cortex, 0.2 mmol/l in the somato-sensory cortex to 0.3 mmol/l in the association cortex.
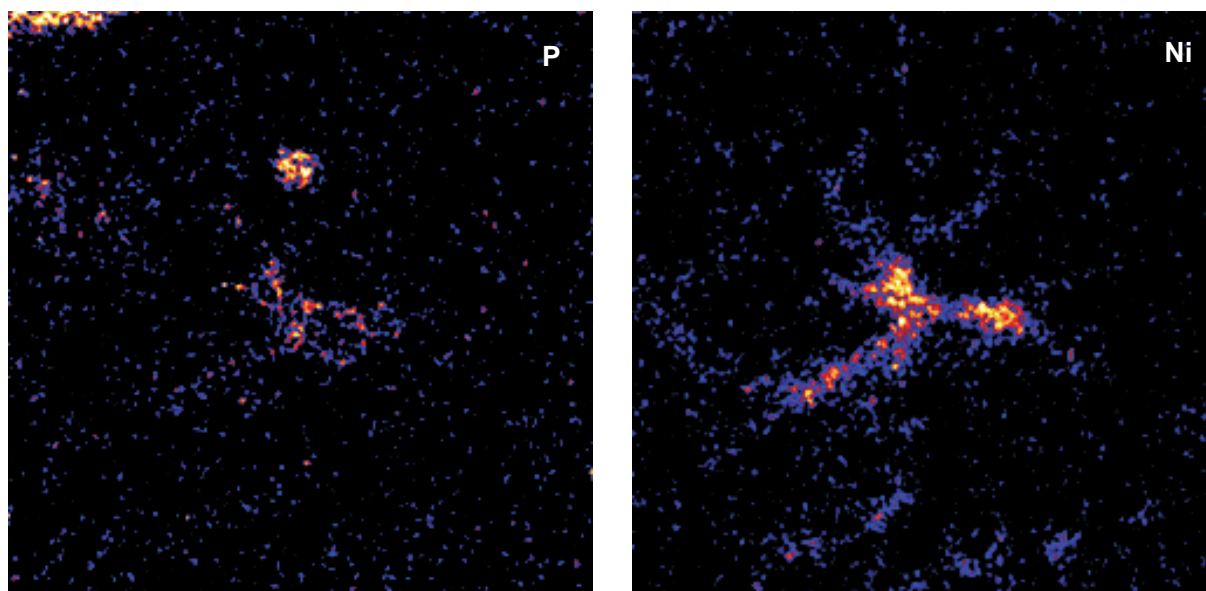

Figure 9.2: phosphorus (left) and nickel (right) maps of a single stained astrocyte. The size of the element maps is 50 μm × 50 μm
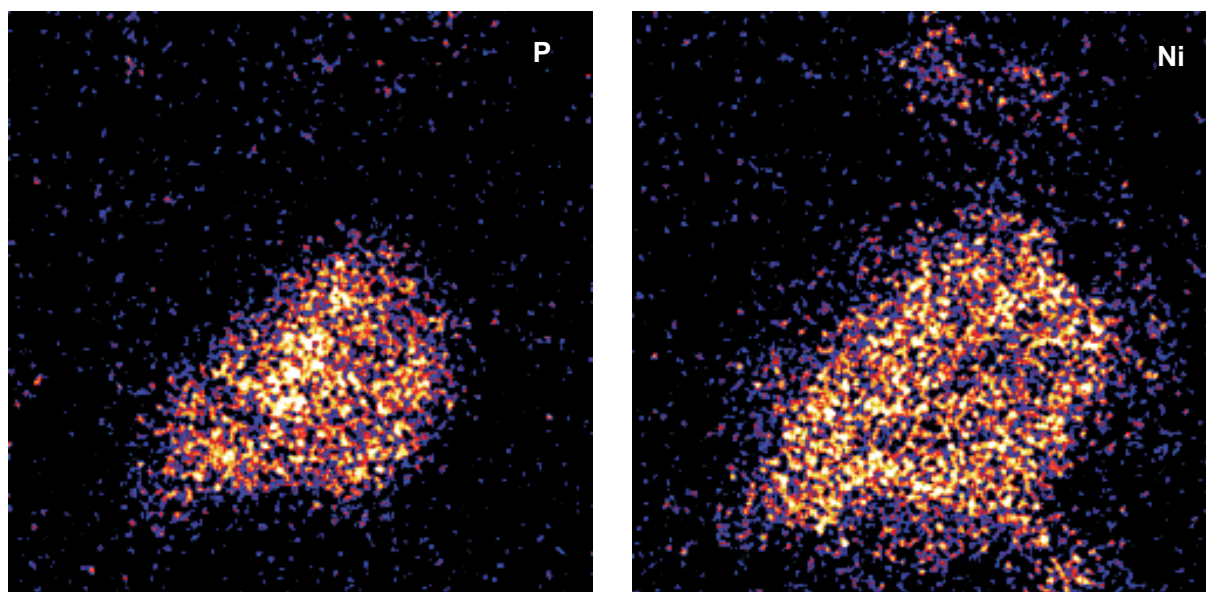
Figure 9.3: phosphorus (left) and nickel (right) maps of a single stained microglia cell. The size of the element maps is $10\,\mu m \times 10\,\mu m$

It has been found in cultured cells that the microglia cells have higher capacity for the accumulation of non-transferrin-bound iron than the astrocytes and the neurons [Bis11]. Free reactive iron is known to induce oxidative stress through Fenton chemistry. Many neurodegenerative diseases have either an unspecific accumulation of iron or a disturbed iron homeostasis and metabolism [Zec02]. So, the mechanisms of transport of iron across the blood-brain barrier into the neuropil are highly topical areas of research. The astrocytes are believed to play a pivotal role in the metabolism of iron in the brain because of their structure and iron binding properties [Dri07].

Large area mapping

Figures 9.4b and 9.5 show mosaics of the phosphorus and sulphur distribution in a rat brain section. The tissue section, taken at the point of maximum dorsal-ventral height and lateral width, is around $13\,mm \times 10\,mm$ in size and required 4×3 scans. The measurement time for the whole coronal section was around fourteen hours. Each scan has 1000×1000 pixels in an area of $3.2\,mm \times 3.2\,mm$. So, the effective spatial resolution of the map is around $3\,\mu m$. More than three orders of magnitude difference in the image size and the spatial resolution make it a high-definition element map. Since the spatial resolution is smaller than most of the cellular bodies, this quantitative map can be used to determine the element content in specific brain regions with subcellular spatial resolution and trace element sensitivity.

Figure 9.4a shows a Nissl stain of a comparable coronal section of rat brain from the literature [Jon07]. Some of the important anatomical regions are marked in the image.

Dark colour represents high density of the cell bodies, whereas areas with no or less dense neurons are light in colour. For example, in hippocampus the pyramidal cell layer is distinctly visible. On the other hand, corpus callosum, which is a bundle of nerve fibers that connects both the hemispheres, appears lighter in colour. In the phosphorus map the corpus callosum is clearly visible because of its high phosphorus content. Elevated levels of phosphorus are due to the axons that are coated with myelin sheaths rich in lipids. Also, in the hippocampus the granular cell layer shows a higher phosphorus content. In general, there is more phosphorus in the subcortical regions than in the cortex. The grey shaded areas in the phosphorus map show the tissue regions lost in the preparation procedure. The distribution of sulphur is relatively uniform in the brain. Sulphur is not only present in the cell bodies, but also is a major constituent of the extracellular matrix [Ioz98]. It can be a good indicator for the perineuronal nets, which are a specialised form the extracellular matrix consisting of large aggregating chondroitin sulphate proteoglycans (CSPG) [Mor09].

Figure 9.6 shows a high-definition map of the distribution of Ni-stained astrocytes in a rat brain section. Since the native concentration of nickel in rat brain is not detectable, the nickel mosaic reflects the distribution of astrocytes that are labeled with nickel.

Table 9.1: Typical MDLs for various elements quantified in an $3.2\,\text{mm} \times 3.2\,\text{mm}$ area of rat brain section. The concentration values are in µmol/l.

Charge	P	S	Cl	K	Ca	Fe	Ni	Cu	Zn
$6\,\mu\text{C}$	160	145	108	72	48	11	20	24	21

Large area mapping can be used to create elemental brain atlases. In this study $130\,\text{mm}^2$ of rat brain has been mapped in $14\,\text{h}$ with a spatial resolution of $3\,\mu\text{m}$ and a current of $1\,\text{nA}$. The minimum detection limit for various elements in an area of $3.2\,\text{mm} \times 3.2\,\text{mm}$ is listed in table 9.1. A rat brain has an average volume of around $600\,\text{mm}^3$ [Sah01]. The section thickness was $6\,\mu\text{m}$, so the analysed volume was $0.78\,\text{mm}^3$. If $30\,\mu\text{m}$ thick sections were taken, which is certainly feasible, the analysed volume would have been $3.9\,\text{mm}^3$ in $14\,\text{h}$. If we consider for a moment that the sensitivity does not changes for thick sections considerably, then the measurement time for whole rat brain would be around $2.15 \times 10^4\,\text{h}$, i.e. 90 days. However, the sensitivity of $11\,\mu\text{mol/l}$ for an area of $10.24\,\text{mm}^2$ is poor for spatially resolved analysis.

The maximum current available at LIPSION for a beam spot of under $3\,\mu\text{m}$ is $17\,\text{nA}$ (tab.5.1). If the measurements are performed at $17\,\text{nA}$ and the measurement time is 90 days the sensitivity improves by a factor of $\sqrt{17}$. Or, if a sensitivity of $11\,\mu\text{mol/l}$ is to be achieved for a smaller area of, for example, $50\,\mu\text{m} \times 50\,\mu\text{m}$, a factor of 10^7 more charge would be required. This is not practical. On the other hand, the volume of subthalamic nucleus (STN) in rats is around $0.8\,\text{mm}^3$ [Har02] and its area in coronal sections should be less than $1\,\text{mm}^2$. For a factor of 100 more in charge a sensitivity of $11\,\mu\text{mol/l}$ can be achieved in this brain region.
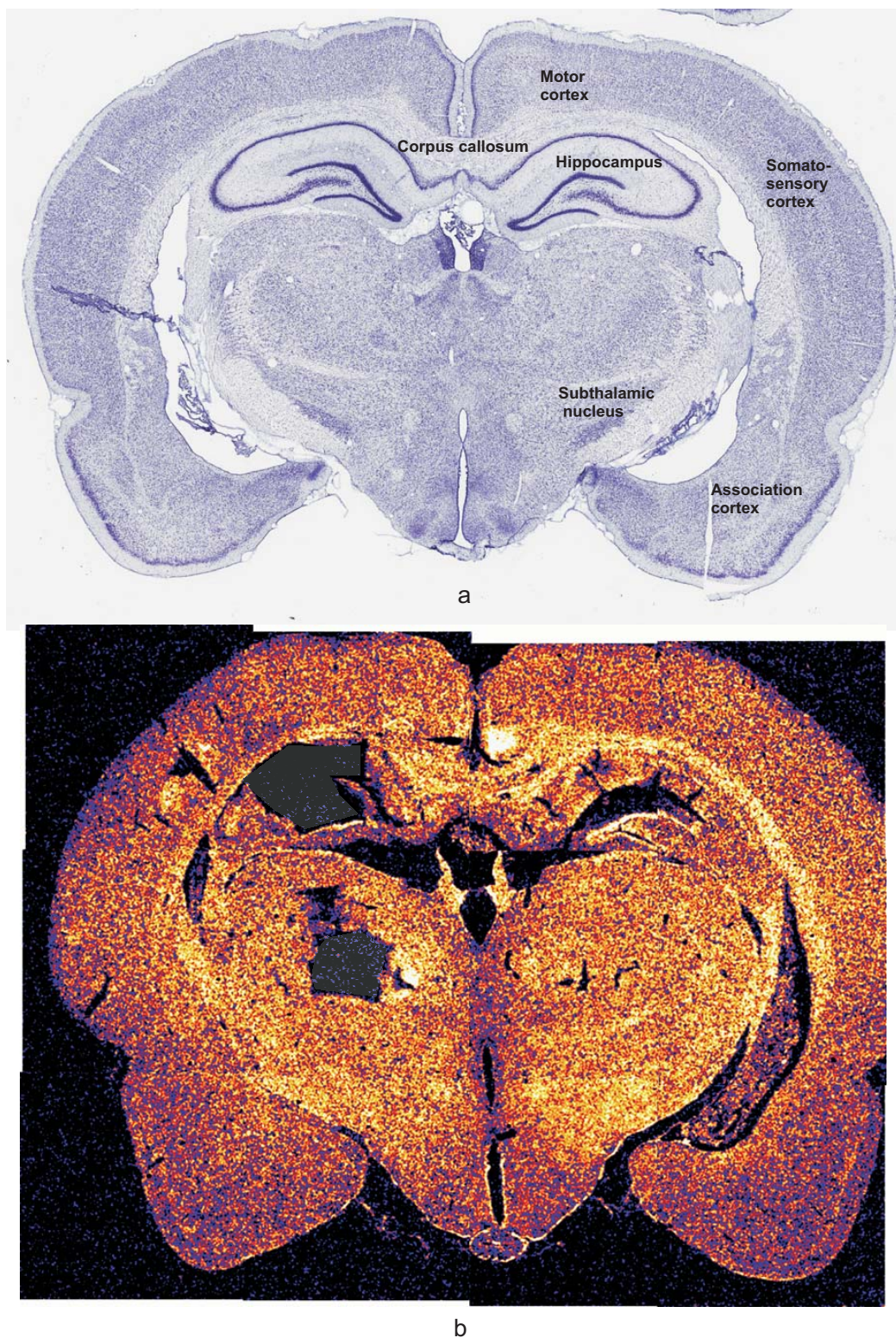
Figure 9.4: (a) Nissl stain showing the distribution of cell bodies in a coronal cross-section of rat brain [Jon07]. (b) phosphorus high-definition map of a 6 µm coronal section of a rat brain (Bregma −4.3 mm). The grey shaded area represents the missing brain tissue.
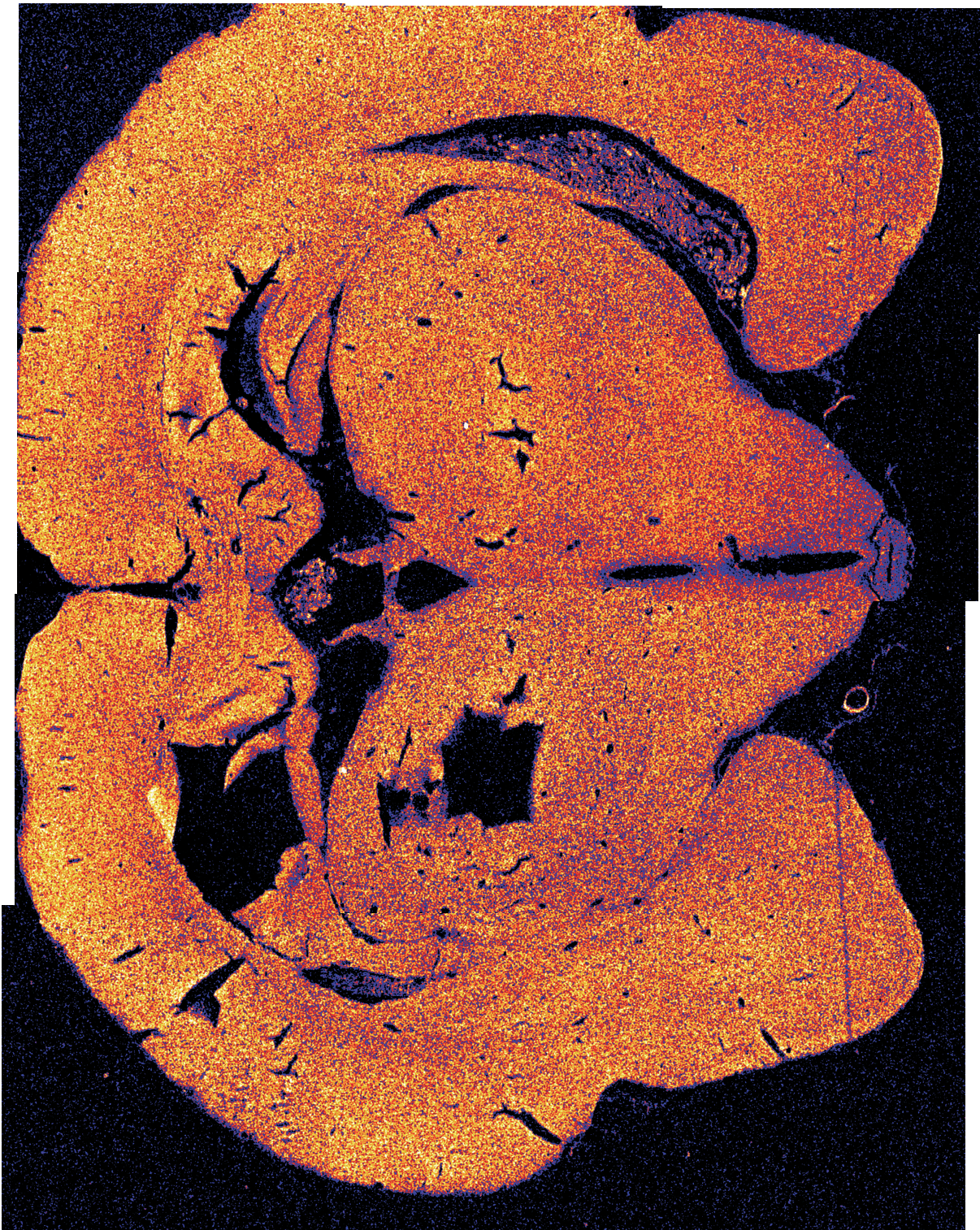
Figure 9.5: Sulphur high-definition map of a 6 μm coronal section of a rat brain (Bregma −4.3 mm).
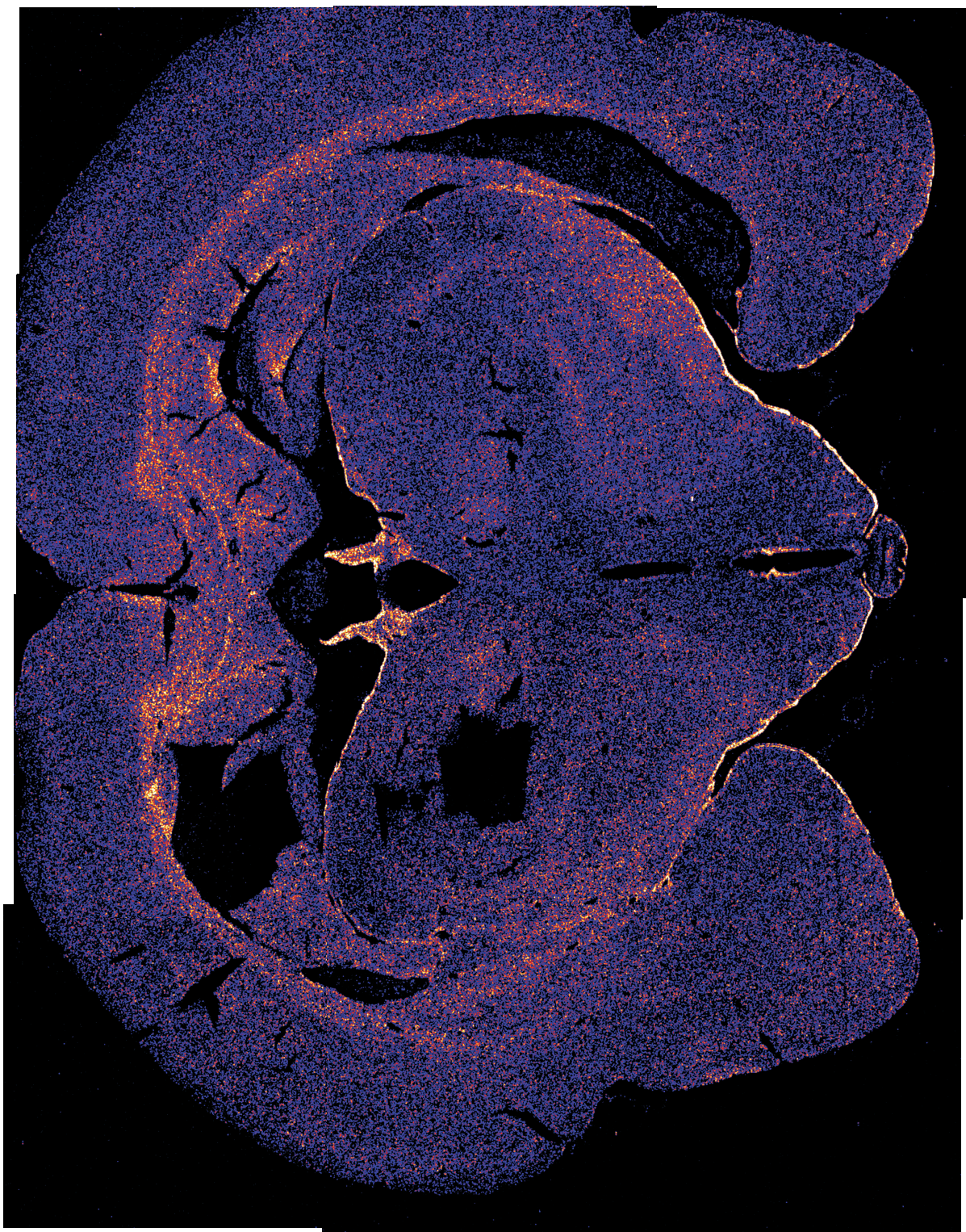
Figure 9.6: Ni high-definition map of a 6 µm coronal section of a rat brain. The distribution of astrocytes is visualised with the help of Ni stain (Bregma −4.3 mm).

So, an elemental rodent brain atlas with a sensitivity of $11\,\mu mol/l$ per mm^2 can be realised in 530 days if the beam current is $17\,nA$. The use of multiple detectors or a large array detector [Rya10] can further reduce the measurement time. However, it is important to note that the concentration of some trace elements like Mn is only about $1\,\mu g/g$. Because of its relevance in Parkinsonism, there is a growing interest in understanding its transport in the brain [Asc07]. To be able to quantify $1\,\mu g/g$ the MDL for Mn should be $0.3\,\mu g/g$. Even with a beam current of $17\,nA$ this sesitivity is only possible for areas larger than $1\,mm^2$. When measuring with such high currents, the dead time of the data acquisition system is above 50%. It can be reduced by shortening the pulse shaping time. In order to minimise the sample damage due to heat, the sample should be cooled. A variety of ways of achieving this are explained in [Lla96].

Subthalamic nucleus

Large area high-definition element mapping was also applied to complement a study in cognitive science. To study the parcellation of iron in human subthalamic nucleus (STN), a section of STN was measured by nuclear microscopy. Figure 9.7 shows a high-definition quantitative map of iron distribution in a section of STN. This map serves as a reference for quantifying the signal that emanates from iron during *in vivo* measurements on STN by functional magnetic resonance imaging [Keu].
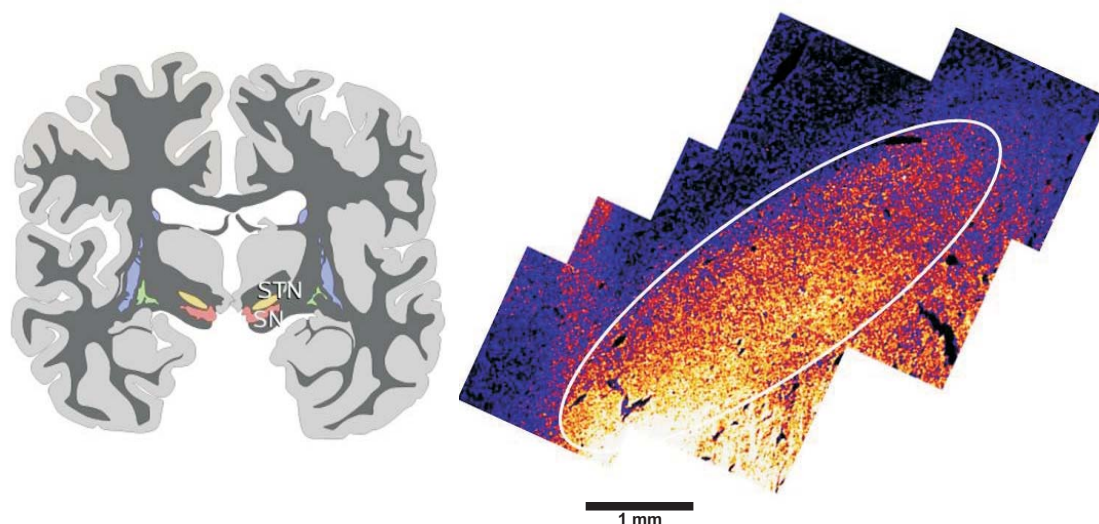

Figure 9.7: On the left is an illustration of a coronal section through human brain showing the location of the substantia nigra (SN) and the subthalamic nucleus [Gil05]. On the right is a large area map of iron distribution in human STN.

9.4   Conclusion

Measurements with high beam current allow generation of quantitative elemental maps of macro-dimensional specimens in a reasonable amount of time. A coronal section of rat brain measuring $13\,\text{mm} \times 10\,\text{mm}$ was measured in fourteen hours. The quantitative mosaics of element distribution are of high-definition with 12 Mega-Pixel at $3\,\text{µm}$ spatial resolution. The measurement time of fourteen hours per section makes the construction of a quantitative element atlas of the rodent brain feasible. Particular anatomical areas of the brain are also reflected in the element maps. Such an atlas can be used as reference for studying the pathological changes in neurodegenerative diseases that implicate the trace element imbalance. Also, the quantitative maps of large specimens can serve as reference for the quantitative interpretation of data from *in vivo* methods like magnetic resonance imaging.

The immunohistochemical staining with nickel marker can help in visualising the distribution of cell bodies. Also, the nickel marker is useful in determining the extent of small cells that are difficult to differentiate from the surroundings in the element maps like the astrocytes. The quantification of iron bound to astrocytes and microglia in three different cortical regions shows that a study of functional correlation based on the amount of iron bound to the glia cells and their location in the cortex is possible. The neurodegenerative diseases that implicate iron overload can also be caused due to a malfunction in the scavenging or the iron-delivery mechanisms of the glial cells. This hypothesis can be investigated by a combination of immunohistochemical and nuclear microscopy methods. Burdo et al. mapped the cellular distribution of iron in the brain of Belgrade rats that have a mutation in Divalent Metal Transporter 1 [Bur99]. They used Perls' stain to visualise the iron distribution. In Perls' stain not all forms of iron can be labled. Here, Large Area Mapping in conjugation with immunohistochemical methods can provide subcellular distribution of total iron.

Chapter 10

Outlook

Nuclear microscopy occupies a unique position among the chemical analysis techniques. The fully quantitative nature of this method, combined with a very high detection sensitivity and a sub-micron spatial resolution, enables the mapping of elements with trace element sensitivity. Since the method is non-destructive, many applications in biomedical research are possible. From neurobiology to cognitive brain sciences, the spectrum of applications is very broad.
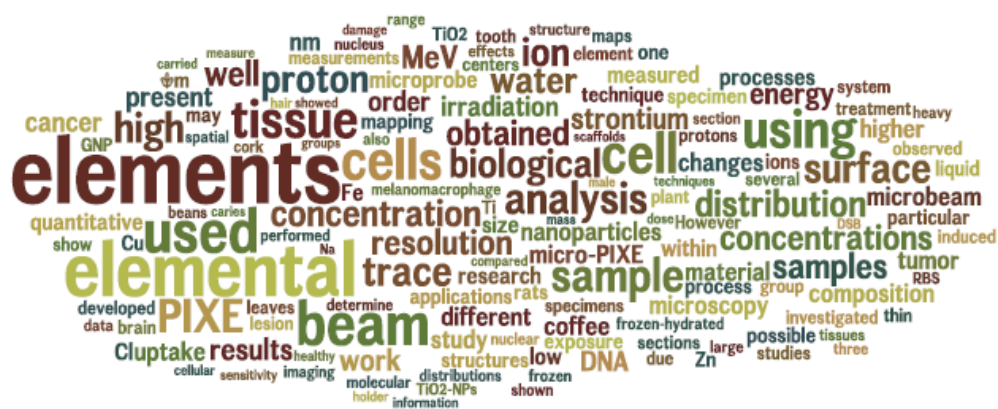

Figure 10.1: A word cloud of the abstracts presented at the 13th International Conference on Nuclear Microprobe Technology and Applications in Lisbon under the category 'Biology and Biomedicine'.

However, nuclear microscopy is still considered an experimental technique. Figure 10.1 shows a word cloud generated from the abstracts of contributions made to the 13th International Conference on Nuclear Microprobe Technology and Applications in Lisbon under the category 'Biology and Biomedicine'. The prominence of the words like 'elements', 'concentration', 'distribution' etc. underlines the experimental nature of nuclear microscopy, whereas the biomedical keywords like 'cancer', 'brain', 'lesion' etc., that would

suggest an established method of analysis, appear less frequent. The present study builds on the previous work to effect the transition of this method from experimental towards a routine method of analysis in biomedical research.

A large number of samples needs to be processed for a statistically robust proposition in biomedical experiments. The number of samples must be chosen in such a way that the probability of the measured value falling within the inherent biological variability, which is assumed to be 20%, is rendered insignificant. The requirement of a high sample throughput is achieved at LIPSION, as the beam current density is high ($>1\,\mathrm{nA}/\mu^2\mathrm{m}$). The novel method of charge measurement in the aperture box is independent of the influence from secondary electrons from the sample, and therefore, is more reliable.

Over the years the trace element microanalysis has been the mainstay of biomedical research by nuclear microscopy. A high sample throughput and an efficient experiment design can help in providing biologically relevant data for understanding the pathophysiology of diseases in which the trace elements might play a role. A statistically significant number of cases has been analysed to investigate the trace element hypothesis in Parkinson's disease. Similarly, the Alzheimer's disease can be studied. The concurrent use of immunohistochemical markers enhanced with single metals like Ni can even identify the structures that are implicated in the disease progression. The lead provided by Morawski et al. in a feasibility study on identifying the neurofibrillary tangles and analysing them by nuclear microscopy is worth pursuing [Mor05].

Not only the trace elements but also the electrolyte elements were quantified successfully in the drosophila head by preparing the specimens in an ion conservative way. New grounds have been broken in 3d analysis by PIXE-stacking, and in the analysis of macro-dimensional samples by high-definition PIXE. Given the extensive use of fruit flies in genetics and as animal models for a variety of diseases, the preparation of reference elemental atlases can only benefit from the current research. A 3d elemental atlas of the drosophila head can be generated by PIXE-stacking in a relatively a short period of time. The preparation of elemental atlases of rodent brains, on the other hand, requires extensive beam time. A combination of Large Area Mapping and PIXE-stacking is needed to generate such a quantitative atlas. An automated algorithm that moves the sample stage after each measurement is performed with a predetermined amount of charge can help in reducing the beam time for macro dimensional samples. The measurement time can be further reduced by increasing the detection angle either through the use of multiple detectors or a single large array detector. The Maia 384 detector array is developed by Ryan et al. for high throughput and high definition PIXE elemental imaging [Rya10]. Its real-time deconvolution of the spectra can even save some time in the post-processing of data. Again, the tagging of antibodies with elemental markers will enable the visualisation of the distribution of various types of cells. Based on the bound element content a correlation can then be drawn between the cell type, the area of residence in brain, and the function it performs. An intelligent sample preparation, in which multiple immunohistochemical markers enhanced with different single elements and non-overlapping peaks are used to tag different type of cells, can yield a multilayered atlas in a single measurement.

Nuclear microscopy also has the ability to serve as a reference method for the *in vivo* methods like Magnetic Resonance Imaging (MRI). The MRI is crucial not only in brain research but also in clinics for diagnostic purposes, as it can provide anatomical as well as functional information. The tissue iron concentration can be estimated by quantitative susceptibility mapping in high-field MRI [Bɪʟ12]. However, the MR signal from iron is, at best, semi-quanititative. Many cognitive diseases have abnormal distributions of iron in the brain. If the MR signal from iron is pre-validated by nuclear microscopy, then the cognitive deficiencies can be researched and diagnosed quantitatively. An eventual clinical therapy can be monitored as well. For nuclear microscopy to grow and sustain in biomedical research, a link to the pre-clinical or clinical stage has to be established.

Appendix A
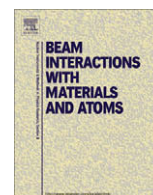
Trace element mapping in Parkinsonian brain by quantitative ion beam microscopy

Nirav Barapatre [a,*], Markus Morawski [b], Tilman Butz [a], Tilo Reinert [a]

[a] *Nukleare Festkörperphysik, Universität Leipzig, Linnéstr. 5, 04103 Leipzig, Germany*
[b] *Paul-Flechsig-Institut für Hirnforschung, Universität Leipzig, Jahnalle 59, 04109 Leipzig, Germany*

ARTICLE INFO

ABSTRACT

The role of iron in the pathogenesis of the Parkinson's disease (PD) is a current subject of research in Neurochemistry, since an abnormal increase in iron is reported in the *substantia nigra* (SN) of Parkinsonian patients. A severe loss of the cells containing dopamine in the SN in the PD has also drawn attention towards the function of a browny-black pigment called neuromelanin, which accumulates predominantly in these dopaminergic neurons. The neuromelanin has an ability to chelate metal ions, which, in free state, may cause considerable damage to cells by reacting with their lipid-rich membranes. However, it could also potentiate free radical production if it releases the bound metal ions. The highly sensitive and non-destructive micro-PIXE method suits best to quantify and map the trace elements in the SN.

The accuracy in charge measurement for such microanalysis studies is of utmost importance for quantitative analysis. Since a Faraday cup is usually placed behind the thin biological sample to measure the charge, the primary and the secondary electrons, knocked out from the sample by traversing ion beam, hamper an exact charge determination. Hence, a new non-interceptive technique was developed for precise charge measurement and for continuous monitoring of beam current.

1. Introduction

The Parkinson's disease (PD) is the second most common neurodegenerative disease after Alzheimer's disease [1]. The aetiology of the PD is largely unknown. Sir James Parkinson described the illness first in the book "An essay of shaking palsy". The symptoms generally noticed in PD are resting tremor, bradykinesia and muscle rigidity. At the cellular level, severe loss of dopaminergic nerve cells in the *pars compacta* of *substantia nigra* (SN) in the midbrain region is linked with the PD [2]. Of various possibilities that may lead to the pathogenesis of PD, oxidative stress has been most discussed since a correlation between increased iron level in SN and PD has been reported [3]. Iron is the most abundant transition metal in the human body and has many essential functions in brain. It is not only involved in protein and DNA synthesis, but also plays an important part in the formation of myelin and the development of dendrites [4]. Further, iron is a cofactor for the generation of neurotransmitter dopamine. The specific death of dopaminergic neurons has also drawn attention towards a melanin like pigment, neuromelanin (NM), present in these cells. NM has an ability to bind metal ions, which in free state could have toxic effect on the cells. Hence, a protective role of NM is proposed, which in PD is perhaps compromised leading to death of dopaminergic cells in SN [5,6]. Micro-PIXE is a versatile tool for determining the concentration and distribution of trace elements [7–9]. Previous PIXE studies have shown a co-localisation of metal ions and NM, which underlines the binding capability of NM [9,10].

2. Sample preparation

The human midbrain regions encompassing the *substantia nigra* of six idiopathic Parkinson's disease patients and six non-demented controls were obtained from the Brain Bank of the University of Leipzig. The PD subjects were aged 75 ± 5 years and the controls were between 64 and 72 years old. The brain samples were fixed by immersion in 4% formalin (4% aqueous solution of HCHO) for 1 week or longer. The conventional protocols for paraffin embedding and block mounting were followed. The tissue was cut into 6 µm thick sections. The sections were deparaffinised with xylene and rinsed with ethanol to bring it into toluene. The slices were embedded in mounting medium (DePeX®, Merck). The embedded sections were peeled off and brought on a sample holder for microbeam analysis.

3. Charge measurement

The microanalysis studies require an exact determination of the amount of charge applied on the sample. In our setup the charge is

* Corresponding author. Address: Fakultät für Physik und Geowissenschaften, Universität Leipzig, Linnéstr. 5, D-04103 Leipzig, Germany. Tel.: +49 341 97 32711; fax: +49 341 97 32708.
 E-mail address: barapatre@physik.uni-leipzig.de (N. Barapatre).
 URL: http://www.uni-leipzig.de/~nfp (N. Barapatre).

measured by a Faraday cup placed behind the sample, since the biological samples are transparent for the energetic ion beam. Therefore, the amount of charge, which is collected in the Faraday cup is not only given by the ion beam, but also by the secondary electrons knocked out from the sample by the traversing ion beam. Another, less accurate option would be to measure the beam current directly in the Faraday cup without the sample. If the beam conditions are sufficiently stable, the current can be used to calculate the applied charge from the duration of the measurement. This option is, however, often not reliable because many experiments require precise knowledge of the applied charge. This inaccuracy can be compensated either by periodic measurement of the backscattering yield from a beam chopper [11] or by blanking the ion beam periodically in a Faraday cup [12]. There might be many other innovative ways of measuring charge.

We have developed a non-interceptive, non-blanking way of measuring charge. Assuming a distinguished beam density distribution due to flux peaking [13], the ion beam current can be monitored shortly before the aperture diaphragm by using a set of copper plates (pre-aperture, Fig. 1). A front plate (the pupil plate) collimates the ion beam through a 2 mm hole followed by a rear plate (the collector plate). This collector plate, having a 1 mm hole, allows beam current monitoring, without obstructing the aperture diaphragm illumination. Hence, the ratio Q_{Col}/Q_{FC} of the current at the collector plate to the current at the sample position without sample (measured in a Faraday cup right next to the sample position) should remain constant. Once this ratio is determined, the amount of the charge applied to the sample can be calculated from the charge measured at the collector plate. The prerequisite for such a calculation is a constant brightness of the beam for a given object/aperture setting, which can be considered to be fulfilled for the Leipzig system. Test measurements showed that this ratio was constant over the whole day. For 100 μm/300 μm object/aperture setting Q_{Col}/Q_{FC} was determined at an interval of 30 min for a period of 7 h. The mean ratio was 15.24 ± 0.18. Since the ratio as well as the brightness depends on the selected object diaphragm [14], the ratio must be determined for each object/aperture settings or if the accelerator settings are changed (Fig. 2).

Due to the technical implementation of the 'pre-aperture' plates, the ratio is always above 10. This facilitates fluence determination for low beam current (<1 pA) applications (e.g. proton beam writing) where conventional charge/current measurements are no longer appropriate [15,16]. The minimum measurable fluence can be decreased by the ratio Q_{Col}/Q_{FC}.

4. Experimental

The unstained sections were analysed at the ion beam laboratory LIPSION [17] (University of Leipzig). A 2.25 MeV proton beam of 250 pA was focussed to 0.5 μm. The NM was measured typically with a scan size of 50 μm × 50 μm. The integrated charge for a scan was around 0.55 μC (0.22 nC/μm²). The extracellular regions were measured with a scan size of 100 μm × 100 μm. Within this scanning area the elemental distributions were homogenous because no structure appeared in the PIXE maps. The minimum detection limit for iron was 50 μmol/l. The integrated charge on the sample was approximately 0.3 nC/μm². Particle induced X-ray emission (PIXE) was used to analyse the minor elements' (P, S) and trace elements' (Fe, Cu, Zn) distributions. Backscattering spectrometry (BS) was used simultaneously to gain information on the thickness and the matrix elemental content (C, N, O) of the sample. The BS data were analysed by RUMP code [18]. The total accumulated charge on the sample was also determined by fitting the BS spectrum with the same program code. This information from BS spectrometry served as the input parameters for quantitative analysis of the PIXE data with GeoPIXE [19].
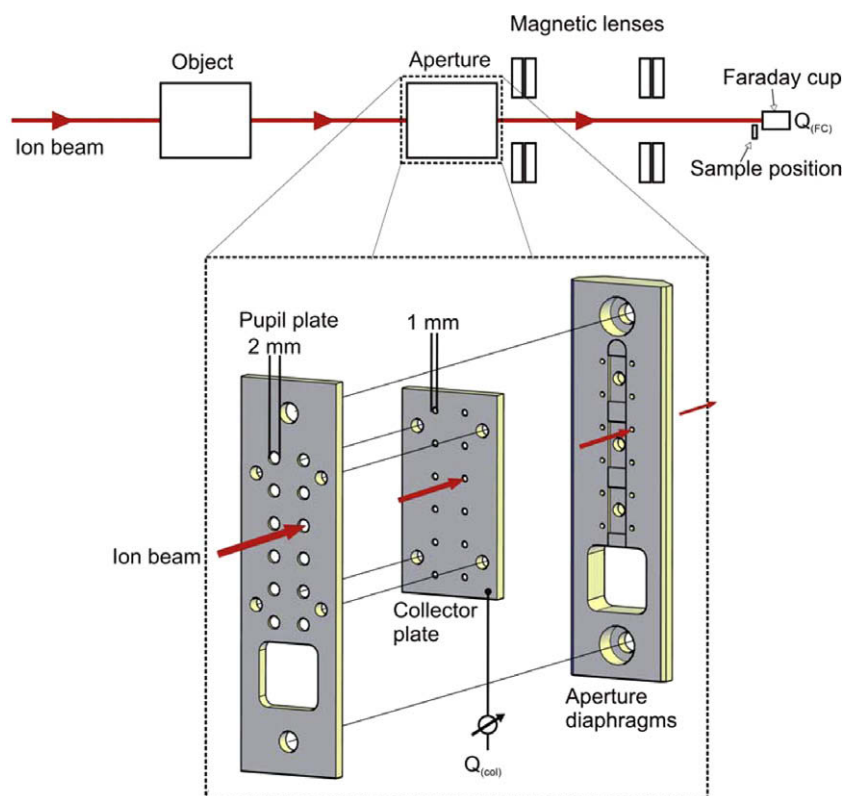

Fig. 1. A schematic representation of the 'pre-aperture' and the trajectory of the beam after leaving the object diaphragm. The ratio of current at collector plate to the current in Faraday cup (without sample) remains constant, unless beam brightness or accelerator settings are changed.
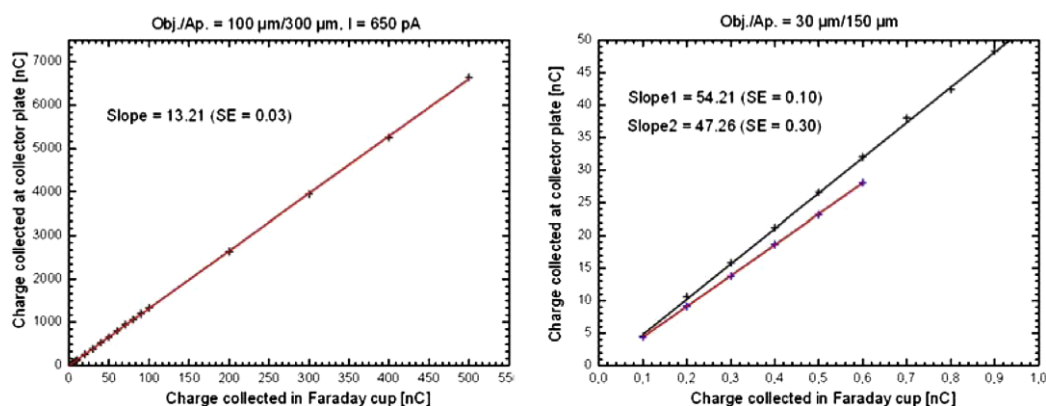
Fig. 2. Simultaneous charge measurement at the collector plate before the aperture diaphragm and in a Faraday cup at the sample position (the crosses represent ±1% error bar). The linear fit indicates the constant nature of the ratio Q_{Col}/Q_{FC}. The slope is obviously different for different object settings, since the beam brightness is not homogenous [18]. The right graph also shows the effect of changes in accelerator settings (extraction voltage) on the ratio of the currents.
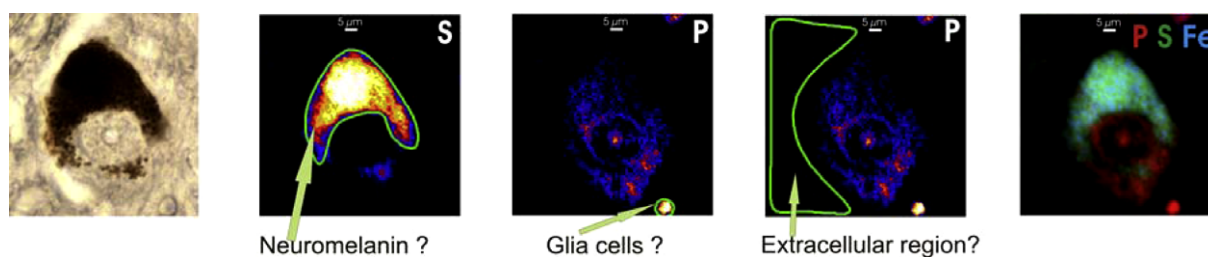

Fig. 3. (From l to r) An optical picture of a dopaminergic cell pigmented with neuromelanin. Sulphur map highlighting the neuromelanin. Phosphorous map shows cell nucleus and phosphorous rich gila cell of 5 μm diameter. The extracellular region is chosen in such a way that it does not include any visible definite structures. A three-element map revealing the co-localisation of neuromelanin and Fe.

Sulphur is present in the building blocks of neuromelanin (Fig. 3) [6]. Hence, it was used as melanin indicator. At least 10 pigmented cells and five extracellular regions were analysed in each of the three idiopathic Parkinsonian and three control cases. The PIXE maps of the extracellular region revealed many phosphorous rich structures of approximately 5 μm diameter. These structures were interpreted as glia cells as the morphology and phosphorous content was similar to a previous study [20]. The elemental content contribution from these cells was excluded from the analysis of the extracellular region. The elemental content of the glia cells is currently under investigation.

5. Results and discussion

The degree of NM pigmentation varies from cell to cell. To be able to compare the trace element content in numerous cells, the trace element content was normalised to the NM indicator, sulphur. The results are shown in Table 1. For both, Parkinsonian and control cases, the iron content bound to NM is at the same

level. However, there was a significant decrease in calcium and increase in potassium content for the Parkinsonian cases. The calcium content was about 40% lower, whereas the potassium content was around five times higher in the PD affected cases. No significant change in the content of other trace elements (Cu, Zn) was observed. The elemental content in the extracellular region showed a similar trend. The iron content was not significantly altered, whereas in the PD cases the calcium level was 30% lower than the controls and the potassium level was almost 4-fold the control level. The trace elements copper and zinc were unaltered.

Various studies on the total iron in the SN in PD brains have either reported insignificant or significant changes [3]. So, it is not yet an established fact that Fe imbalance is indeed manifested in the SN of Parkinsonian patients. We need to analyse even more cases to gather enough statistics to support or refute the Fe imbalance hypothesis.

6. Conclusion

The micro-PIXE setup of the University of Leipzig has developed a suitable quantitative trace element analysis method for biological samples. It provides for high resolution quantitative imaging [10] as well as exhaustive statistical studies. The new charge measuring system promises not only precise charge measurement for the PIXE studies but also very low fluences for the proton beam writing.

The trace elemental distributions in Parkinsonian brain was analysed differentially for three cases and compared with three controls. The iron content in *substantia nigra* of Parkinsonian cases was not significantly different. This study included more cases and data than the previous ones [9,21]. The varying results of these studies suggest there is a high variance in the trace element distribution within the cases of same category. This variance is

Table 1
Comparison of the elemental content in neuromelanin and in the extracellular region for three controls and three Parkinsonian cases. Data are mean values ± SEM.

	Element	Control (10^{-3})	Parkinson' disease (10^{-3})
Neuromelanin	K/S*	9 ± 1	50 ± 5
	Ca/S*	67 ± 5	42 ± 5
	Fe/S	104 ± 4	98 ± 6
		(mmol/l)	(mmol/l)
Extracellular region	K*	1.24 ± 0.15	4.79 ± 0.69
	Ca*	4.08 ± 0.38	2.79 ± 0.52
	Fe	11.00 ± 2.10	7.70 ± 1.40

* Significance $p < 0.05$ (students t-test).

perhaps due to different stages of the disease and varying ages of the subjects.

Acknowledgement

References

[1] R. Mayeux, Annu. Rev. Neurosci. 26 (2003) 81–104.
[2] L.S. Forno, J. Neuropathol. Exp. Neurol. 55 (1996) 259–272.
[3] M.E. Götz, K.L. Double, M. Gerlach, M.B.H. Youdim, P. Riederer, Ann. NY Acad. Sci. 1012 (2008) 193–208.
[4] D. Ben-Shachar, P. Riederer, M.B. Youdim, J. Neurochem. 57 (1991) 1069–1614.
[5] H. Fedorow, F. Tribl, G. Halliday, M. Gerlach, P. Riederer, K.L. Double, Prog. Neurobiol. 75 (2005) 109.
[6] L. Zecca, D. Tampellini, A. Gatti, R. Krippa, M. Eisner, D. Sulzer, S. Ito, R. Fariello, M. Gallorini, J. Neural Transmission 109 (2002) 663–672.
[7] K.G. Malmqvist, Nucl. Instr. and Meth. B 49 (1990) 183.
[8] M.B.H. Breese, G.W. Grime, F. Watt, Annu. Rev. Nucl. Part Sci. 42 (1992) 1.
[9] M. Morawski, Ch. Meinecke, T. Reinert, A.C. Dörffel, P. Riederer, T. Arendt, T. Butz, Nucl. Instr. and Meth. B 231 (2005) 224.
[10] T. Reinert, D. Spemann, M. Morawski, T. Arendt, Nucl. Instr. and Meth. B 249 (2006) 734.
[11] L. Bartha, I. Uzonyi, Nucl. Instr. and Meth. B 161–163 (2000) 339.
[12] V. Auzelyte, F. Andersson, M. Elfman, P. Kristiansson, J. Pallon, M. Wegdén, C. Nilsson, N. Arteaga Marrero, Nucl. Instr. and Meth. B 249 (2006) 760.
[13] R. Szymanski, D.N. Jamieson, Nucl. Instr. and Meth. B 130 (1997) 80.
[14] D.J.W. Mous, R.G. Haitsma, T. Butz, R.-H. Flagmeyer, D. Lehmann, J. Vogt, Nucl. Instr. and Meth. B 130 (1997) 31.
[15] F. Menzel, D. Spemann, S. Petriconi, J. Lenzner, T. Butz, Nucl. Instr. and Meth. B 260 (2007) 419.
[16] A.A. Bettiol, I. Rajta, E.J. Teo, J.A. van Kan, F. Watt, Nucl. Instr. and Meth. B 190 (1–4) (2002) 154.
[17] T. Butz, R.-H. Flagmeyer, J. Heitmann, D.N. Jamieson, G.J.F. Legge, D. Lehmann, U. Reibetanz, T. Reinert, A. Saint, D. Spemann, R. Szymanski, W. Tröger, J. Vogt, J. Zhu, Nucl. Instr. and Meth. B 161–163 (2000) 323.
[18] L.R. Doolittle, Nucl. Instr. and Meth. B 9 (1985) 344.
[19] C.G. Ryan, Nucl. Instr. and Meth. B 181 (2001) 170.
[20] M. Morawski, T. Reinert, Ch. Meinecke, T. Arendt, T. Butz, Nucl. Instr. and Meth. B 231 (2005) 229.
[21] T. Reinert, A. Fiedler, M. Morawski, T. Arendt, Nucl. Instr. and Meth. B 260 (2007) 227.

Appendix B

µPIXE for a µBrain: The vinegar fly's brain, antenna, sensilla hairs and eye ion concentrations

Anja Reinert [a,*], Nirav Barapatre [b], Silke Sachse [a], Tilo Reinert [c]

[a] Department of Evolutionary Neuroethology, Max Planck Institute for Chemical Ecology, Hans-Knöll-Strasse 8, 07745 Jena, Germany
[b] Institute for Experimental Physics II, University of Leipzig, Linnéstrasse 5, 04103 Leipzig, Germany
[c] Department of Physics, University of North Texas, 1155 Union Circle, 76203 Denton, TX, United States

ARTICLE INFO

ABSTRACT

The vinegar fly Drosophila melanogaster is used as model organism to study a variety of different scientific purposes. Thus, our laboratory studies the olfactory system by neurobiological experiments. These techniques are often disruptive and need to compensate or exchange the body fluid, the lymph, with an artificial Ringer's solution in defined compartments of the fly. The solution mainly contains Na, Cl, K and Ca and is to keep physiological conditions. Therefore, the knowledge about the ion concentrations in the respective Drosophila lymph is required for a correct mixture of the ions.

This paper presents the spatially resolved concentrations of P, S, Cl, K, Ca, Fe, Cu and Zn in lyophilised head cryosections of Drosophila by using quantitative µPIXE at the ion beam facility LIPSION in Leipzig. The PIXE maps enable a detailed analysis of particular regions of interest down to a spatial resolution of 0.5 µm.

We quantified the ion concentrations especially in the brain, the antenna and its sensilla hairs acting as the olfactory organ of the fly, in the compound eye and in the mouthparts. The averaged element concentrations of these main compartments are (in descending order): P: 90 mM, K: 81 mM, S: 38 mM, Cl: 18 mM, Ca: 4.9 mM, Fe: 1.4 mM, Zn: 1.2 mM, Cu: 0.06 mM. Certain structures or cavities possess a remarkably high concentration of particular elements and might reflect the different functions of the compartments. An example presented in more detail is the composition of the compound eye. Conclusively, our findings on the ion concentrations might be useful for the mixture of the Drosophila Ringer's solution to ensure physiological conditions in experiments.

1. Introduction

The vinegar fly Drosophila melanogaster is one of the most famous model organisms in biology. It's sequenced genome, fast replication cycle and easy handling makes Drosophila a brilliant genetic model and tool to study a variety of different scientific purposes.

Neurobiological experiments require the knowledge of the ion concentration in the Drosophila's body fluid, the lymph. Especially when electrophysiological techniques or optical recording experiments disrupt the tissue or the cellular barrier the application of artificial lymph is needed to remain physiological conditions. The most commonly used compensatory solution is the so-called Ringer's solution that mainly contains the ions Na, Cl, K and Ca. Several recipes for Ringer's solution are available depending on the investigated specie, the different cavities (for example discrim-

inating between hemolymph and sensilla-/receptor-lymph) or the applied technique that might require a modification of the solution.

However, the recipes for insect lymph solutions are mainly based on the ion concentrations estimated by indirect non-quantitative techniques (see for example [1–4]). Quantitative data on the concentration of ions were achieved by electron-probe X-ray microanalysis (EPXMA) on several compartments of the antenna of the silkmoth Bombyx mori [5] and the labellar taste hairs of the blowfly Protophormia terraenovae [6], respectively. Schofield et al. [7] used particle-induced X-ray emission (PIXE) to quantitatively study the accumulation of Fe, Cu and Zn in whole Drosophila melanogaster flies and in Drosophila hydei larvae, respectively, and in dissected Malpighian tubules and gut. However, the element content in this study is given as mass ratio (parts per million of dry mass) and not as a concentration value (mass per litre), the spatial resolution is in the order of several micrometres and information on the electrolytes is not provided.

Our laboratory studies the olfactory and neurobiological system of Drosophila melanogaster. Thus, the aim was to quantify the ion concentrations especially in the brain, the antenna and its sensilla

* Corresponding author. Tel.: +49 0 3641 57 1452; fax: +49 0 3641 57 1402.
E-mail address: areinert@ice.mpg.de (A. Reinert).

hairs acting as the olfactory organ of the fly, and in further sense-associated organs like the compound eye and mouthparts. Therefore, we used µPIXE at the ion beam facility LIPSION in Leipzig [8]. This paper presents the spatially resolved concentrations of P, S, Cl, K, Ca, Fe, Cu and Zn in lyophilised head cryosections of Drosophila. The PIXE maps enable a detailed analysis of regions of particular interest down to a spatial resolution of 0.5 µm [9].

2. Materials and methods

2.1. Flies

Drosophila melanogaster wild type flies (wild type Berlin) aged 1–3 weeks were used. Flies were reared in standard food medium containing following substituents per litre: 648 ml of water, 118 ml of sugar beet syrup, 95 g of corn meal, 11 g of yeast, 4.1 g of agar, 3.3 ml of nipagin (30%) and 2.4 ml of propionic acid. Flies were kept at 25 °C and 60% relative humidity with a 12:12 h light:darkness cycle.

2.2. Head cryosections

Cryofixation and cryosectioning are essential prerequisites to analyse the elemental concentrations of electrolytes, because a solvent treatment might cause redistribution or even extraction of soluble elements.

Living flies were transferred in self-made rod-like plastic dishes filled with Tissue-Tech O.C.T. compound and immediately frozen by immersing the dish in liquid nitrogen chilled isopentane. The rod of frozen compound with the embedded flies was removed from the dish and positioned in the cryotome (Microm HM560). Frontal sections (14 µm and 25 µm, respectively) of the head were cut, and freeze dried over night (ALPHA 2–4 Christ GmbH). It was assured that the sections remained frozen all the time until freeze-drying. The dried sections were prepared as self-supporting samples on a striped aluminium holder, or were transferred on Depex foil or between two Parafilm® foils fixed on a sample holder, respectively.

2.3. Ion beam microscopy and analysis

The quantitative elemental mapping was carried out at the Leipzig ion nanoprobe LIPSION using a 2.25 MeV proton beam with a current of up to 1 nA. The spatially resolved element distributions of P, S, Cl, K, Ca, Fe and Zn were recorded by Particle induced X-ray emission (PIXE). The spatial resolution was 0.5 µm for all scans excepted whole head section scans with 1 µm spatial resolution. Backscattering spectrometry (BS) was simultaneously used to obtain information on the matrix composition (C, N, O, and H indirectly), on the sample thickness and the accumulated beam charge using the RUMP code for BS-spectrum fitting.

For quantitative analysis of the PIXE data we used GeoPIXE to extract element profiles and concentrations in regions of interest. Since the basic unit of quantitative PIXE results is mass per unit area, we normalised these values by the original thickness of the analysed section to obtain the results in mass per volume. It is important to refer to the section thickness as prepared. The unit mass per volume easily converts into the unit mM. GeoPIXE versions 4.0 or later now provide the option to select the concentration units µg/g, mM and ng/cm^2.

3. Results and discussion

By using the µPIXE facility LIPSION we were able to spatially resolve the ion concentrations in head sections of the vinegar fly Dro-

sophila melanogaster. We focused on the elements P, S, Cl, K, Ca, Fe, Cu and Zn. Na was unfortunately not detectable via PIXE due to the limited detector efficiency below 2 keV.

Quantitative element maps were used to extract the ion concentrations in regions of interest (ROIs). The results are given in Fig. 1 for the brain, the antenna, the compound eye, the mouthparts and the average values from all regions, respectively. The most prominent element is P showing the highest concentration in the brain (162 mM in average). This might be due to the concentrated occurrence of neurons and glia cells, which do have an intense P concentration [10].

The second most prominent element in all analysed regions is K. Its concentration was unexpected high (up to 124 mM in the brain). This information might be useful for the mixture of the Drosophila Ringer's solution since for imaging analyses in our laboratory we use the recipe after [11] which contains just 5 mM K. It might probably be better to orientate on the protocol of [12] that describes a Drosophila Ringer's solution that is enriched with 182 mM K. However, the data of the present PIXE study are based on tissue regions instead of single cells, thus no information on the differentiation of the intra- and extracellular ion concentrations can be provided thus far.
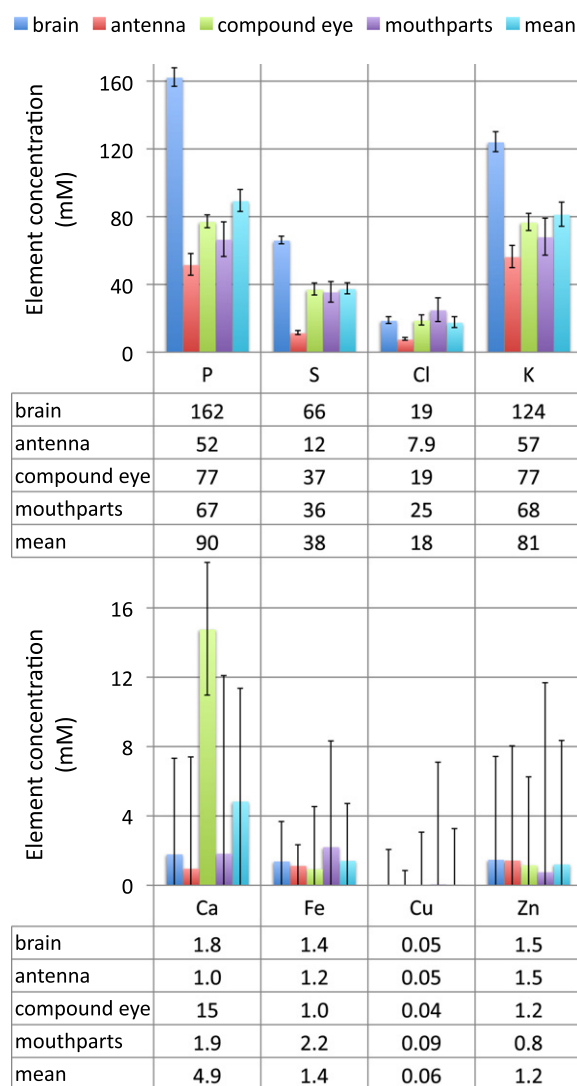

	P	S	Cl	K
brain	162	66	19	124
antenna	52	12	7.9	57
compound eye	77	37	19	77
mouthparts	67	36	25	68
mean	90	38	18	81

	Ca	Fe	Cu	Zn
brain	1.8	1.4	0.05	1.5
antenna	1.0	1.2	0.05	1.5
compound eye	15	1.0	0.04	1.2
mouthparts	1.9	2.2	0.09	0.8
mean	4.9	1.4	0.06	1.2

Fig. 1. Element concentrations (mM) in different compartments of the Drosophila head. Special focus is given to P, S, Cl, K, Ca, Fe, Cu and Zn. Data include the measurement of 23 sections of n_{flies} = 6 in total. Error bar: standard error.
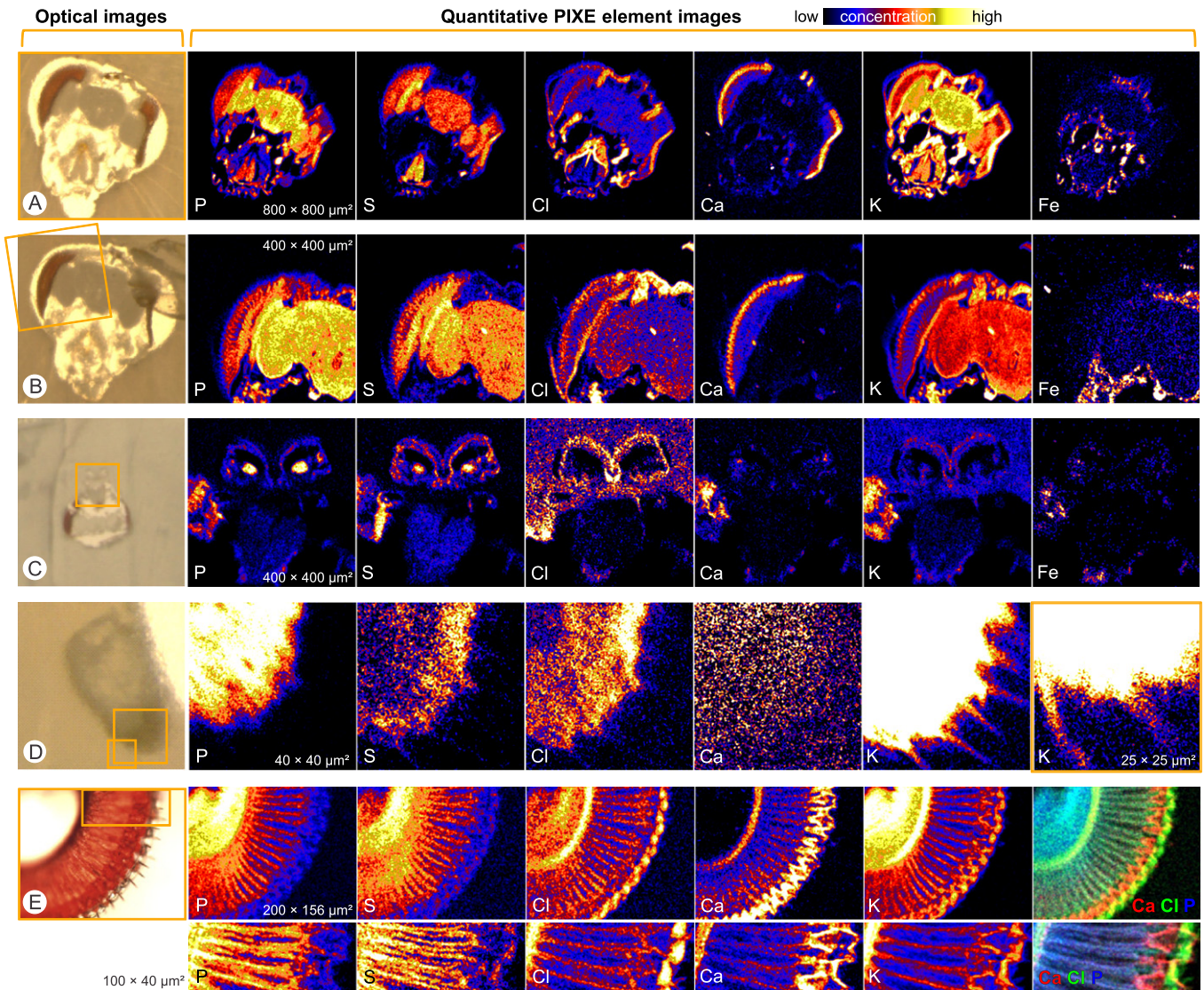
Fig. 2. Spatially resolved element concentrations in *Drosophila* head sections analysed by PIXE. Shown are P, S, Cl, K, Ca and Fe in single element maps. The analysed areas are highlighted in the optical images: (A) whole head section, (B) brain/compound eye, (C) proboscis/pharynx, (D) antenna/sensilla, (E) compound eye/ommatidia.
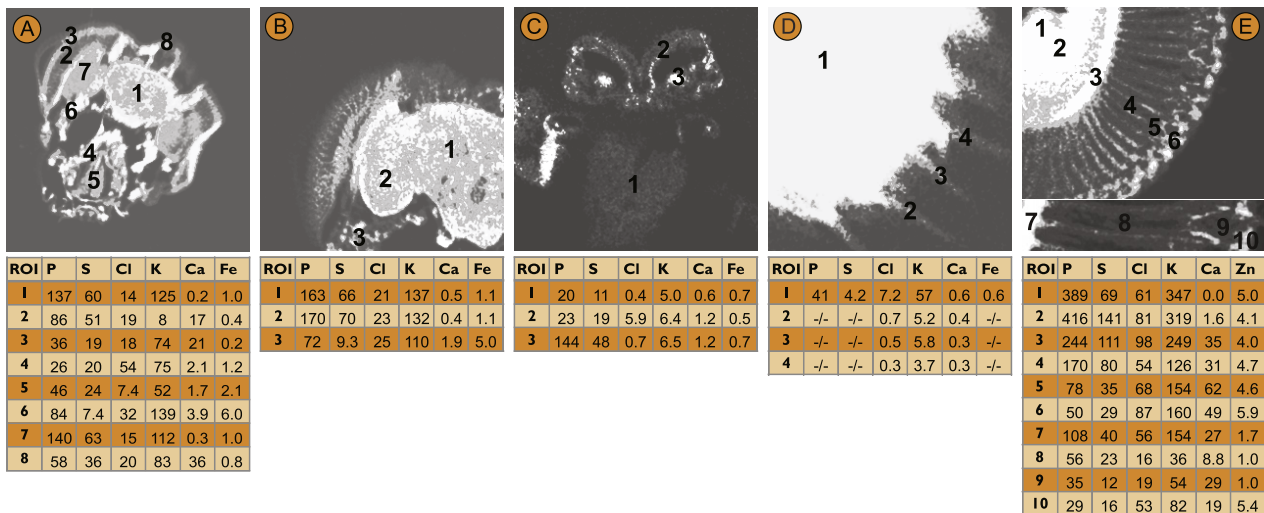

A

ROI	P	S	Cl	K	Ca	Fe
1	137	60	14	125	0.2	1.0
2	86	51	19	8	17	0.4
3	36	19	18	74	21	0.2
4	26	20	54	75	2.1	1.2
5	46	24	7.4	52	1.7	2.1
6	84	7.4	32	139	3.9	6.0
7	140	63	15	112	0.3	1.0
8	58	36	20	83	36	0.8

B

ROI	P	S	Cl	K	Ca	Fe
1	163	66	21	137	0.5	1.1
2	170	70	23	132	0.4	1.1
3	72	9.3	25	110	1.9	5.0

C

ROI	P	S	Cl	K	Ca	Fe
1	20	11	0.4	5.0	0.6	0.7
2	23	19	5.9	6.4	1.2	0.5
3	144	48	0.7	6.5	1.2	0.7

D

ROI	P	S	Cl	K	Ca	Fe
1	41	4.2	7.2	57	0.6	0.6
2	-/-	-/-	0.7	5.2	0.4	-/-
3	-/-	-/-	0.5	5.8	0.3	-/-
4	-/-	-/-	0.3	3.7	0.3	-/-

E

ROI	P	S	Cl	K	Ca	Zn
1	389	69	61	347	0.0	5.0
2	416	141	81	319	1.6	4.1
3	244	111	98	249	35	4.0
4	170	80	54	126	31	4.7
5	78	35	68	154	62	4.6
6	50	29	87	160	49	5.9
7	108	40	56	154	27	1.7
8	56	23	16	36	8.8	1.0
9	35	12	19	54	29	1.0
10	29	16	53	82	19	5.4

Fig. 3. PIXE maps from Fig. 2 were used to analyse regions of interest (ROIs). The corresponding tables present the element concentrations in mM of the ROIs.
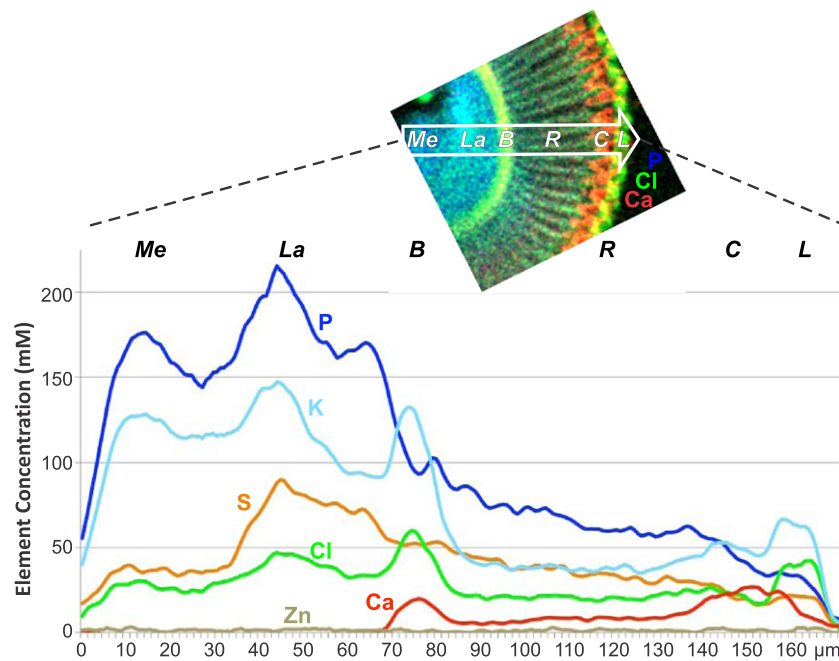
Fig. 4. Elemental profile in radial direction through the layers of the compound eye. The three-element-map (Ca, Cl, P) demonstrates the following layer: medulla (*Me*), lamina (*La*), basal lamina (*B*), rhabdom layer (*R*), crystalline cone layer (*C*) and corneal lens layer (*L*). The different elemental distributions might reflect the different functions of the individual compartments of the compound eye.

S is the third most present element with the highest content also in the brain (66 mM).

The concentration of Cl was unexpected low (18 mM in average). This is much less than used in the two recipes mentioned above (143 mM [11] and 234 mM [12], respectively). Even though Cl is a highly volatile electrolyte an artefact in our data is unlikely since the sample preparation was done in an ion conservative way (see Section 2).

The Ca concentration is 4.9 mM in average and matches the Ca concentration used in the Ringer's solutions. One exception is the compound eye showing in average a three times higher (15 mM) Ca concentration than the mean value (Fig. 1), whereby certain layers even possess a ten times higher Ca concentration (for example Fig. 3E, ROI #6 (49 mM) and ROI #5 (62 mM)). The extraordinary high content of Ca in special layers of the compound eye was already obvious in the PIXE maps (Fig. 2A,B, and E; Fig. 4, discussed below).

The concentration of Fe and Zn is low (in average 1.4 and 1.2 mM, respectively). Cu with an average concentration of 0.06 mM is near the limit of quantification.

Fig. 2 shows a set of quantitative element maps from various aspects of *Drosophila*'s head. We applied several scan sizes from $800 \times 800\ \mu m^2$ for whole head sections (Fig. 2A) down to $25 \times 25\ \mu m^2$ for olfactory sensilla hairs on the antenna (Fig. 2D, zoomed K map). The element concentrations extracted from particular ROIs are given tabulated in Fig. 3. The ion content of whole olfactory sensilla hairs could not be quantified, because they are smaller in diameter (approximately 2.5 μm) than the thickness of the slices (14 and 25 μm, respectively). Thus, the reduction of the element concentration in the PIXE maps (Figs. 2D and 3D) is due to the decreasing, but unknown thickness of the truncated sensilla. For a reliable quantification of element concentrations in sensilla hairs individual PIXE maps with sub-micron resolution from single sensilla are required. This will be a subject of a further study.

Certain structures or compartments accumulate special elements with a conspicuously high preference. Some structures of the mouthparts for example are enriched in Fe (Fig. 3A, ROI #6), whereby other parts like ROI #4 in Fig. 3A or the outer surrounding

of the proboscis (Fig. 3C, ROI #2) are characterised by a high content of Cl. The inner core of the proboscis instead is enriched in P (Fig. 3C, ROI #3). The different distribution of the elements in the mouthparts might support functional tasks like the stabilization of the apparatus on the one site and an easy passage of food on the other site.

The high concentration of K is particularly obvious in the antenna and especially in the olfactory sensilla hairs (Figs. 2D and 3D). The thin sensilla are visible just only in the K map, but not in the P map usually providing a good recognition and orientation within the biological sample.

The most prominent structure showing a concrete distribution of certain elements in particular cell layers is the compound eye (Figs. 2A,B,E and 3A,B,E). The compound eye is composed of many closely packed facets, the ommatidia, which are the structural and functional units of vision. The ommatidia can be recognised in the optical image of a compound eye section, but the PIXE analysis reveals an even more detailed structure and complex organisation (Figs. 2E and 3E). Especially the elements Cl, K and Ca are distributed in such a particular manner, that they characterise single compartments in the ommatidia (Figs. 2E and 3E). In a single ommatidium the concentration of Cl vary from 16 to 56 mM, of K from 36 to 154 mM and of Ca from 8.8 to 29 mM (Fig. 3E, ROIs #7–10).

To demonstrate the element distribution in the compound eye we applied a traverse within the PIXE map to extract the ion concentration along the radial axis of the eye (Fig. 4). The track crosses the medulla (Me) and the lamina (La) as parts of the optical lobes, the basal lamina (B), the light-sensitive rhabdomeres and surrounding retinula and pigment cells (R), crystalline cones and primary pigment cells (C) and terminating corneal lenses (L) on the surface of the eye. The medulla and the lamina contain the highest concentration of P and the lamina additionally of S. The decrease in P in between the two neuropiles represents the first optical chiasm. The content of P and S decreases continuously from now on. When reaching the basal lamina Cl, K and Ca are increased, but drop again in the section including the rhabdomeres. When reaching the layer of the crystalline cones the Ca and K concentrations increase. The

three-element-map, however, indicates that the Ca is not accumulated in the crystalline cones, but in the primary pigment cells aside. A speculation for the high Ca content is its role in the photo-transduction [13]. Interestingly, the ocelli, simple eyes located on the dorsal surface of the head, also show a remarkably high concentration of Ca (Fig. 3A, ROI #8). Closing the results for the traverse in Fig. 4 the corneal lenses are characterised by an increased concentration of Cl and K, respectively.

4. Conclusion

The present study presents quantitative element concentrations in head sections of adult *Drosophila melanogaster* flies with a spatial resolution of 0.5 μm. We provide information on P, S, Cl, K, Ca, Fe, Cu and Zn contents in whole head sections and regions of interests, particular in the brain, the antenna and its olfactory sensilla hairs, mouthparts, and the compound eye and single ommatidia. Different ion concentrations in the different compartments are presented. Furthermore, our findings let assume that the commonly used mixture for the artificial lymph, the *Drosophila* Ringer's solution, probably needs an adjustment of the Cl and K concentration to keep the experiments under physiological conditions.

Acknowledgements

References

[1] L.Y. Jan, Y.N. Jan, Properties of the larval neuromuscular junction in *Drosophila melanogaster*, J. Physiol. 262 (1976) 189–214.
[2] K.-E. Kaissling, Chemo-electrical transduction in insect olfactory receptors, Ann. Rev. Neurosci. 9 (1986) 121–145.
[3] R.A. Gleeson, H.C. Aldrich, J.F. White, H.G. Trapido-Rosenthal, W.E.S. Carr, Ionic and elemental analyses of the olfactory sensillar lymph in the spiny lobster *Panulirus argus*, Comp. Biochem. Physiol. 105 (1993) 29–34.
[4] H. Kijima, Y. Okada, S. Oiki, S. Goshima, K. Nagata, T. Kazawa, Free ion concentrations in receptor lymph and role of transepithelial voltage in the fly labellar taste receptor, J. Comp. Physiol. A 177 (1995) 123–133.
[5] R.A. Steinbrecht, K. Zierold, The electrolyte distribution in insect olfactory sensilla as revealed by X-ray microanalysis, Ann. NY Acad. Sci. 510 (1987) 638–641.
[6] J. Gödde, E.-R. Krefting, Ions in the receptor lymph of the labellar taste hairs of the fly *Protophormia terraenovae*, J. Insect Physiol. 35 (2) (1989) 107–111.
[7] R.M.S. Schofield, J.H. Postlethwait, H.W. Lefevre, MeV-Ion microprobe analyses of whole *Drosophila* suggest that zinc and copper accumulation is regulated storage not deposit excretion, J. Exp. Biol. 200 (1997) 3235–3243.
[8] T. Reinert, T. Andrea, N. Barapatre, M. Hohlweg, T. Koal, W. Larisch, A. Reinert, D. Spemann, J. Voigt, R. Werner, T. Butz, Biomedical research at LIPSION – Present state and future developments, These proceedings.
[9] T. Reinert, D. Spemann, M. Morawski, T. Arendt, Quantitative trace element analyses with sub-micron lateral resolution, NIM B 249 (1) (2006) 734–737.
[10] A. Fiedler, T. Reinert, M. Morawski, G. Brückner, T. Arendt, T. Butz, Intracellular iron concentration of neurons with and without perineuronal nets, NIM B 260 (2007) 153–158.
[11] A. Fiala, T. Spall, S. Diegelmann, B. Eisermann, S. Sachse, J.-M. Devaud, E. Buchner, C.G. Galizia, Genetically expressed Cameleon in *Drosophila melanogaster* is used to visualize olfactory information in projection neurons, Curr. Biol. 12 (2002) 1877–1884.
[12] W. Sullivan, M. Ashburner, R.S. Hawley, *Drosophila Protocols*, CSHL Press (2000), ISBN: 978-0879695866.
[13] R.C. Hardie, Phototransduction in *Drosophila melanogaster*, J. Exp. Biol. 204 (2001) 3403–3409.

Appendix C

3D ANALYSIS OF AN INDUCED ATHEROSCLEROTIC LESION IN A MURINE ARTERY BY PIXE STACKING

ANNEMARIE SICKERT

Nuclear Solid State Physics, Institute of Experimental Physics II, University of Leipzig, Linnéstr. 5

Leipzig, 04103, Germany

Frank.Sickert@t-online.de

NIRAV BARAPATRE[1]

Nuclear Solid State Physics, Institute of Experimental Physics II, University of Leipzig, Linnéstr. 5

Leipzig, 04103, Germany

barapatre@physik.uni-leipzig.de

MARTIN ROTHERMEL

Nuclear Solid State Physics, Institute of Experimental Physics II, University of Leipzig, Linnéstr. 5

Leipzig, 04103, Germany

rothermel@physik.uni-leipzig.de

DANIEL TEUPSER

Institute of Laboratory Medicine, Clinical Chemistry and Molecular Diagnostics, University of Leipzig,

Liebigstr. 27

Leipzig, 04103, Germany

Daniel.Teupser@medizin.uni-leipzig.de

TILO REINERT

Department of Physics, University of North Texas, 1155 Union Circle

Denton, TX76203, USA

tilo@unt.edu

Received

Revised

ABSTRACT

Quantitative three dimensional analysis is possible, in principle, by PIXE tomography. But, the inherent problems in quantitation, restrictions on the sample geometry and preparation, and specimen damage due to high fluences make this method unsuitable for many biological samples. The specimen under investigation, a murine artery, was around a millimeter in diameter and the induced atherosclerotic lesion was spread few hundreds of micrometers across the length of the artery. Since no tomographic experiments were possible, we chose to do the 3D quantitative analysis

1 *Nirav Barapatre*

Nuclear Solid State Physics, Institute for Experimental Physics II

Faculty for Physics and Earth Sciences, University of Leipzig

Linnéstr. 5, 04103 Leipzig, Germany

by means of PIXE Stacking. Herein, thin serial sections of the specimen are prepared and measured by conventional ion beam techniques. The resultant two dimensional quantitative element maps are stacked and aligned to reconstruct a quantitative volume of the specimen. Although the reconstructed dimension has poorer spatial resolution as compared with the measured dimensions, new information can still be gained from it. The three dimensional element distribution of the atherosclerotic lesion shows calcification on the outer surface of the artery, which otherwise would not have been easily visible in the two dimensional analysis.

1. Introduction

Commendable efforts have been made in past to do quantitative tomography with a particle beam.[1-3] Whereas it is relatively simple to create 3D mass density distribution map by scanning transmission ion microscopy tomography (STIM-T)[4], quantitative elemental analysis by proton induced X-ray emission tomography (PIXE-T) is yet to establish itself. The calculation of accurate element concentration in PIXE-T gets complicated as one has to correct for beam broadening effects, changes in ionization cross-section along the ion track and the attenuation of fluorescence yield within the sample.[5, 6] Further restrictions are imposed if biological tissues are to be analyzed. The samples must be prepared free-standing as far as possible in order to avoid further source of inaccuracy due to the mounting media. On the other hand, a free-standing sample would deteriorate readily as a result of high fluences employed in PIXE-T. Andrea et al[7] performed limited angle tomography of single cells grown on a substrate to overcome the sample preparation limitations. They used an average fluence of 500 pC/μm² per map to avoid the sample deterioration. The penetration depth of protons of few MeV energy in biological tissue is less than 500 μm.[5] But, reliable values for element concentration in PIXE-T can only be achieved if the specimen thickness is significantly lower than the range of ion beam in it. A strand of human hair, for example, can be measured by PIXE-T.[8] A murine coronal artery, on contrary, is around a millimeter in diameter and, therefore, unsuitable for the tomographic measurements.

Atherosclerosis is a progressive inflammatory disease of large and medium sized arteries. The lesions are characterized by accumulation of lipid-rich material and fibrous elements within the intimal layer of the artery wall.[9,10] To study the progression of the disease mutant mouse models are used. Many microbeam studies have investigated the role of trace elements in the atherogenesis by two dimensional sectional analysis.[11-13] In general, a lesion is spread few hundreds of micrometers along the artery. Hence, a three dimensional investigation is required. Since the specimen in present study is unsuitable for PIXE-T, we propose a different method for three dimensional analysis by means of PIXE Stacking. Herein, the specimen is first cut serially in thin sections. The thickness of the sections is selected in such a way that the loss in energy of the incident particle beam is negligible. Each section is then analyzed by the ion beam techniques. The resulting 2D element maps of the sections are stacked in the same sequence as they were cut and aligned to render a 3D quantitative distribution of the elements.

2. Materials and Methods

2.1. *Tissue Preparation*

A LDL-Receptor deficient mouse was raised on low fat, semi-synthetic diet with 0.02 % cholesterol, which subsequently developed atherosclerosis.[14] A control mouse was raised on normal diet and showed no significant atherosclerotic lesions. Both the mice were sacrificed humanely at the age of 20 weeks. The brachiocephalic artery was cut at the branching point from the aorta and 1 mm distal to its bifurcation into the subclavian and carotid arteries. It was then frozen in a mounting medium (OCT Compound, Tissue Tek®). 49 serial sections of 10 μm thickness each were obtained with a cryomicrotome (LEICA CM 1900) at -25 °C. Three sections were lost during the preparation procedure. The remaining 46 sections were brought on glass slides with a fresh coating of embedding resin DePeX (Serva). The sections attached to the polymer foil were then transferred to appropriate aluminum holders for the ion beam analysis.

2.2. *Ion Beam Analysis*

The quantitative microscopy measurements were done at LIPSION, the accelerator laboratory of the University of Leipzig. The samples were irradiated in vacuum with 2.25 MeV proton beam focused to a spot-size of 1.2 μm. The PIXE (Particle Induced X-ray Emission) and BS (Backscattering) events were registered simultaneously with a HPGe (High Purity Germanium) X-ray detector placed at 135 degrees and a PIPS (Passivated Implanted Planar Silicon) annular ring detector placed at 180 degrees, respectively. The BS spectra were analysed with the routine RUMP[15] to determine the lighter matrix elements and the incident charge on the sample. This information was used in the analysis of the PIXE spectra by the routine GeoPIXE.[16] The elements present in sample with atomic number greater than that of aluminum were quantified.

3. Results and Discussion

2.1. *2D Analysis*

The control mouse fed on a normal diet did not exhibit atherosclerotic lesions, whereas there is significant lesion-based narrowing of the lumen in the LDL-Receptor deficient mouse. The presence of calcium suggests the onset of calcification of artery walls and that the lesion is in an advanced stage. Figure 1 is a three element map (P, S and Ca) of a section in greyscale. A smaller and closer scan reveals precipitation of calcium in intimal and medial arterial wall and co-localization of calcium and phosphorous in form of microspots. The average calcium to phosphorous ratio in these microcalcifications was measured to be around 2.9. This corresponds to amorphous calcium phosphate as found by a previous study on post mortem human samples.[11] A ROI (Region of Interest) was put around the lesion and the elements present within were quantified. Table 1 shows the mean element concentration of 46 sections against 9 control sections. The concentration of calcium in the lesion is ten times higher than in the healthy artery. The phosphorus

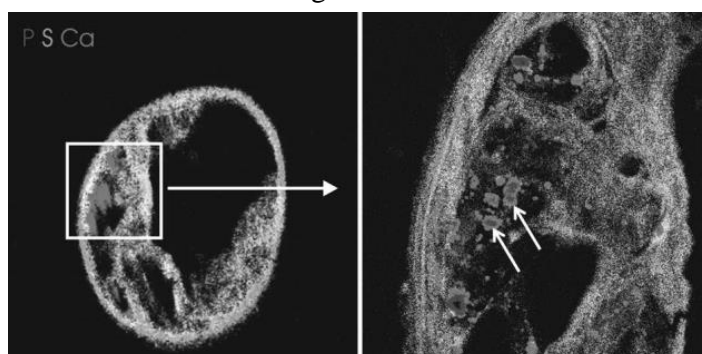concentration in the lesions is twice as high as in the control arteries.

Fig. 1. Three element map of P, S and Ca of the whole scan area (1200 × 1200 μm²) on the left side and of a part of the lesion area (300 × 300 μm²) on the right side. The arrows in the right image point to microspots of high Ca and P concentration. These microspots represent microcalcifications in the lesion.

This is expected due to presence of phospholipids, macrophages and other necrotic material inside the lesion. The sulphur maps act as an indicator for the spatial extent of the lesion. We did not measure any significant change in sulphur content. Iron, on the other hand, is significantly increased inside the lesion. Elevated levels of iron in the atherogenesis have been reported earlier.[12] Iron is known for its pro-oxidative role by production of reactive oxygen species through Fenton reaction. Elevated levels of iron suggest its complicity in the progression of the disease. In contrast, zinc may play a protective role against atherosclerosis by reducing the iron level in the lesion.[12] Since the embedding material was contaminated with zinc we cannot comment on any differences in the zinc content. The role of chlorine and potassium in the formation of the lesions is vague. Both elements have a higher content in the lesions (41 mmol/l and 8 mmol/l) than in the control arteries (20 mmol/l and 1.1 mmol/l). It is difficult to interpret this result as these are electrolyte elements and vulnerable to preparation procedures.

Table 1. The mean element concentration in the lesion is compared against the mean element concentration in the control arteries.

	P^a mmol/l	S mmol/l	Cl^a mmol/l	K^a mmol/l	Ca^a mmol/l	Fe^a mmol/l	Zn^a mmol/l
Atherosclerotic lesions (n=46)	46 (1.8)	47 (1.8)	41 (1.9)	8.0 (0.4)	17 (1.5)	0.7 (0.04)	1.3 (0.07)
Control arteries (n=9)	23 (1.3)	52 (2.3)	20 (1.0)	1.1 (0.1)	1.7 (0.1)	0.4 (0.07)	1.8 (0.13)

Note: The uncertainity value in the brackets represents the standard error of the mean.
[a]Student's t-test: $p < 0.001$

2.2. 3D Analysis

For the three dimensional analysis a program was written that allows the alignment of the sections by manual rotation and translation. Each section is aligned to the preceding section and the quality of the alignment is judged by the eye. The aligned 2D element maps are exported as a three dimensional data set. It is then visualized by the iVolume routine of IDL (Interactive Data Language) from ITT Visual Information Solutions, where to each concentration value a color value is assigned. Hence, the quantitative

character is preserved. The aim was to create a stack of all 46 artery sections leading to a stack height of 460 μm. However, there was substantial change in the shape of many sections during the cutting process. So, the similarity was lost in the successive sections. But, we could create four different stacks with up to seven serial slices per stack. We present here the stack with maximum number of unchanged serial sections. Figure 2 shows the 2D sulphur maps of these slices and a 3D sulphur stack. Figure 3 shows individual and composite stacks P and Ca. The new third dimension clearly shows calcification on the outer surface of the artery wall. This property would not have easily been visible in the 2D maps.
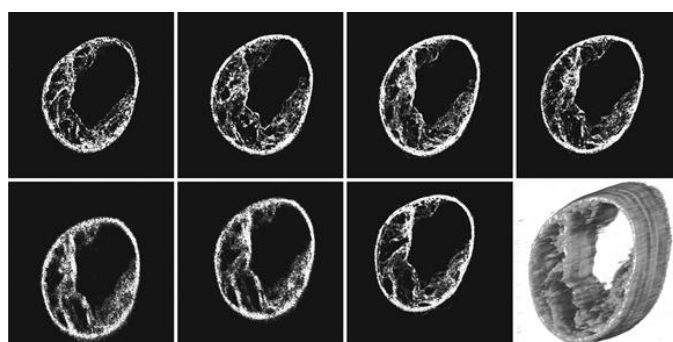
Fig. 2. Sulphur element maps of the 7 artery slices that were chosen to create a stack. These arteries were aligned to each other manually and then stacked in this order to a quantitative volume.

Fig. 3. On the left are the 3D concentration maps of phosphorous and calcium in black color. On the right is a composite volume of these two elements. Phosphorous is rendered in black and calcium in white color. Calcification on the upper outer surface of the artery is only visible in this 3D element distribution map.

4. Conclusion

The atherosclerotic lesions of the 20 weeks old LDL-receptor deficient mouse show a high concentration of phosphorous and calcium. These calcifications appear in microspots (microcalcifications) and they have a Ca/P ratio of 2.9, which corresponds to amorphous calcium phosphate. The higher iron content in the lesion verify that iron abet the process of atherogenesis.

Through alignment and stacking of the two dimensional element maps it was possible to create a three dimensional visualization of a part from the murine artery. Although a limited number of slices were available, we could present information from the newly gained dimension. The problem of sample deformation can be eliminated by optimizing the preparation procedure. The method of stacking provides a tool for 3D analysis of samples, which otherwise are unsuitable for tomographic experiments. It can even be a preferred method of analysis, if the specimen can easily be sectioned, as the

quantification of elements is less cumbersome and more accurate.
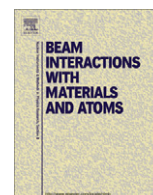
Acknowledgments

References

1. C. Habchi, D. T. Nguyen, Ph. Barberet, S. Incerti, Ph. Moretto, A. Sakellariou and H. Seznec, Nucl. Instr. and Meth. B 267 (2009) 2107.

2. T. Satoh, M. Oikawa and T. Kamiya, Nucl. Instr. and Meth. B 267 (2009) 2125.

3. M. Rothermel, T. Reinert, T. Andrea and T. Butz, Nucl. Instr. and Meth. B 268 (2010) 2001

4. T. Andrea, M. Rothermel, T. Butz, T. Reinert, Nucl. Instr. and Meth. B 267 (2009) 2098.

5. C. Michelet-Habchi, S. Incerti, P. Aguer, Ph. Barberet, E.Gontier, T. Guinefolleau, Ph. Moretto, A. Pouthier, T. Pouthier and R. W. Smith, IEEE Trans. Nucl. Sci. 52 (2005) 612.

6. D. Beasley and N. M. Spyrou, J. Radioanal. Nucl. Chem. 264 (2005) 289

7. T. Andrea, M. Rothermel, R. Werner, T. Butz and T.Reinert, Nucl. Instr. and Meth. B 268 (2010) 1884.

8. D. Beasley, I. Gomez-Morilla and N. M. Spyrou, J. Radioanal. Nucl. Chem. 276 (2008).

9. Aldons J. Luis, Nature 407 (2000) 233.

10. Russell Ross, N. Engl. J. Med. 340 (1999) 115.

11. R. B. Roijers, R. K. Dutta, J. P. M. Cleutjens, P. H. A. Mutsaers, J. J. M. de Goeij and G. J. van der Vusse, Anal. Chem. 80 (2008) 55.

12. F. Watt, R. Rajendran, M. Q. Ren, B. K. H. Tan and B. Halliwell, Nucl. Instr. and Meth. B 249 (2006) 646.

13. M. Ren, R. Rajendran, P. Ning, B. Tan Kwong Huat, O. Choon Nam, F. Watt, A. Jenner and B. Halliwell, Free Radic. Biol. Med. 41 (2006) 222.

14. D. Teupser, A. D. Persky and J. L. Breslow, Arterioscler Thromb Vasc Biol. 23 (2003) 1907.

15. L. R. Doolittle, Nucl. Instr. and Meth. B9 (1985) 344.

16. C. G. Ryan, Nucl. Instr. and Meth. B181 (2001) 170.

Appendix D

Biomedical research at LIPSION – Present state and future developments

T. Reinert [a,b,*], T. Andrea [a], N. Barapatre [a], M. Hohlweg [a], T. Koal [a], W. Larisch [a], A. Reinert [a], D. Spemann [a], J. Vogt [a], R. Werner [a], T. Butz [a]

[a] Universität Leipzig, Institut für Experimentelle Physik II, Linnéstr. 5, 04103 Leipzig, Germany
[b] University of North Texas, Department of Physics, 1155 Union Circle, Denton, TX 76203, USA

ARTICLE INFO

ABSTRACT

Since its commissioning in 1998 the high energy ion nanoprobe LIPSION has been developed into a versatile tool for a variety of applications in biomedical research. It includes quantitative trace element analysis with sub-micron spatial resolution and 3D-element imaging, as well as 2D- and 3D-microscopy of density distributions. The analytical methods base on particle induced X-ray emission spectrometry (PIXE) and PIXE-tomography, Rutherford backscattering spectrometry (RBS), as well as scanning transmission ion microscopy (STIM) and STIM-tomography.

The continuous developments led to improved capabilities for trace element analysis. For sub-micron analysis the spatial resolution could be improved to 0.3 μm for high resolution work and to 0.5 μm for routine analysis. On the other hand, LIPSION was optimized for high sample throughput in quantitative element imaging maintaining a lateral resolution of 1–2 μm. Recently the methods of PIXE- and STIM-tomography of biological specimens have been extended to limited angle tomography to avoid the complicated preparation of free-standing samples.

Besides its analytical applications, the nanoprobe is also used for targeted irradiation of living cells with counted single ions for radiobiological research. It is capable of irradiating up to 20,000 cells per hour. Furthermore, we have developed a technique to achieve confined cell growth based on the proton beam writing technique (PBW) and agar. The paper presents an overview of the current biomedical research fields at LIPSION and gives an outlook on prospective developments.

© 2011 Elsevier B.V. All rights reserved.

1. Introduction

The great versatility of nuclear microprobes is demonstrated by the vast number of studies that have been performed during the last 40 years since the first nuclear microprobe has been built by Cookson [1]. Hereby, the applications in biological and biomedical fields were always a major part. During the last three series of the International Conference on Nuclear Microprobe Technology and Applications, 2006 in Singapore [2], 2008 in Debrecen [3], and 2010 in Leipzig (this proceedings), the percentage of contributions with relation to biological or biomedical research was almost 30%. Although nuclear microprobes are still considered experimental physics facilities, their broad applicability leads to more beam time requests from external users. Not only the increased beam time demands but also demands for further developments of the analytical capabilities or the development of existing applications such as micro-irradiation of living cells push nuclear microprobes towards user facilities with a broad interdisciplinary spectrum.

Several laboratories with nuclear microprobes have already developed or are currently constructing dedicated beamlines for applications in life science research. Most prominent examples are beamlines or specialized end-stations for micro-irradiation of living cells [4–11]. These facilities serve the radiobiology community to study the cellular response to targeted single MeV-ion irradiation. But also highly specialized nuclear microprobe set-ups for the analysis of biological material or single cells have been developed [12,13].

The Leipzig high energy ion nanoprobe LIPSION has been designed from scratch for applications of various ion beam analytical and modification techniques, using H^+, H_2^+, or He^+ ions, in materials, biological and biomedical research. The components, the laboratory building with a high stability air-conditioning system and deep-seated concrete baseplates, the ion accelerator Singletron™ with a high ion source brightness [14], the probe forming lens system of high demagnification configured in a split Russian quadruplet [15], and the passive shielding of the beam line against magnetic stray fields were chosen according to the actual knowledge at that time.

* Corresponding author at: University of North Texas, Department of Physics, 1155 Union Circle, Denton, TX 76203, USA. Tel.: +1 940 369 5188; fax: +1 940 565 2227.
E-mail address: tilo.reinert@unt.edu (T. Reinert).
URL: http://www.phys.unt.edu (T. Reinert).

Since 1998, when LIPSION started operation, its performance has been continuously improved. Among others there is the increase of spatial resolution [16], the reduction of beam time needed for analysis, mainly by increasing the beam current density [17], or the enhancement of the analytical capabilities by introducing tomographic techniques [18]. A summary of the improvements and a detailed list of the present specifications are given by Spemann [19].

This paper presents examples from recent and present research activities with life science background using quantitative element microscopy, scanning transmission ion microscopy, proton beam writing in agar to achieve confined cell growth, and single ion irradiation of living cells. Finally, a prospect on future developments is given.

2. Technical set-up

The 3.5 MV Singletron™ accelerator provides H^+, H_2^+, or He^+ ions that are transferred into the nanoprobe beamline through a Danfysik 90° analyzing magnet. The theoretical demagnification of the ion optical system of the nanoprobe is 104 in both directions (calculation with PRAM-Propagate Rays and Aberrations by Matricies), but effective demagnifications of up to 130 can be experimentally deduced from measured beam spot sizes and corresponding object/aperture settings [17]. Due to the long working distance of the system of 330 mm the electro-magnetic beam scanner is situated between the last quadrupole lens and the sample chamber. The metallic beam tube through the scanner was replaced by a glass tube to prevent eddy currents. An internal silver coating with longitudinal scratches electrically neutralizes the glass tube. Thus, reliable fast beam scanning with dwell times as low as 20 µs and beam jumping from one position to another are achieved. Scan widths from below 5 µm to more than 3 mm are accessible with pixel resolutions up to 4096.

A large multi-purpose sample chamber has been developed to meet the needs for in-vacuum analysis and in-air irradiation. It contains a computer controlled x-/y-/z-/θ-stage for sample positioning with an additional φ-/x'-/y'-goniometer for tomographic measurements (all from Feinmess Dresden GmbH, Germany). The overall positioning accuracy is in the order of 1 µm for the translation and 0.015° and 0.005° for θ and φ, respectively. Two optical microscopes, custom-made by TSO (Thalheim Spezial Optik, Germany) are available: one retractable high resolution (ca. 1 µm) rear microscope with LED ring illumination and a wide field (6 ×4.5 mm) long distance (65 mm) front microscope 45° above the incident beam with in-built Scheimpflug correction for the tilted plane of focus. Both microscopes use digital cameras to display their images on a computer screen.

The sample chamber is equipped with several detectors: (1) In standard 135° geometry a retractable 100 mm² HPGe photon detector (up to 150 msr) for PIXE or low energy PIGE (particle induced Gamma-ray emission) measurements with a 25 µm Be-window and polyethylene proton stop filter of appropriate thickness. A second detector (Canberra GUL0110) was purchased to double the solid angle. However, it had to be used instead as a replacement of the first detector (EG&G Ortec IGLET-X) which could not be satisfactorily repaired after its breakdown in 2008. (2) Five-segment annular PIPS particle detector (Canberra, total solid angle of 100 msr) for the spectrometry of backscattered particles. (3) PIN-diode (S1223-01, Hamamatsu) for the spectrometry of transmitted particles. (4) MD-502 channeltron (Amptek) for the detection of secondary electrons.

For the charge measurement three options are available, a Faraday-cup behind the sample, charge measurement from the insulated target holder and a new, so called pre-aperture pick-up [20]. It uses a calibrated beam current at a specially designed pre-aperture diaphragm as a measure for the beam current on the sample. The calibration is done prior sample analysis using the ratio of the beam currents of pre-aperture pick-up and Faraday-cup without any sample.

For in-air irradiation experiments the top of the chamber is removed and an adjustable beam exit nozzle with a 200 nm thin Si_3N_4 window of 2×2 mm² area is mounted on the inner side of the chamber to extend the beam tube to the beam focus position.

3. Applications

3.1. Ecology and anatomy

The spectrum of LIPSION's applications in life science research during the last 12 years is relatively broad. It started already with challenging high resolution work on elemental analysis of micron-sized samples, e.g. single aerosol particles ($PM_{2.5}$) to study the air pollution sources in Shanghai [21], or the analysis of the elemental distributions in individual algae cells to study modifications in metal bioaccumulation [22]. First sub-100 nm imaging was achieved with the visualization of individual collagen fibers down to 200 nm in diameter in joint cartilage by scanning transmission ion microscopy which is shown in Fig. 1. Although the beam spot is well below 100 nm the influence of stray fields is readily visible as image distortions. However, the STIM-study revealed the architecture of the collagenous network in knee joints, in particular it confirmed regions of fiber alignment with preferred directions which was anticipated by nuclear magnetic resonance imaging and polarized light microscopy [23].

3.2. Neurobiology – perineuronal net

An approach to better understand neuropathologies is the investigation of the selective neuronal vulnerability. There is a noticeable correlation between selective neuronal vulnerability and the heterogeneous distribution pattern of a subpopulation of neurons that express a reticular neuronal coating of extracellular matrix proteoglycans, a so called perineuronal net (PNN). This correlation is in particular remarkable since the vulnerability in
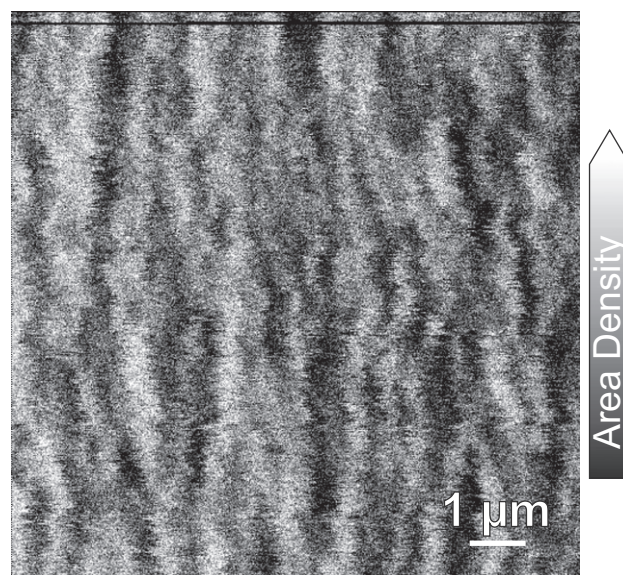

Fig. 1. STIM (10µm × 10 µm) of radially aligned collagen fibers within the center region of tibial joint cartilage (domestic pig, cryofixed and freeze-dried 10 µm thick section). The image distortions are due to stray magnetic fields.

relation with anatomy and the regional and cellular characteristics can be linked to a disturbed metal homeostasis, especially to iron (mis-)management.

In regions with physiologically higher iron concentrations the iron is compartmentalized mainly in oligodendrocytes; it is essential for the support of axons and for the production of myelin sheath. Free excess iron ions contribute to cellular damage by catalyzing oxidative stress. However, in the regions of pathologically higher iron concentration, where a progressive loss of neurons takes place for instance in Parkinson's and Alzheimer's diseases, a particular group of neurons is not or at least very lately affected by degeneration. This group obviously posses a certain protection mechanism. Numerous indications suggested that the polyanionic extracellular matrix proteoglycans, the PNNs, are involved in the protection mechanism [24,25].

According to the polyanionic character of the perineuronal nets, a possible neuroprotective effect could be based on the ability to scavenge iron ions, thereby reducing the oxidative stress. The ability to scavenge cations has to be connected with a high affinity to metal ions. In order to determine the affinity, transverse sections (6 μm thick) of an adult Wistar rat were incubated with gradually increasing concentrations of colloidal iron hydroxide. The concentrations of iron bound to the perineuronal nets were analyzed for the different Fe loadings in several brain regions [26]. The result for the cortex is shown in Fig. 2. The distinct affinity to iron ions is shown in the sharp increase of the bound iron already at a low iron loading.

This affinity could be an auxiliary mechanism of the perineuronal net ensheathed neurons that is part of a specialized cellular iron metabolism to eliminate the excess iron. Therefore, in a follow-up study, the physiological intraneuronal concentration of iron in the cytoplasm was investigated with a special emphasis to the difference between neurons ensheathed by a perineuronal net and neurons without a net. For the analysis Wistar rat brain sections including the regions of the substantia nigra, nucleus ruber, subiculum, parietal cortex, brain stem and cerebellum were prepared. The challenge was to analyze the subcellular distribution of iron at physiological concentrations maintaining the high spatial resolution of 1 μm.

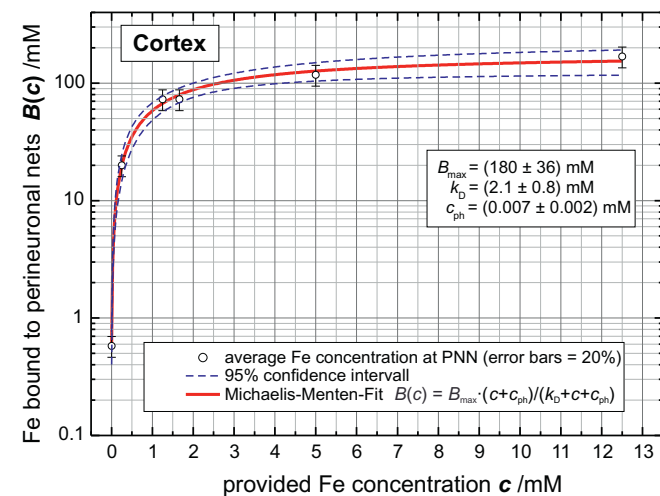Normally the perineuronal nets are neither visible in optical microscopy nor in ion beam microscopy. Although, after very long acquisition times perineuronal nets seem to slightly show up via an increased contrast in the sulfur map due to their main components chondroitin sulfate proteoglycans, this is not a suitable method for a fast and reliable recognition of the perineuronal nets. Other appropriate recognition techniques had to be established. The idea connected standard immune- or lectin-histochemical methods with a selective elemental contrast for ion beam microscopy [27]. The method can easily tag a variety of physiological structures by immune-labeling with primary antibodies in combination with a secondary antibody intensified by an elemental additive appropriate for ion beam analysis (e.g. Co, Ni, Cd, Ag, Au of highest purity). Tests have shown that there is no significant change in elemental concentrations of cells due to the labeling with an elemental marker (Fig. 3).

With this method the perineuronal nets were labeled with nickel to facilitate the PNN visualization by ion beam microscopy. A detailed analysis with high spatial resolution and sensitivity was then performed on selected neurons [28]. Concentration values for the different cellular compartments were extracted such as for the nucleolus, the nucleus (with/without nucleolar contributions), the cytoplasm, and the total neuronal concentrations (Fig. 4). Similarly, the total cell Fe-concentrations of more than 300 neurons with and without a PNN were extracted. The statistical analysis of the data revealed a higher intraneuronal iron concentration in neurons ensheathed by PNNs than in neurons devoid of PNNs on the significance level of $p < 0.01$ for the parietal cortex and the subiculum and $p < 0.02$ for the substantia nigra. The results from the analysis of the iron concentration together with further studies using biological standard methods led to a deeper understanding of the iron homeostasis of neurons ensheathed by a perineuronal net [29].

3.3. Neurobiology – Parkinson's disease

Patients suffering from Parkinson's disease have an up to three-fold higher iron concentration in the brain region substantia nigra [30]. The reason for this pathological accumulation, obviously an altered iron homeostasis, is unknown. Presumably, the iron accumulating molecular structures, e.g. ferritin in glial cells and in particular the pigment neuromelanin (NM) in neurons, play a fundamental role in the etiology of Parkinson's disease. Neuromelanin
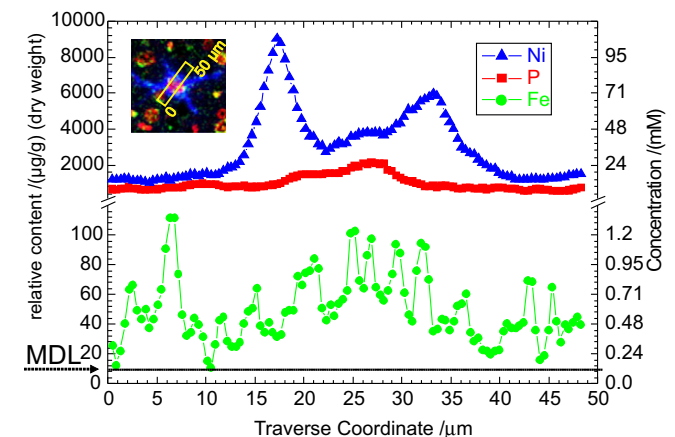
Fig. 2. Analysis of the affinity of perineuronal nets to iron, described by the affinity constant k_D, (Wistar rat cortex). The dependency of the Fe-concentration bound to the PNN upon the applied Fe loading, c, follows the Michaelis–Menten equation for enzyme kinetics. The parameter c_{ph} was introduced to account for the physiologic iron concentration which was determined close to the minimum detection limit.

Fig. 3. Elemental profiles of P (red), Ni (blue) and Fe (green) extracted from a 50 μm long traverse across the soma of a perineuronal net ensheathed neuron. The inlay shows the corresponding three element map. The nickel labeling of the perineuronal net (PNN) enables the identification of PNN-neurons to extract intracellular iron concentrations. The Fe-profile shows that there is no influence from the Ni-labeling, because the distributions of these two elements are not correlated. The minimum detection limit (MDL) is well below the physiological intracellular iron concentration. (For interpretation of the references in color in this figure legend, the reader is referred to the web version of this article.)
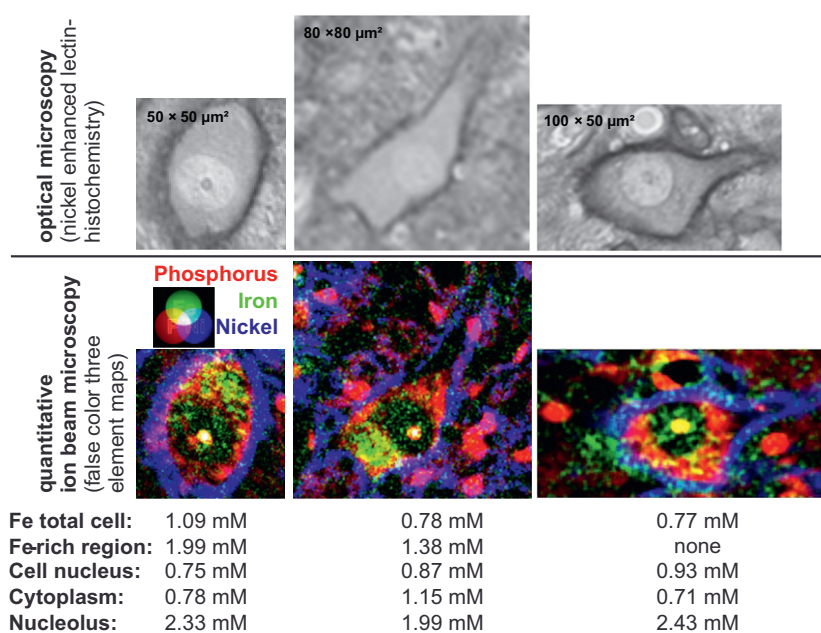
Fe total cell:	1.09 mM	0.78 mM	0.77 mM
Fe-rich region:	1.99 mM	1.38 mM	none
Cell nucleus:	0.75 mM	0.87 mM	0.93 mM
Cytoplasm:	0.78 mM	1.15 mM	0.71 mM
Nucleolus:	2.33 mM	1.99 mM	2.43 mM

Fig. 4. Top: Optical microscopy of rat neurons with a perineuronal net. Bottom: Three element map representation (P: red, Ni: blue, Fe: green) of the neurons shown above. The maps provide quantitative information on the elemental concentrations from which the iron concentrations of several regions of interest are presented. (For interpretation of the references in color in this figure legend, the reader is referred to the web version of this article.)

is a dark-colored intracellular pigment appearing in a specific population of neurons (dopaminergic and noradrenergic) in senescent mammals predominantly in the substantia nigra pars compacta and in the locus coeruleus. It is formed by oxidation of catecholamines. In recent years, there is increasing interest in the role of neuromelanin because of a hypothesized link between this pigment and the cell death of neuromelanin-containing neurons in Parkinson's disease (PD), due to metal ion binding of neuromelanin and a consequential generation of free radicals [31]. The biology, i.e. the structure, synthesis, physiology and its role in the neuron is still not entirely understood. It is likely that, similar to other types of melanins, neuromelanin acts as a protector against free radicals by inactivating or chelating free toxic metal ions (e.g. manganese, iron, copper). However, in the case of redox-active metal ion excess, and this is controversially discussed, neuromelanin could potentiate the free radical production due to a reduced binding capacity. The role of neuromelanin in the pathology of PD is therefore an actual focus in neuroscience [32].

To our best knowledge, there is no comparative study of Parkinsonian cases versus control that performed an in situ analysis of the concentration of metal ions bound to neuromelanin. Therefore, we launched a study analyzing the neurons in the substantia nigra of six cases with different severity of Parkinson's disease and of six control cases without any history of neuropsychiatric disorders or mental impairment. The results show equal levels of iron bound to NM for both, Parkinsonian and control cases. However, there was a significant decrease in calcium and increase in potassium content for the Parkinsonian cases. No significant change in the content of other trace elements (Cu, Zn) was observed [20]. We also performed ultrastructural analysis of the elemental distribution in NM with a lateral resolution of less than 0.5 μm. Our findings suggest that the metal elements are enriched in small dense granules [33].

3.4. Radiobiology

The irradiation platform for single cell irradiation has undergone a stepwise development. Initially the design was restricted to fit into the old target chamber which had no appropriate means to do targeted irradiation. First radiobiological experiments on primary human fibroblasts and HeLa-cells were done with patterned irradiation using 2 MeV protons and He-ions. The induction of DNA double strand breaks (DSB) and the expression of the heat shock protein HSP70 as a marker for cell protective activities have been studied [11]. The induced DNA DSB patterns showed for He-ions the anticipated localized damage near the ion tracks, whereby for proton irradiation the DSB foci were much less correlated with the proton tracks. This result leads to the assumption that for the proton irradiation the DNA damage is mediated via secondary effects such as proton induced reactive oxygen species (ROS). Proton irradiation at low temperatures (<10 °C) showed more localized damage, which can be explained by a reduced diffusion of the induced ROS.

Proton irradiated fibroblasts showed an increased HSP70 expression in the cytoplasm in aggregated forms. This is in contrast to heat shock where HSP70 expression is increased in the nucleus. Furthermore, the cytoplasmic expression can also be observed in non-irradiated bystander cells. However, further studies are needed to elucidate the involved mechanisms.

With the new sample chamber installed in 2007 the irradiation platform was redesigned and a major software development was undertaken to provide fast targeted single cell irradiation [34]. Thereby the cell recognition does not need fluorescence techniques. The cell recognition software identifies cell nuclei and fiducial markers from a phase contrast image taken with a Zeiss Axiovert 25 CFL inverted microscope offline in the cell lab prior transfer to the irradiation stage. The fiducial markers, identified through the online microscope, are taken as reference points for the Petri dish position. The cellular target coordinates are then transformed into beam position coordinates for irradiation. Recently we achieved routine irradiation of cell nuclei (Fig. 5). An average handling time of less than 4 min per Petri dish including microscopy, cell and target identification, medium removal, irradiation and medium restoration, allows irradiation of up to 20,000 individual cells per hour. Targeting of the cytoplasm is realized by an appropriate offset from the nucleus position along the long axis of the cell.
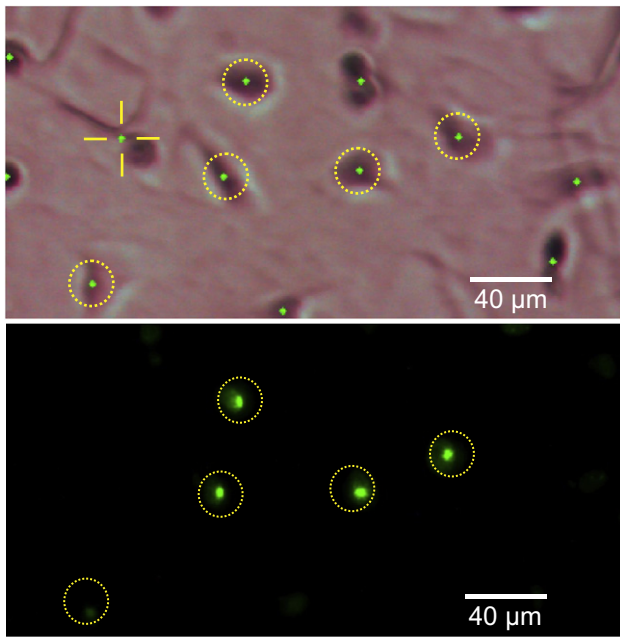
Fig. 5. Top: Phase contrast image of Ea.hy 926 cells on polypropylene foil with identified target position (dot in cell nucleus). The cross indicates a false positive hit. Circles indicate cells with double strand breaks after irradiation with 200 protons of 2.25 MeV and 16 min incubation time (Bottom: γH2AX staining of double strand breaks).

3.5. Confined cell growth

In order to achieve confined cell growth we applied the technique of proton beam writing (PBW) on the biocompatible but cell repellent hydrogel agar which is coated on a cell adhesive substrate. Agar is a polysaccharide, which is non-soluble in water, however, sensitive to proton irradiation. The proton beam transforms the polysaccharide into water-soluble oligo- or monosaccharides which are easily washed away prior cell seeding. Thus, the substrate resurfaces exact in the shape as defined by PBW. Fig. 6 shows an example which demonstrates that the cells exclusively grow on the agar free regions.

The ability to create arbitrary shaped patterns with high precision down to the sub-micrometer level assures the technologically easy application to different arrangement. The technique was first applied in a pilot study in context with low dose ion irradiation to study cell-cell communication (via direct cell contact or medium-borne signaling pathways) by the creation of separated subcultures of cells with and without small bridges. A further application was the creation of attachment sites for individual neurons and interconnecting micron-sized pathways to allow neurite outgrowth. The goal is to create defined neuronal circuits [35].

Fig. 6. Confined cell growth in a Petri dish coated with the cell repellent hydrogel agar. The agar layer was selectively dissolved after proton beam writing exhibiting the "Cell" shape as area of exclusive cell adhesion. Fluorescence diacetate stained primary human fibroblast cells after 3 days in culture.

4. Future developments

The development of a 5 keV energy resolution detection system for STIM, based on a compact Amptek A250 preamplifier design directly connected to the detector improved the STIM contrast considerably (for details see [19]). It enables the imaging of the density contrasts of sub-50 nm cellular structures or the analysis of intracellular distributions of nanoparticles that are promising candidates for drug delivery systems. The higher STIM contrast is equally important for STIM-tomography of single cells which enables the 3D analysis with a spatial resolution below 100 nm. The major problem of a complicate preparation of free-standing single cells for tomography measurements has been avoided by the development of limited angle tomography [18]. The combination STIM/PIXE tomography will enhance even more the analytical capabilities for the study of drug delivery systems or for the analysis of elemental concentrations in samples of irregular shape, e.g. in the sensilla of the Drosophila's antenna [36].

Another approach of 3D elemental analysis is PIXE-stacking of individual element maps of a series of thin sections to assess the third dimension of a sample. The high sample throughput needed for such a 3D PIXE analysis became possible with higher beam current densities (>1 nA/μm^2) that are now achievable. With the octupole stigmator lens that is currently under development, we expect a further increase in beam current density by a factor of two to three.

This will consequently reduce the run time for PIXE maps down to a few minutes without a compromise in detection limit or resolution. A first application of the PIXE-stacking will be the 3D elemental analysis of an artherosclerotic coronar vessel (mouse model) and of a Drosophila's head. Especially the 3D mapping of the fly brain is a promising approach to compile an elemental brain atlas. With a large solid angle detector [37] this goal can even be pursuit to mouse or rat brain.

Acknowledgements

References

[1] J. Cookson, A. Ferguson, F. Pilling, J. Rad. Nucl. Chem. 12 (1972) 39.
[2] T. Osipowicz, M. Breese, Nucl. Instr. Meth. B 260 (2007) vii.
[3] I. Rajta, Á.Z. Kiss, Z. Kertész, Z. Szikszai, A. Simon, Nucl. Instr. Meth. B 267 (2009) v.
[4] A. Bigelow, G. Garty, T. Funayama, G. Randers-Pehrson, D. Brenner, C. Geard, J. Radiat. Res. 50 (2009) A21–A28.
[5] G. Dollinger, V. Hable, A. Hauptner, R. Krücken, P. Reichart, A.A. Friedl, G. Drexler, T. Cremer, S. Dietzel, Nucl. Instr. Meth. B 231 (2005) 195.
[6] M. Heiss, B.E. Fischer, B. Jakob, C. Fournier, G. Becker, G. Taucher-Scholz, Radiat. Res. 165 (2006) 231.
[7] Ph. Barberet, A. Balana, S. Incerti, C. Michelet-Habchi, Ph. Moretto, Th. Pouthier, Rev. Sci. Instr. 76 (2005) 15101.
[8] K. Greif, W. Beverung, F. Langner, D. Frankenberg, A. Gellhaus, F. Banaz-Yasar, Radiat. Prot. Dosim. 122 (2006) 313.
[9] T. Funayama, S. Wada, Y. Yokota, K. Fukamoto, T. Sakashita, M. Taguchi, T. Kakizaki, N. Hamada, M. Suzuki, Y. Furusawa, H. Watanabe, K. Kiguchi, K. Kiguchi, Y. Kobayashi, J. Radiat. Res. 49 (2008) 71.

[10] K.J. Kirkby, G.W. Grime, R.P. Webb, N.F. Kirkby, M. Folkard, K. Prise, B. Vojnovic, Nucl. Instr. Meth. B 260 (2007) 97.
[11] A. Fiedler, T. Reinert, J. Tanner, T. Butz, Nucl. Instr. Meth. B 260 (2007) 169.
[12] G. Tylko, J. Mesjasz-Przybylowicz, W.J. Przybylowicz, Nucl. Instr. Meth. B 260 (2007) 141.
[13] F. Watt, X. Chen, A. de Baysic Vera, C.C.N. Udalagama, R. Minqin, J. van Kan, A. Bettiol, Nucl. Instr. Meth. B (this proceedings).
[14] D.J.W. Mous, R.G. Haitsma, T. Butz, R.H. Flagmeyer, D. Lehmann, J. Vogt, Nucl. Instr. Meth. B 130 (1997) 31.
[15] A.D. Dymnikov, D.N. Jamieson, G.J.F. Legge, Nucl. Instr. Meth. B 104 (1995) 64.
[16] T. Reinert, D. Spemann, M. Morawski, T. Arendt, Nucl. Instr. Meth. B 249 (2006) 734.
[17] M. Rothermel, T. Butz, T. Reinert, Nucl. Instr. Meth. B 267 (2009) 2017.
[18] T. Andrea, M. Rothermel, R. Werner, T. Butz, T. Reinert, Nucl. Instr. Meth. B 268 (2010) 1884.
[19] D. Spemann, T. Reinert, J. Vogt, T. Andrea, N. Barapatre, R. Feder, A.M. Jakob, N. Liebing, C. Meinecke, F. Menzel, M. Rothermel, T. Butz, Nucl. Instr. Meth. B (this proceedings).
[20] N. Barapatre, M. Morawski, T. Butz, T. Reinert, Nucl. Instr. Meth. B 268 (2010) 2156.
[21] J. Wang, P. Guo, X. Li, J. Zhu, T. Reinert, J. Heitmann, D. Spemann, J. Vogt, R.-H. Flagmeyer, T. Butz, Nucl. Instr. Meth. B 161 (2000) 830.
[22] P. Guo, J. Wang, X. Li, J. Zhu, T. Reinert, J. Heitmann, D. Spemann, J. Vogt, R.-H. Flagmeyer, T. Butz, Nucl. Instr. Meth. B 161 (2000) 801.
[23] T. Reinert, U. Reibetanz, J. Vogt, T. Butz, A. Werner, W. Gründer, Nucl. Instr. Meth. B 181 (2001) 511.
[24] M. Morawski, S. Pavlica, G. Seeger, J. Grosche, E. Kouznetsova, R. Schliebs, G. Brückner, T. Arendt, Neurobiol. Aging 31 (2010) 1254.
[25] M. Morawski, G. Brückner, C. Jäger, G. Seeger, T. Arendt, Neuroscience 169 (2010) 1347.
[26] T. Reinert, M. Morawski, T. Arendt, T. Butz, Nucl. Instr. Meth. B 210 (2003) 395.
[27] M. Morawski, T. Reinert, C. Meinecke, T. Arendt, T. Butz, Nucl. Instr. Meth. B 231 (2005) 229.
[28] A. Fiedler, T. Reinert, M. Morawski, G. Brückner, T. Arendt, T. Butz, Nucl. Instr. Meth. B 260 (2007) 153.
[29] A. Fiedler, Eisen und Eisenproteine in Neuronen mit perineuronalem Netz, PhD-Thesis , Universität Leipzig, 2008.
[30] M.E. Götz, K. Double, M. Gerlach, M.B.H. Youdim, P. Riederer, Ann. N. Y. Acad. Sci. 1012 (2004) 193.
[31] L. Zecca, L. Casella, A. Albertini, C. Bellei, F.A. Zucca, M. Engelen, A. Zadlo, G. Szewczyk, M. Zareba, T. Sarna, J. Neurochem. 106 (2008) 1866.
[32] H. Fedorow, F. Tribl, G. Halliday, M. Gerlach, P. Riederer, K.L. Double, Prog. Neurobiol. 75 (2005) 109.
[33] T. Reinert, A. Fiedler, M. Morawski, T. Arendt, Nucl. Instr. Meth. B 260 (2007) 227.
[34] T. Koal, T. Butz, T. Reinert, J. Rad. Res. 50 (2009) 108.
[35] W. Larisch, T. Koal, R. Werner, M. Hohlweg, T. Reinert, T. Butz, Nucl. Instr. Meth. B (this proceedings).
[36] A. Reinert, N. Barapatre, T. Reinert, S. Sachse, Nucl. Instr. Meth. B (this proceedings).
[37] C. Ryan, Nucl. Instr. Meth. B (this proceedings).

Appendix E
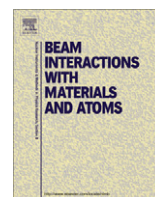
Materials analysis and modification at LIPSION – Present state and future developments

D. Spemann [a,*], T. Reinert [a,b], J. Vogt [a], T. Andrea [a], N. Barapatre [a], R. Feder [a], A.M. Jakob [a], N. Liebing [c], Ch. Meinecke [a], F. Menzel [a], M. Rothermel [a], T. Butz [a]

[a] Universität Leipzig, Institut für Experimentelle Physik II, Linnéstr. 5, 04103 Leipzig, Germany
[b] University of North Texas, Department of Physics, 1155 Union Circle, Denton, TX 76203, USA
[c] Physikalisch-Technische Bundesanstalt, Department 2.52, Bundesallee 100, 38116 Braunschweig, Germany

ARTICLE INFO

ABSTRACT

The LIPSION laboratory which became operational in 1998 has been improved in numerous ways since that time in order to enhance its capabilities in materials analysis and modification as well as life sciences. This paper summarizes the modifications and improvements made and gives a description of the present state with a detailed list of the technical specifications. The capabilities of LIPSION are illustrated by selected examples from our recent research in materials sciences. Finally a prospect on future developments is given, i.e. the new octupole correction lens and the low noise in-vacuum preamplifier which are expected to further increase the performance of the Leipzig ion nanoprobe.

© 2011 Elsevier B.V. All rights reserved.

1. Introduction

Nuclear microprobes (NMPs) are versatile tools that offer a variety of powerful analytical techniques for materials analysis and modification in combination with high spatial resolution [1]. The applications of NMPs in material sciences include quantitative elemental imaging [2,3], the analysis of the structure and defects in crystalline materials [4], the investigation of the electronic properties of semiconductors [5] as well as the modification of a variety of materials in order to create structures [6] or alter physical properties [7]. In some cases, a series of two-dimensional images can even be combined to form three-dimensional tomographic images [8]. This broad range of applications already indicates that nuclear microprobes are far away from being "push-button devices", but are still quite experimental. They are constantly improved to enhance their technical capabilities and to keep up with the demands of today's material sciences. Consequently, the high-energy ion nanoprobe LIPSION which has been operational since 1998 [9,10] has undergone numerous improvements since that time as will be shown here.

This paper describes the present state and experimental capabilities of LIPSION illustrated with some examples of our recent research activities in material sciences. Furthermore, a prospect on future developments is given.

2. Modifications and improvements at LIPSION

The LIPSION laboratory was built completely from scratch. With its special basements, the very stable air-conditioning system, the high brightness 3.5 MV Singletron accelerator and the nanoprobe from MARC Melbourne this laboratory has all ingredients for high-performance and high-resolution microprobe work [9]. Starting operation in 1998, it took a few years to become in-depth familiar with the system, to explore its analytical capabilities and to reveal the weak points every system has in order to make improvements (see Fig. 1). The first major one was the installation of an active compensation of stray magnetic fields [11] in 2002 – the first and up to now only system of this kind used on nuclear microprobes. The compensation significantly reduces the detrimental influence of stray magnetic fields (originating mainly from the tram nearby) on the spatial resolution by keeping constant the magnetic field in the volume that contains the lens system of the microprobe. The upgrade to microDAS in 2005 together with a software developed to scan arbitrary shapes [12] expanded the capabilities of LIPSION by the field of proton beam writing (PBW) [13]. The installation of a new multi-purpose target chamber in 2007 represents another significant modification [14]. It is equipped with a computer-controlled in-vacuum 7-axis stage including a 2-axis eucentric goniometer. The chamber has a removable hood that allows an easy installation of an exit nozzle for external beam applications. Several modifications and improvements followed the new chamber. These are summarized as well in Fig. 1.
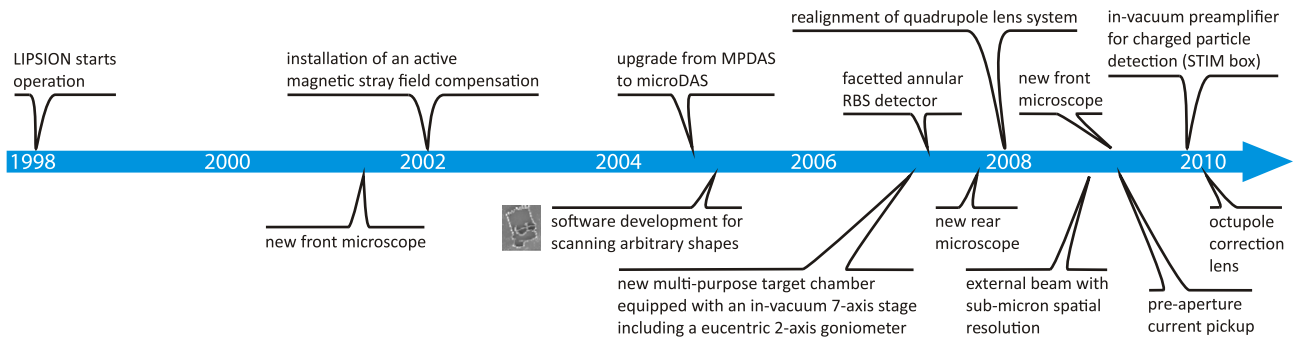
Fig. 1. Modification and improvements of the LIPSION system between 1998 and 2010.

3. Present state and analytical capabilities

A schematic view of the LIPSION laboratory in its present state is shown in Fig. 2 where the main components of the system are labeled. The experimental techniques routinely available are Particle Induced X-ray Emission (PIXE), Rutherford Backscattering Spectrometry (RBS), Secondary Electron detection (SE), Ion Beam Induced Charge (IBIC), and Scanning Transmission Ion Microscopy (STIM). These techniques can be combined with ion channeling using the eucentric goniometer. In addition, PIXE and STIM can be used to obtain 3D-tomographic images by taking a series of 2D-images under different rotation angles. Furthermore, Particle Induced γ-ray Emission (PIGE) can be made available using a dedicated PIGE detector flange.

The sample can be viewed even under ion exposure with a front and rear microscope, respectively. Furthermore, the new front microscope with its large working distance will allow an electrode to be re-installed in front of the RBS detector opposite to the sample that can be biased for secondary electron suppression. Such a system is very important for a reliable measurement of the beam current on target and was already used at LIPSION until 2002 when the front microscope installed at that time made the system ineffective due to geometrical constraints. At present, the accumulated beam charge is calculated from the collected RBS yield.

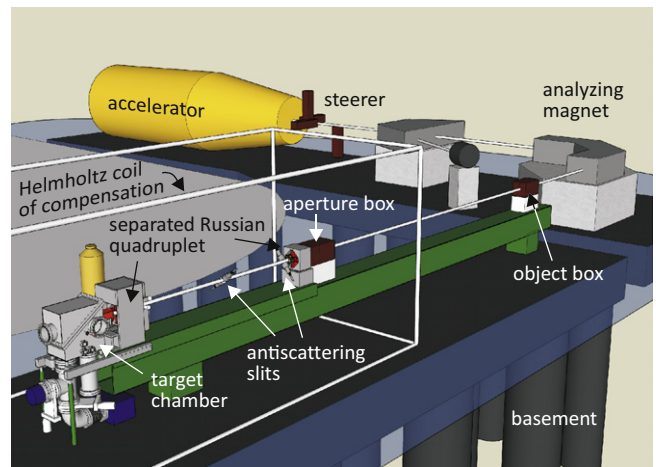More technical details of the system are listed in Table 1.

Fig. 2. Schematic view of the LIPSION laboratory.

Today's materials analysis and modification often requires spatial resolutions well below one micron. This can easily be achieved when using low current techniques like STIM or IBIC (neglecting effects like charge diffusion that limit the spatial resolution attainable) or when exposing photoresists in PBW applications. Elemental

Table 1
Technical details of the Leipzig ion nanoprobe in its present state (July 2010).

Beam parameters and ion optics	
Accelerator	3.5 MV Singletron from HVE
Beams	H^+, H_2^+, He^+
Object box	Circular diaphragms + micro-slits; diaphragms with diameters of 5, 10, 20, 30, 50, 100, 200, 300 μm
Aperture box	Circular diaphragms with diameters of 10, 20, 50, 100, 150, 200, 300, 500 μm; pre-aperture current measurement [15]
Focussing system	Separated Russian quadruplet from MARC Melbourne, symmetric demagnification of $D_{x,y} \approx 130$; octupole correction lens in front of third quadrupole (Q3)
Compensation of stray magnetic fields	Active in x-, y-, z-direction using Helmholtz coils from true DC to several kHz, remaining stray field fluctuations ± 10 nT [4]
Beam scanning	Electromagnetic, coils with N = 1–256 turns between last quadrupole lens (Q4) and target chamber, maximum scan size: 3.2 × 3.2 mm²; Murray MA 534 PT 100 transconductance amplifier
Target chamber and its components	
Target chamber	Multi-purpose chamber with detachable hood for external beam applications [6]
Sample stage	in-vacuum computer-controlled 7-axis stage including a 2-axis eucentric goniometer (x, y, z, φ, θ, x', y')
Microscopes	Custom made front and rear microscopes from Thalheim Spezialoptik (Germany)
Charge measurement	Direct pickup from isolated sample holder and/or from a carbon-made faraday cup; no secondary electron suppression at present
External beam	200 nm Si_3N_4 exit window, 2 × 2 mm² maximum scan size
Detectors and data acquisition	
PIXE-detector	Canberrra GUL0110 high-purity Germanium (since 2010), 95 mm² active area, energy resolution 144 eV at 5.9 keV, retractable with sealed bellow, solid angle up to 150 msr
RBS-detector	Canberra CD-Leipzig1–300 facetted annular PIPS detector, energy resolution 20 keV for 2.25 MeV protons, total solid angle 100 msr (4 × 16.7 msr + 1 × 33.0 msr)
STIM-detector	Hamamatsu S1223 PIN diode, in-vacuum preamplifier based on Amptek A250, energy resolution 5.4 keV for 2.25 MeV protons
SE-detector	Amptektron MD-502 channeltron from Amptek
Data acquisition	microDAS from MARC Melbourne

Table 2
Typical beam spot sizes and currents for different object and aperture diaphragm settings. Details on these measurements can be found in [18], [19], [17].

Object diaphragm (μm)	Aperture diaphragm (μm)	Beam spot size (μm)	Beam current
μ–slits	10	0.04[*]	1–2 fA
20	200	0.27[**]	10 pA
50	200	0.50[**]	120 pA
100	300	0.80	1.0 nA
200	300	1.5	4.5 nA
200	500	1.6	8.3 nA
300	500	2.2	17 nA

[*] Due to the characteristics of the standard used, this value was measured as beam spot profile in one dimension only [18].
[**] These values were measured before the realignment of the lens system [19].

analysis with submicron spatial resolution, however, can still be quite challenging depending on the required beam current which might range from 10 pA for the determination of the matrix composition to several nA for trace element analysis, e.g. in geological samples [16].

The LIPSION nanoprobe has been designed for high spatial resolution with a high demagnification of $D_{x,y} \approx 130$ of the lens system which, however, is also characterized by very high spherical aberration coefficients [9]. Therefore, not only the alignment of the quadrupole lenses itself, but also the alignment of the aperture diaphragm with respect to the optical axis of the lens system needs to be very precise in order to keep the beam spot sizes small when using larger apertures. This precise alignment could be achieved in 2008 by a realignment of the lens system [17] which significantly improved the spatial resolution achievable at higher beam currents. Typical beam spots sizes at LIPSION together with the diaphragm settings and beam currents are listed in Table 2.

4. Examples from materials sciences at LIPSION

One main application in material sciences at LIPSION is the elemental analysis of optoelectronic materials [20] and devices [21] as well as the trace element analysis of carbon-based materials in the sub-ppm region [22]. In addition, the electronic properties of commercially available polycrystalline Si solar cells were recently characterized with IBIC using a new low noise in-vacuum IBIC setup [23].

With the eucentric goniometer installed 2007 and a software developed 2008 automated angular scans can be performed in order to align a sample's crystallographic axis to the beam axis. Fig. 3(a) shows a polar plot of the RBS yield of 2 MeV He$^+$ ions on (1 0 0) silicon for an angular scan around the horizontal axis at a tilt
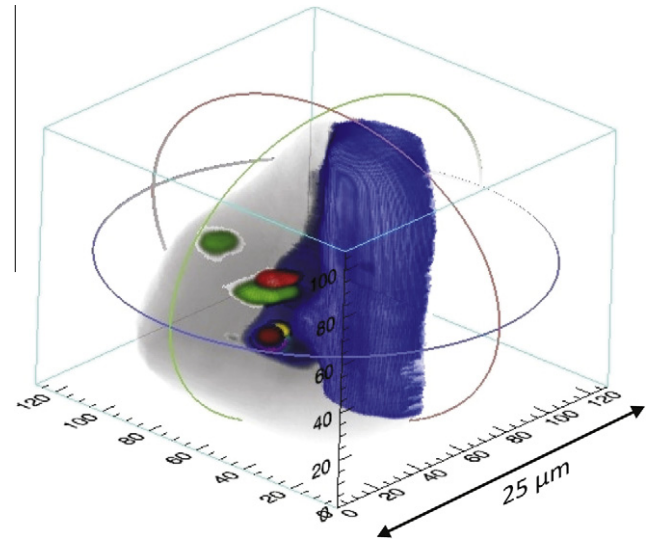

Fig. 4. PIXE-tomogram of a phantom containing ZnO (blue), Fe$_2$O$_3$ (red), Co$_3$O$_4$ (green), SiO$_2$ (yellow), K$_2$Cr$_2$O$_7$ (magenta) and glue (grey). The initial 2D-images were recorded using 2.25 MeV protons. The orbits shown in the picture allow a real time investigation of the tomogram by mouse movement in the dedicated tomography software (For interpretation of the references to color in this figure legend, the reader is referred to the web version of this paper.)

angle of $\theta = 5°$. From this angular scan, the φ and θ position of the (1 0 0) axis can be determined by triangulation (see right plot in Fig. 3(a)). The normalized minimum yield achieved in these measurements was $\chi_{min} = 4\%$ which is a good result when taking into consideration that a focussed beam with a convergence angle of 0.15° was used instead of a well collimated one. With this setup, one of the first applications of Channeling Contrast Microscopy (CCM) was to gain some experience on the influence of ion beam induced damage on the channeled backscattering yield, an important issue that needs to be taken into account in CCM analysis. Similar to the study reported in [24], an area of $54 \times 54 \ \mu m^2$ of silicon was irradiated with 2 MeV He$^+$ ions along the (1 0 0) axis with a fluence of 1.0×10^{18} He$^+$/cm^2 and scanned afterwards using CCM (see Fig. 3(b)). It was observed that χ_{min} increased only from 4.0% to 4.7% in the central region, whereas at the edges of the $54 \times 54 \ \mu m^2$ scan χ_{min} increased to 33%. As has been first correctly explained by Dooley et al. in 1992 [24], this is caused by a swelling of the crystal due to ion beam induced defects (one should note that the defects themselves are mainly produced near the end of range of the He$^+$ ions and are therefore invisible in the backscattering
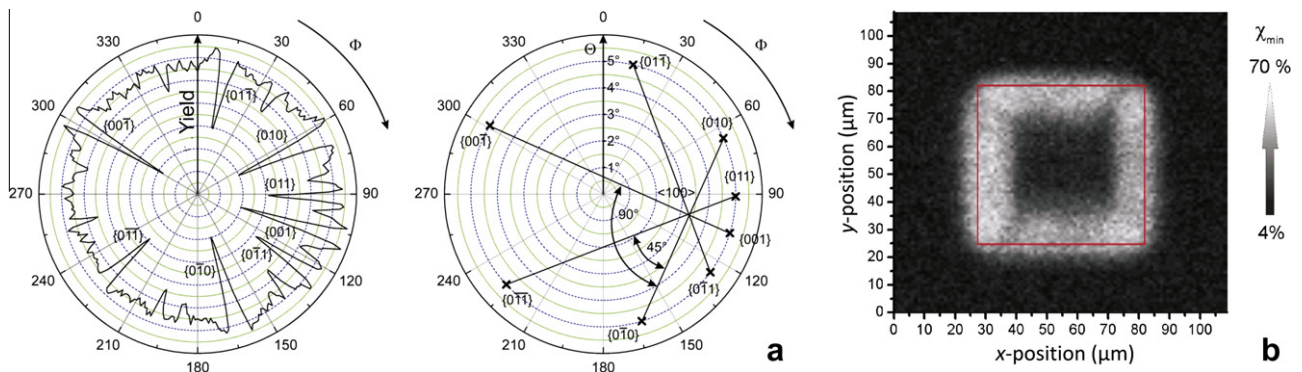

Fig. 3. 2 MeV He$^+$ ion channeling on (100) silicon: (a) polar plot of the RBS yield during an automated φ angular scan at $\theta = 5°$ tilt angle (left) and determination of the angular position of the crystal axis by triangulation (right); (b) CCM map of a $54 \times 54 \ \mu m^2$ sized region irradiated with a fluence of 1×10^{18} He$^+$/cm^2 (region within square) that shows a reduced channeling at the edges of this region due to a tilt of the crystal planes.
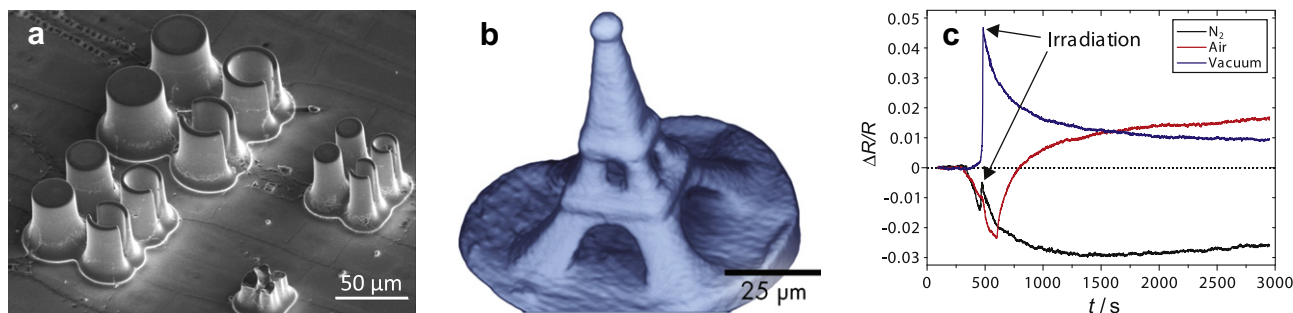
Fig. 5. Examples of materials modification at LIPSION: (a) creation of structures in p-type InP by PBW using 2.25 MeV protons and electrochemical etching in a HF solution; (b) Eiffel tower sculpted in PMMA resist and imaged using STIM-tomography; (c) in situ measurement of the influence of 2.25 MeV proton irradiation on the electrical resistivity of a micrometer-sized multi-graphene sample under different atmospheres using an external beam.
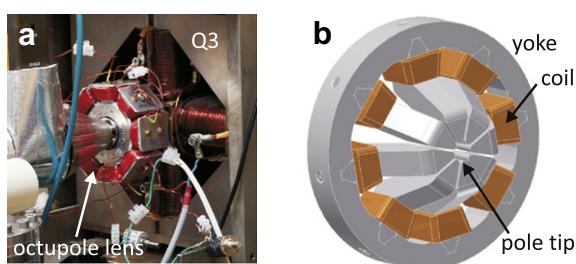

Fig. 6. Octupole correction lens in front of quadrupole Q3: (a) optical image of the first test setup; (b) schematic drawing of the octupole lens that is currently being manufactured using wire cutting.

yield at sufficiently low fluences). This swelling leads to a tilt of the crystal planes along these edges which results in a misalignment between the $(1\,0\,0)$ axis and the ion beam and consequently to poor channeling in these areas. This can be verified by tilting the sample by a small angle which re-establishes a good channeling in the corresponding edge.

PIXE-tomography (PIXE-T) still is a big challenge in elemental analysis and requires a substantial effort in data acquisition and processing. It also requires a high performance and stability of the microprobe system over hours which is one of the characteristics of LIPSION. Fig. 4 shows a tomogram of a phantom prepared from different oxidic compounds that represents some of the first results of PIXE-T obtained with 2.25 MeV protons at the Leipzig ion nanoprobe [25].

The applications in materials modification can be subdivided in PBW where micro- and nanostructures are created and the modification of electronic and magnetic properties of samples. PBW has been used to create structures in a variety of photoresists [26,27] as well as in different semiconductors [26,28,29] (see Fig. 5(a)). The structures in resist materials can be transferred into metal

structures by using electroplating if necessary [26]. Photoresists can also be prepared as cylinders with diameters comparable to the ion range and below. The irradiation of these cylinders under different rotational angles and perpendicular to the cylinder's axis allows the creation of complex 3D-structures – a process that can be described as proton beam sculpting [30] (see Fig. 5(b)).

In addition, the interaction of ions with matter, i.e. the breakage of chemical bonds and the displacement of atoms allows to modify the physical properties of samples. One example that has been studied in detail at LIPSION and attracted much interest is the creation of magnetic order in carbon [7]. The new target chamber with its ample space and numerous electric feedthroughs has opened up new possibilities for the in situ study of the magneto-resistance [31] as well as the electrical resistance of carbon-based materials under ion irradiation (see Fig. 5(c)).

5. Future developments

There are several ways to improve the performance and technical capabilities of a microprobe. Increasing the spatial resolution at a given beam current is a challenging task, but equally vital to keep up with the demands of today's material sciences. At LIPSION increasing the spatial resolution at constant beam current can be achieved by using smaller object but larger aperture diaphragms. After the realigment of the lens system in 2008 grid shadow measurements revealed a parasitic octupole contribution to which quadrupole lens Q3 is most susceptible to. Therefore, the anti-skew quadrupole lens in front of Q3 was replaced by an octupole stigmator lens. This allows to correct for the main octupole contribution as well, because it provides both a quadrupole as well as a octupole field of adjustable strength [32]. First tests with a comparably simple design (see Fig. 6(a)) showed that the field strength is not yet sufficient. Therefore, a more sophisticated lens design with significantly smaller gaps between pole tips and beam axis was developed and is currently being manufactured using wire cutting (see
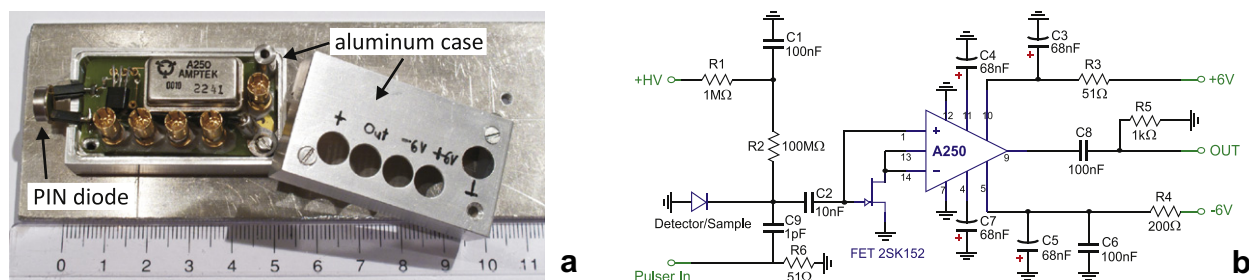

Fig. 7. Low noise in-vacuum preamplifier based on an Amptek A250: (a) photography of the preamplifier together with a PIN diode. The electronics is mounted in an aluminum case that provides shielding against electromagnetic stray fields. The scale is in cm; (b) circuit diagram of the preamplifier.

Fig. 6(b)). With this octupole stigmator in operation we hope to fully exploit the capabilities of the quadrupole lens system.

An improvement of the analytical capabilities can also be achieved by improving the performance of the detectors, e.g. the energy resolution of charged particle detectors. For this purpose, an in-vacuum preamplifier based on an Amptek A250 that was initially developed for IBIC measurements on solar cells has been adapted to be used with standard charged particle detectors (see Fig. 7). The complete setup consisting of a Hamamatsu S1223 PIN diode, the preamplifier and an Ortec 572 pulse shaper is characterized by an excellent signal-to-noise-ratio and is already in use for STIM measurements where it provides an energy resolution of $\delta E = 5.4$ keV for 2.25 MeV protons. It is planned to use these pre-amplifiers for the facetted RBS detector as well.

6. Conclusion

Over the years, the Leipzig ion nanoprobe LIPSION has been improved in numerous ways in order to enhance its capabilities in materials analysis and modification. It is used for a broad range of applications here and in life sciences as well [33] which, however, does not come without compromises as there is only one nanoprobe beamline available that cannot be dedicated to one specific application only. Nevertheless, LIPSION offers a state-of-the-art performance that makes it a valuable tool in material sciences.

Acknowledgements

References

[1] M.B.H. Breese, P.J.C. King, Materials Analysis using a Nuclear Microprobe, John Wiley & Sons, Inc., New York, 1996.
[2] C.G. Ryan, Nucl. Instr. Meth. B 181 (2001) 170.
[3] C.G. Ryan, R. Kirkham, D.P. Siddons, P.A. Dunn, J.S. Laird, A. Kuczewski, G. Moorhead, G. De Geronimo, P. Davey, M. Jensen, D.J. Paterson, M.D. de Jonge, D.L. Howard, R.M. Hough, Nucl. Instr. Meth. B 268 (2010) 1899.
[4] M.B.H. Breese, E.J. Teo, L. Huang, Nucl. Instr. Meth. B 260 (2007) 288.
[5] M.B.H. Breese, E. Vittone, G. Vizkelethy, P.J. Sellin, Nucl. Instr. Meth. B 264 (2007) 345.
[6] F. Watt, M.B.H. Breese, A.A. Bettiol, J.A. van Kan, Materials Today 10 (2007) 20.
[7] H. Ohldag, T. Tyliszczak, R. Höhne, D. Spemann, P. Esquinazi, M. Ungureanu, T. Butz, Phys. Rev. Lett. 98 (2007) 187204.
[8] A. Sakellariou, D.N. Jamieson, G.J.F. Legge, Nucl. Instr. Meth. B 181 (2001) 211.
[9] T. Butz, R.-H. Flagmeyer, J. Heitmann, D.N. Jamieson, G.J.F. Legge, D. Lehmann, U. Reibetanz, T. Reinert, A. Saint, D. Spemann, R. Szymanski, W. Tröger, J. Vogt, J. Zhu, Nucl. Instr. Meth. B 161–163 (2000) 323.
[10] J. Vogt, R.-H. Flagmeyer, J. Heitmann, D. Lehmann, T. Reinert, St. Jankuhn, D. Spemann, W. Tröger, T. Butz, Mikrochim. Acta 133 (2000) 105.
[11] D. Spemann, T. Reinert, J. Vogt, J. Wassermann, T. Butz, Nucl. Instr. Meth. B 210 (2003) 79.
[12] Silvio Petriconi, On the proton beam writing and magnetic characterisation of microstructures in highly oriented pyrolytic graphite. Diploma thesis, Universität Leipzig (2006).
[13] F. Menzel, D. Spemann, S. Petriconi, J. Lenzner, T. Butz, Nucl. Instr. Meth. B 250 (2006) 66.
[14] Ch. Nilsson, S. Petriconi, T. Reinert, T. Butz, Nucl. Instr. Meth. B 260 (2007) 71.
[15] N. Barapatre, M. Morawski, T. Butz, T. Reinert, Nucl. Instr. Meth. B 268 (2010) 2156.
[16] C.G. Ryan, This proceedings.
[17] M. Rothermel, T. Butz, T. Reinert, Nucl. Instr. Meth. B 267 (2009) 2017.
[18] D. Spemann, T. Reinert, J. Vogt, D. Dobrev, T. Butz, Nucl. Instr. Meth. B 190 (2002) 312.
[19] T. Reinert, M. Morawski, D. Spemann, Th. Arendt, Nucl. Instr. Meth. B 249 (2006) 734.
[20] Ch. Meinecke, J. Vogt, J. Bauer, V. Gottschalch, T. Butz, Nucl. Instr. Meth. B 260 (2007) 314.
[21] D. Spemann, K. Otte, M. Lorenz, T. Butz, Nucl. Instr. Meth. B 231 (2005) 440.
[22] D. Spemann, P. Esquinazi, R. Höhne, A. Setzer, M. Diaconu, H. Schmidt, T. Butz, Nucl. Instr. Meth. B 231 (2005) 433.
[23] A.M. Jakob, D. Spemann, R. Thies, J. Barzola-Quiquia, J. Vogt, T. Butz. This proceedings.
[24] S.P. Dooley, D.N. Jamieson, Nucl. Instr. Meth. B 66 (1992) 369.
[25] M. Rothermel, T. Reinert, T. Andrea, T. Butz, Nucl. Instr. Meth. B 268 (2010) 2001.
[26] F. Menzel, D. Spemann, S. Petriconi, J. Lenzner, T. Butz, Nucl. Instr. Meth. B 260 (2007) 419.
[27] R. Feder, F. Menzel, T. Butz. This proceedings.
[28] F. Menzel, D. Spemann, J. Lenzner, W. Böhlmann, G. Zimmermann, T. Butz, Nucl. Instr. Meth. B 267 (2009) 2321.
[29] F. Menzel, D. Spemann, J. Lenzner, W. Böhlmann, G. Zimmermann, T. Butz, Semiconductor Science and Technology 23 (2008) 125028.
[30] T. Andrea, M. Rothermel, T. Reinert, T. Koal, T. Butz. This proceedings.
[31] A. Arndt, D. Spoddig, P. Esquinazi, J. Barzola-Quiquia, S. Dusari, T. Butz, Phys. Rev. B 80 (2009) 195402.
[32] D.N. Jamieson, G.J.F. Legge, Nucl. Instr. Meth. B 34 (1988) 411.
[33] T. Reinert, N. Barapatre, A. Reinert, D. Spemann, T. Andrea, W. Larisch, Ch. Meinecke, T. Koal, R. Werner, M. Hohlweg, J. Vogt, T. Butz. This proceedings.

Bibliography

[Abb73] E. Abbe. Beiträge zur Theorie des Mikroskops und der mikroskopischen Wahrnehmung. *Archiv für Mikroskopische Anatomie* **9**, 413–418 (1873).

[And10] T. Andrea, M. Rothermel, R. Werner, T. Butz, T. Reinert. Limited angle STIM and PIXE tomography of single cells. *Nucl. Instr. and Meth. B* **268** (11-12), 1884–1888 (2010).

[Asc07] M. Aschner, T. R. Guilarte, J. S. Schneider, W. Zheng. Manganese: Recent advances in understanding its transport and neurotoxicity. *Toxicol. Appl. Pharmacol.* **221** (2), 131–147 (2007).

[Auz06] V. Auzelyte, F. Andersson, M. Elfman, P. Kristiansson, J. Pallon, M. Wegdén, C. Nilsson, N. Arteaga Marrero. On-line measurement of proton beam current in pA range. *Nucl. Instr. and Meth. B* **249** (1-2), 760–763 (2006).

[Aze09] F. A. C. Azevedo, L. R. B. Carvalho, L. T. Grinberg, J. M. Farfel, R. E. L. Ferretti, R. E. P. Leite, W. J. Filho, R. Lent, S. Herculano-Houzel. Equal numbers of neuronal and nonneuronal cells make the human brain an isometrically scaled-up primate brain. *J. Comp. Neurol.* **513** (5), 532–541 (2009).

[Bar00] L. Bartha, I. Uzonyi. Ion beam dose measurement in nuclear microprobe using a compact beam chopper. *Nucl. Instr. and Meth. B* **161-163**, 339–343 (2000).

[Bar07] N. Barapatre. *In-situ Trace Element Analysis of Neuromelanin*. Master's Thesis, Universität Leipzig, Leipzig (2007).

[Bar10] N. Barapatre, M. Morawski, T. Butz, T. Reinert. Trace element mapping in Parkinsonian brain by quantitative ion beam microscopy. *Nucl. Instr. and Meth. B* **268** (11-12), 2156–2159 (2010).

[Bea08] D. Beasley, I. Gomez-Morilla, N. Spyrou. Elemental analysis of hair using PIXE-tomography and INAA. *J Radioanal Nucl Chem* **276** (1), 101–105 (2008).

[Bec10] J. S. Becker. Bioimaging of metals in brain tissue from micrometre to nano-metre scale by laser ablation inductively coupled plasma mass spectrometry: State of the art and perspectives. *Int. J. Mass Spectrom.* **289** (2-3), 65–75 (2010).

[Bet30] H. Bethe. Zur Theorie des Durchgangs schneller Korpuskularstrahlen durch Materie. *Ann. Phys.* **397** (3), 325–400 (1930).

[Bet32] H. Bethe. Bremsformel für Elektronen relativistischer Geschwindigkeit. *Z. Physik* **76** (5-6), 293–299 (1932).

[Bil12] B. Bilgic, A. Pfefferbaum, T. Rohlfing, E. V. Sullivan, E. Adal-steinsson. MRI estimates of brain iron concentration in normal aging using quantitative susceptibility mapping. *NeuroImage* **59** (3), 2625–2635 (2012).

[Bis11] G. M. Bishop, T. N. Dang, R. Dringen, S. R. Robinson. Accumulation of non-transferrin-bound iron by neurons, astrocytes, and microglia. *Neurotox. Res.* **19** (3), 443–451 (2011).

[Blo33] F. Bloch. Zur Bremsung rasch bewegter Teilchen beim Durchgang durch Materie. *Ann. Phys.* **408** (3), 285–320 (1933).

[Boh13] N. Bohr. II. On the theory of the decrease of velocity of moving electrified particles on passing through matter. *Phil. Mag.* **25** (145), 10–31 (1913).

[Bur82] D. T. Burns. Robert Boyle (1627-1691): a foundation stone of Analytical Chemistry in the British Isles. Part I. Life and thought. *Anal. Proc.* **19** (5), 224 (1982).

[Bur99] J. R. Burdo, J. Martin, S. L. Menzies, K. G. Dolan, M. A. Romano, R. J. Fletcher, M. D. Garrick, L. M. Garrick, J. R. Connor. Cellular distribution of iron in the brain of the Belgrade rat. *Neuroscience* **93** (3), 1189–1196 (1999).

[But97] T. Butz, R.-H Flagmeyer. High energy ion microprobes: Where are we going? *MSF* **248-249**, 439–444 (1997).

[But00] T. Butz, R.-H Flagmeyer, J. Heitmann, D. N. Jamieson, G. J. F. Legge, D. Lehmann, U. Reibetanz, T. Reinert, A. Saint, D. Spemann, R. Szymanski, W. Tröger, J. Vogt, J. Zhu. The Leipzig high-energy ion nanoprobe: A report on first results. *Nucl. Instr. and Meth. B* **161-163**, 323–327 (2000).

[Cam90] J. L. Campbell, W. J. Teesdale, J.-X Wang. Accuracy of thick-target micro-PIXE analysis. *Nucl. Instr. and Meth. B* **50** (1-4), 189–196 (1990).

[Car59] A. Carlsson. The occurrence, distribution and physiological role of cat-echolamines in the nervous system. *Pharmacol. Rev.* **11**, 490–493 (1959).

[Che85] M. H. CHEN, B. CRASEMANN. Relativistic cross sections for atomic K- and L-shell ionization by protons, calculated from a Dirac-Hartree-Slater model. *At. Data Nucl. Data Tables* **33** (2), 217–233 (1985).

[Che89] M. H. CHEN, B. CRASEMANN. Atomic K-, L-, and M-shell cross sections for ionization by protons: A relativistic hartree-slater calculation. *At. Data Nucl. Data Tables* **41** (2), 257–285 (1989).

[Chu78] W.-K CHU, J. W. MAYER, M.-A NICOLET. *Backscattering spectrometry.* Academic Press, New York (1978).

[Coc32] J. D. COCKCROFT, E. T. S. WALTON. Experiments with high velocity positive ions. (I) Further developments in the method of obtaining high velocity positive ions. *Proc. R. Soc. A* **136** (830), 619–630 (1932).

[Dev01] G. DEVÈS, R. ORTEGA. Comparison of STIM and particle backscattering spectrometry mass determination for quantitative microanalysis of cultured cells. *Nucl. Instr. and Meth. B* **181** (1-4), 460–464 (2001).

[Dex89] D. T. DEXTER, F. R. WELLS, A. J. LEE, F. AGID, Y. AGID, P. JENNER, C. D. MARSDEN. Increased nigral iron content and alterations in other metal ions occurring in brain in Parkinson's disease. *J. Neurochem.* **52** (6), 1830–1836 (1989).

[Doo85] L. R. DOOLITTLE. Algorithms for the rapid simulation of Rutherford backscattering spectra. *Nucl. Instr. and Meth. B* **9** (3), 344–351 (1985).

[Dor07] E. R. DORSEY, R. CONSTANTINESCU, J. P. THOMPSON, K. M. BIGLAN, R. G. HOLLOWAY, K. KIEBURTZ, F. J. MARSHALL, B. M. RAVINA, G. SCHIFITTO, A. SIDEROWF, C. M. TANNER. Projected number of people with Parkinson disease in the most populous nations, 2005 through 2030. *Neurology* **68** (5), 384–386 (2007).

[Dri07] R. DRINGEN, G. M. BISHOP, M. KOEPPE, T. N. DANG, S. R. ROBINSON. The pivotal role of astrocytes in the metabolism of iron in the brain. *Neurochem. Res.* **32** (11), 1884–1890 (2007).

[Ehr60] H. EHRINGER, O. HORNYKIEWICZ. Verteilung von Noradrenalin und Dopamin (3-Hydroxytyramin) im Gehirn des Menschen und ihr Verhalten bei Erkrankungen des extrapyramidalen Systems. *Klin Wochenschr* **38** (24), 1236–1239 (1960).

[Fas06] M. FASANO, B. BERGAMASCO, L. LOPIANO. Is neuromelanin changed in Parkinson's disease? Investigations by magnetic spectroscopies. *J. Neural. Transm.* **113** (6), 769–774 (2006).

[Fed95] J. S. Fedorowich, J. C. Jain, R. Kerrich, V. Sopuck. Trace-element analysis of garnet by laser-ablation microprobe ICP-MS. *Can. Mineral.* **33** (2), 469–480 (1995).

[Fed05] H. Fedorow, F. Tribl, G. M. Halliday, M. Gerlach, P. Riederer, K. L. Double. Neuromelanin in human dopamine neurons: Comparison with peripheral melanins and relevance to Parkinson's disease. *Prog. Neurobiol.* **75** (2), 109–124 (2005).

[Foo06] Scientific Panel on Dietetic Products Nutrition Scientific Committee on Food, Allergies. *Tolerable upper intake levels for vitamins and minerals.* European Food Safety Authority, [Parma] (2006).

[Ges04] H. Gest. The discovery of microorganisms by Robert Hooke and Antoni van Leeuwenhoek, Fellows of The Royal Society. *Notes Rec. R. Soc. Lond.* **58** (2), 187–201 (2004).

[Gil05] Andrew Gillies (2005). Basal-ganglia-coronal-sections-large.png.
URL: *http://en.wikipedia.org/wiki/File:Basal-ganglia-coronal-sections-large.png* .

[Gol03] J. Goldstein, D. E. Newbury, D. C. Joy, C. E. Lyman, P. Echlin, E. Llfshin, L. Sawyer, J. R. Michael. *Scanning electron microscopy and X-ray microanalysis.* Springer, New York, 3rd Ed. (2003).

[Goo92] P. F. Good, C. W. Olanow, D. P. Perl. Neuromelanin-containing neurons of the substantia nigra accumulate iron and aluminum in Parkinson's disease: a LAMMA study. *Brain. Res.* **593** (2), 343–346 (1992).

[Göt04] M. E. Götz, K. L. Double, M. Gerlach, M. B. H. Youdim, P. Riederer. The relevance of iron in the pathogenesis of Parkinson's disease. *Ann. N.Y. Acad. Sci.* **1012** (1), 193–208 (2004).

[Gur] A. Gurbich. SigmaCalc.
URL: *http://www-nds.iaea.org/sigmacalc/* .

[Hal07] B. Halliwell, J. M. C. Gutteridge. *Free radicals in biology and medicine.* Oxford University Press, Oxford and New York, 4th Ed. (2007).

[Har01] R. C. Hardie. Phototransduction in *Drosophila melanogaster. J. Exp. Biol.* **204**, 3403–3409 (2001).

[Har02] C. D. Hardman, J. M. Henderson, D. I. Finkelstein, M. K. Horne, G. Paxinos, G. M. Halliday. Comparison of the basal ganglia in rats, marmosets, macaques, baboons, and humans: Volume and neuronal number for the output, internal relay, and striatal modulating nuclei. *J. Comp. Neurol.* **445** (3), 238–255 (2002).

[Hir88] E. Hirsch, A. M. Graybiel, Y. A. Agid. Melanized dopaminergic neurons are differentially susceptible to degeneration in Parkinson's disease. *Nature* **334** (6180), 345–348 (1988).

[Hir91] E. C. Hirsch, J.-P Brandel, P. Galle, F. Javoy-Agid, Y. Agid. Iron and aluminum increase in the substantia nigra of patients with Parkinson's disease: An X-ray microanalysis. *J. Neurochem.* **56** (2), 446–451 (1991).

[Hoo65] R. Hooke. *Micrographia: Or some physiological descriptions of minute bodies made by magnifying glasses with observations and inquiries thereupon.* Jo. Martyn & Ja. Allestry, London (1665).

[Ioz98] Renato V. Iozzo. Matrix Proteoglycans: From molecular design to cellular function. *Annu. Rev. Biochem.* **67** (1), 609–652 (1998).

[Iye89] G. V. Iyengar. *Elemental analysis of biological systems*, vol. 1. CRC Press, Boca Raton and Florida (1989).

[Jen03] P. Jenner. Oxidative stress in Parkinson's disease. *Ann. Neurol.* **53** (S3), S26–S38 (2003).

[Joh95] S. A. E. Johansson, J. L. Campbell, Malmqvist K. G. *Particle-induced x-ray emission spectrometry (PIXE)*, vol. 133 of *Chemical analysis.* John Wiley & Sons, Inc., New York (1995).

[Jon07] E. G. Jones (2007). Rattus Norvegicus, Whole-brain Nissl. URL: *http://brainmaps.org/index.php?action=viewslides&datid=94* .

[Jon09] A. R. Jones, Caroline C. Overly, S. M. Sunkin. The Allen Brain Atlas: 5 years and beyond. *Nat. Rev. Neurosci.* **10** (11), 821–828 (2009).

[Jon11] E. G. Jones, J. M. Stone, H. J. Karten. High-resolution digital brain atlases: a Hubble telescope for the brain. *Ann. N.Y. Acad. Sci.* **1225** (S1), E147–E159 (2011).

[Keu] M. C. Keuken. *Personal communication.*

[Kol08] D. Kolbe. *Rastertransmissions-Ionenmikroskopie einzelner lebender und fixierter Zellen.* Diplomarbeit, Universität Leipzig, Leipzig (2008).

[Kra79] Krause. M. O. Atomic radiative and radiationless yields for K and L shells. *J. Phys. Chem. Ref. Data* **8** (2), 307–327 (1979).

[Lai88] H. A. Laitinen. History of trace analysis. *J. Res. Natl. Bur. Stand.* **93** (3), 175 (1988).

[Lau06] L. M. L. de Lau, M. M. B. Breteler. Epidemiology of Parkinson's disease. *The Lancet Neurology* **5** (6), 525–535 (2006).

[Lla96] Y. Llabador, Ph Moretto. *Applications of nuclear microprobe in the life sciences: An efficient analytical technique for the research in biology and medicine.* World Scientific, Singapore and River Edge and NJ (1996).

[Lob06] R. Lobinski, C. Moulin, R. Ortega. Imaging and speciation of trace elements in biological environment. *Biochimie* **88** (11), 1591–1604 (2006).

[LS09] C. M. Long-Smith, A. M. Sullivan, Y. M. Nolan. The influence of microglia on the pathogenesis of Parkinson's disease. *Prog. Neurobiol.* **89** (3), 277–287 (2009).

[Lus00] A. J. Lusis. Atherosclerosis. *Nature* **407** (6801), 233–241 (2000).

[Mad04] N. R. Madamanchi. Oxidative stress and vascular disease. *Arterioscler. Thromb. Vasc. Biol.* (2004).

[Mar90] C. D. Marsden. Parkinson's disease. *The Lancet* **335** (8695), 948–952 (1990).

[Men07] F. Menzel, D. Spemann, S. Petriconi, J. Lenzner, T. Butz. Proton beam writing of submicrometer structures at LIPSION. *Nucl. Instr. and Meth. B* **260** (1), 419–425 (2007).

[Mer81] W. Mertz. The essential trace elements. *Science* **213** (4514), 1332–1338 (1981).

[Mer87] W. Mertz. *Trace elements in human and animal nutrition.* Academic Press Inc., San Diego, 5th Ed. (1987).

[Mey00] D. G. Meyers. The iron hypothesis:does iron play a role in atherosclerosis? *Transfusion* **40** (8), 1023–1029 (2000).

[MH05] C. Michelet-Habchi, S. Incerti, P. Aguer, Ph Barberet, E. Gontier, T. Guinefolleau, Ph Moretto, A. Pouthier, T. Pouthier, R.W Smith. 3D imaging of microscopic structures using a proton beam. *IEEE Trans. Nucl. Sci.* **52** (3), 612–617 (2005).

[Min07] R. Minqin, H. En, K. Beck, R. Rajendran, B. J. Wu, B. Halliwell, F. Watt, R. Stocker. Nuclear microprobe investigation into the trace elemental contents of carotid artery walls of apolipoprotein E deficient mice. *Nucl. Instr. and Meth. B* **260** (1), 240–244 (2007).

[Mor05] M. Morawski, T. Reinert, Ch Meinecke, T. Arendt, T. Butz. Antibody meets the microbeam – or how to find neurofibrillary tangles. *Nucl. Instr. and Meth. B* **231** (1-4), 229–233 (2005).

[Mor09] M. Morawski, A. Alpár, G. Brückner, A. Fiedler, C. Jäger, G. Gati, J. T. Stieler, T. Arendt. Chondroitin sulfate proteoglycan-based extracellular matrix in chicken (Gallus domesticus) brain. *Brain. Res.* **1275**, 10–23 (2009).

[Mou97] D. J. W. Mous, R. G. Haitsma, T. Butz, R.-H Flagmeyer, D. Lehmann, J. Vogt. The novel ultrastable HVEE 3.5 MV Singletron™ accelerator for nanoprobe applications. *Nucl. Instr. and Meth. B* **130** (1-4), 31–36 (1997).

[Nil07] C. Nilsson, S. Petriconi, T. Reinert, T. Butz. The new target chamber at LIPSION: The new translation stage and goniometer and the new irradiation platform for single cell experiments. *Nucl. Instr. and Meth. B* **260** (1), 71–76 (2007).

[NIM09] NIMR, MRC, Wellcome Images (2009). Drosophila melanogaster head, B0007686.
URL: *http://wellcomeimages.org/* .

[Ola99] C. W. Olanow, W. G. Tatton. Etiology and pathogenesis of Parkinson's disease. *Annu. Rev. Neurosci.* **22** (1), 123–144 (1999).

[Ola04] C. W. Olanow. The scientific basis for the current treatment of Parkinson's disease. *Annu. Rev. Med.* **55** (1), 41–60 (2004).

[Ort09] R. Ortega, G. Deves, A. Carmona. Bio-metals imaging and speciation in cells using proton and synchrotron radiation X-ray microspectroscopy. *J. R. Soc. Interface* **6** (Suppl_5), S649–S658 (2009).

[Pau89] H. Paul, J. Sacher. Fitted empirical reference cross sections for K-shell ionization by protons. *At. Data Nucl. Data Tables* **42** (1), 105–156 (1989).

[Pow00] S. R. Powell. The antioxidant properties of zinc. *J. Nutr.* **130** (5), 1447S–1454S (2000).

[Rei01a] T. Reinert. *Ionenstrahluntersuchungen am Gelenkknorpel: Energiedispersive Röntgenspektrometrie, Rückstreuspektrometrie und Transmissionsionenmikroskopie (PIXE, RBS, STIM).* Dissertation, Universität Leipzig, Leipzig (14.07.2001).

[Rei01b] L. T. Reiter, L. Potocki, S. Chien, M. Gribskov, E. Bier. A systematic analysis of human disease-associated gene sequences in drosophila melanogaster. *Genome Research* **11** (6), 1114–1125 (2001).

[Rei11] A. Reinert, N. Barapatre, S. Sachse, T. Reinert. Micro-PIXE for a Micro-Brain: The vinegar fly's brain, antenna, sensilla hairs and eye ion concentrations. *Nucl. Instr. and Meth. B* **269** (20), 2292–2296 (2011).

[Rhc]   Rhcastilhos. Brachiocephalic artery.
         URL: *http://en.wikipedia.org/wiki/File:Gray506.svg* .

[Rie89] P. Riederer, E. Sofic, W. D. Rausch, B. Schmidt, G. P. Reynolds,
         K. Jellinger, M. B. H. Youdim. Transition metals, ferritin, glutathione, and
         ascorbic acid in Parkinsonian brains. *J. Neurochem.* **52** (2), 515–520 (1989).

[Roi11] R. B. Roijers, N. Debernardi, J. P. M. Cleutjens, L. J. Schurgers,
         P. H. A. Mutsaers, G. J. van der Vusse. Microcalcifications in early
         intimal lesions of atherosclerotic human coronary arteries. *Am. J. Pathol.* **178**
         (6), 2879–2887 (2011).

[Ros99] R. Ross. Atherosclerosis — An inflammatory disease. *N. Engl. J. Med.* **340**
         (2), 115–126 (1999).

[Rot09] M. Rothermel, T. Butz, T. Reinert. Rearranging a nanoprobe: Line
         foci, grid shadow patterns and performance tests. *Nucl. Instr. and Meth. B* **267**
         (12-13), 2017–2020 (2009).

[Rot10] M. Rothermel, T. Reinert, T. Andrea, T. Butz. First results on ion
         micro-tomography at LIPSION. *Nucl. Instr. and Meth. B* **268** (11-12), 2001–2005
         (2010).

[Rya95] C. G. Ryan, D. N. Jamieson, C. L. Churms, J. V. Pilcher. A new
         method for on-line true-elemental imaging using PIXE and the proton micro-
         probe. *Nucl. Instr. and Meth. B* **104** (1-4), 157–165 (1995).

[Rya00] C. G. Ryan. Quantitative trace element imaging using PIXE and the nuclear
         microprobe. *Int. J. Imaging Syst. Technol.* **11** (4), 219–230 (2000).

[Rya01] C. G. Ryan. Developments in Dynamic Analysis for quantitative PIXE true
         elemental imaging. *Nucl. Instr. and Meth. B* **181** (1-4), 170–179 (2001).

[Rya10] C. G. Ryan, R. Kirkham, D. P. Siddons, P. A. Dunn, J. S. Laird,
         A. Kuczewski, G. Moorhead, G. de Geronimo, P. Davey, M. Jensen,
         D. J. Paterson, M. D. de Jonge, D. L. Howard, R. M. Hough. The Maia
         384 detector array in a nuclear microprobe: A platform for high definition PIXE
         elemental imaging. *Nucl. Instr. and Meth. B* **268** (11-12), 1899–1902 (2010).

[Sah01] B. Sahin, H. Aslan, B. Unal, S. Canan, S. Bilgic, S. Kaplan,
         L. Tumkaya. Brain volumes of the lamb, rat and bird do not show hemispheric
         asymmetry: A stereological study. *Image Anal. Stereol.* **20** (1), 9–13 (2001).

[Sak97] A. Sakellariou, M. Cholewa, A. Saint, G. J. F. Legge. An accurate
         reconstruction algorithm for tomography experiments that involve complex probe
         - sample interactions. *Meas. Sci. Technol.* **8** (7), 746–758 (1997).

[Sic12] A. Sickert, N. Barapatre, M. Rothermel, D. Teupser, T. Reinert. 3d analysis of an induced atherosclerotic lesion in a murine artery by PIXE stacking. *Int. J. PIXE* **22** (01n02), 81–86 (2012).

[Spe03] D. Spemann, T. Reinert, J. Vogt, J. Wassermann, T. Butz. Active compensation of stray magnetic fields at LIPSION. *Nucl. Instr. and Meth. B* **210**, 79–84 (2003).

[Sta92] H. C. Stary, D. H. Blankenhorn, A. B. Chandler, S. Glagov, W. Insull, M. Richardson, M. E. Rosenfeld, S. A. Schaffer, C. J. Schwartz, W. D. Wagner. A definition of the intima of human arteries and of its atherosclerosis- prone regions. A report from the Committee on Vascular Lesions of the Council on Arteriosclerosis, American Heart Association. *Arterioscler. Thromb. Vasc. Biol.* **12** (1), 120–134 (1992).

[Sta94] H. C. Stary, A. B. Chandler, S. Glagov, J. R. Guyton, W. Insull, M. E. Rosenfeld, S. A. Schaffer, C. J. Schwartz, W. D. Wagner, R. W. Wissler. A definition of initial, fatty streak, and intermediate lesions of atherosclerosis. A report from the Committee on Vascular Lesions of the Council on Arteriosclerosis, American Heart Association. *Arterioscler. Thromb. Vasc. Biol.* **14** (5), 840–856 (1994).

[Sta95] H. C. Stary, A. B. Chandler, R. E. Dinsmore, V. Fuster, S. Glagov, W. Insull, M. E. Rosenfeld, C. J. Schwartz, W. D. Wagner, R. W. Wissler. A definition of advanced types of atherosclerotic lesions and a histological classification of atherosclerosis A report from the Committee on Vascular Lesions of the Council on Arteriosclerosis, American Heart Association. *Arterioscler. Thromb. Vasc. Biol.* **15** (9), 1512–1531 (1995).

[Sta00] H. C. Stary. Natural history of calcium deposits in atherosclerosis progression and regression. *Z. Kardiol.* **89** (14), S028–S035 (2000).

[Sta04] N. Stadler, R. A. Lindner, Davies M. J. Direct detection and quantification of transition metal ions in human atherosclerotic plaques: Evidence for the Presence of Elevated Levels of Iron and Copper. *Arterioscler. Thromb. Vasc. Biol.* **24** (5), 949–954 (2004).

[Sta12] N. Stadler, S. Heeneman, S. Vöö, N. Stanley, G. I. Giles, B. P. Gang, K. D. Croft, T. A. Mori, V. Vacata, M. J.A.P Daemen, J. Waltenberger, Davies M. J. Reduced metal ion concentrations in atherosclerotic plaques from subjects with Type 2 diabetes mellitus. *Atherosclerosis* **222** (2), 512–518 (2012).

[Sti05] A. I. Stijn (2005). Anatomy artery.
URL: *http://de.wikipedia.org/wiki/Arterie* .

[Str]   David Strutt, Wellcome Images. Drosophila melanogaster adult eye, B0001865.
          URL: *http://wellcomeimages.org/* .

[Sul81]   J. L. Sullivan. Iron and the sex difference in heart disease risk. *The Lancet* **317** (8233), 1293–1294 (1981).

[Szy97]   R. Szymanski, D. N. Jamieson. Ion source brightness and nuclear microprobe applications. *Nucl. Instr. and Meth. B* **130** (1-4), 80–85 (1997).

[Teu03]   D. Teupser, A. D. Persky, J. L. Breslow. Induction of atherosclerosis by low-fat, semisynthetic diets in LDL receptor-deficient C57BL/6J and FVB/NJ mice: Comparison of lesions of the aortic root, brachiocephalic artery, and whole aorta (en face measurement). *Arterioscler. Thromb. Vasc. Biol.* **23** (10), 1907–1913 (2003).

[Tri09]   F. Tribl, E. Asan, T. Arzberger, T. Tatschner, E. Langenfeld, H. E. Meyer, G. Bringmann, P. Riederer, M. Gerlach, K. Marcus. Identification of L-ferritin in neuromelanin granules of the human substantia nigra: A targeted proteomics approach. *Mol. Cell. Proteomics* **8** (8), 1832–1838 (2009).

[Val05]   M. Valko, H. Morris, M. T.D Cronin. Metals, toxicity and oxidative Stress. *Curr. Med. Chem.* **12** (10), 1161–1208 (2005).

[Wat88]   F. Watt, G. W. Grime, C. C. Perry. The damage effects of a 1 micron proton beam on a single pollen grain. *Nucl. Instr. and Meth. B* **30** (3), 331–336 (1988).

[Wat97]   F. Watt, P. S. P. Thong, A. H. M. Tan, S. M. Tang. Nuclear microscopy of single whole cultured cells: Beam damage studies. *Nucl. Instr. and Meth. B* **130** (1-4), 188–191 (1997).

[Wat06]   F. Watt, R. Rajendran, M. Q. Ren, B. K. H. Tan, B. Halliwell. A nuclear microscopy study of trace elements Ca, Fe, Zn and Cu in atherosclerosis. *Nucl. Instr. and Meth. B* **249** (1-2), 646–652 (2006).

[Wei08]   R. Weissleder, M. J. Pittet. Imaging in the era of molecular oncology. *Nature* **452** (7187), 580–589 (2008).

[Wer09]   R. Werner. *Confined cell growth in structured Petri dishes fabricated by proton beam writing (in agar) and major energy resolution improvements in detectors.* Diploma Thesis, Universität Leipzig, Leipzig (2009).

[Wes05]   J. B. West. Robert Boyle's landmark book of 1660 with the first experiments on rarified air. *J. Appl. Physiol.* **98** (1), 31–39 (2005).

[WS11] F. Wolfe-Simon, J. S. Blum, T. R. Kulp, G. W. Gordon, S. E. Hoeft, J. Pett-Ridge, J. F. Stolz, S. M. Webb, P. K. Weber, P. C. W. Davies, A. D. Anbar, R. S. Oremland. A bacterium that can grow by using arsenic instead of phosphorus. *Science* **332** (6034), 1163–1166 (2011).

[YI11] J. R. Yates III. A century of mass spectrometry: from atoms to proteomes. *Nat. Meth.* **8** (8), 633–637 (2011).

[Yua03] X.-M Yuan, W. Li. The iron hypothesis of atherosclerosis and its clinical impact. *Ann. Med.* **35** (8), 578–591 (2003).

[Zec02] L. Zecca, R. Fariello, P. Riederer, D. Sulzer, A. Gatti, D. Tampellini. The absolute concentration of nigral neuromelanin, assayed by a new sensitive method, increases throughout the life and is dramatically decreased in Parkinson's disease. *FEBS Letters* **510** (3), 216–220 (2002).

[Zec03] L. Zecca, F. A. Zucca, H. Wilms, D. Sulzer. Neuromelanin of the substantia nigra: a neuronal black hole with protective and toxic characteristics. *Trends Neurosci.* **26** (11), 578–580 (2003).

[Zec04] L. Zecca, M. B. H. Youdim, P. Riederer, J. R. Connor, R. R. Crichton. Iron, brain ageing and neurodegenerative disorders. *Nat. Rev. Neurosci.* **5** (11), 863–873 (2004).

[Zie85] J. F. Ziegler. *The stopping and range of ions in matter*, vol. 2-6. Pergamon Press, New York (1977-1985).

List of Publications

The following research papers have been published during the course of this work in scientific journals.

1. N. Barapatre, M. Morawski, T. Reinert. Quantification and localisation of trace elements in Parkinsonian brain: a proton beam microscopy study. *Journal of Neurochemistry* **110**s1, 71 (2009).

2. N. Barapatre, M. Morawski, T. Butz, T. Reinert. Trace element mapping in Parkinsonian Brain by quantitative ion beam microscopy. *Nucl. Instr. and Meth. B* **268**, 2156–2159 (2010).

3. T. Reinert, T. Andrea, N. Barapatre, M. Hohlweg, T. Koal, W. Larisch, A. Reinert, D. Spemann, J. Vogt, R. Werner, T. Butz. Biomedical Research at LIPSION - Present State and Future Developments. *Nucl. Instr. and Meth. B* **269**, 2254–2259 (2011).

4. D. Spemann, T. Reinert, J. Vogt, T. Andrea, N. Barapatre, R. Feder, A. M. Jakob, N. Liebing, Ch. Meinecke, F. Menzel, M. Rothermel, T. Butz. Materials analysis and modification at LIPSION - Present state and future developments. *Nucl. Instr. and Meth. B* **269**, 2175–2179 (2011).

5. A. Reinert, N. Barapatre, S. Sachse, T. Reinert. PIXE for a Brain: The Vinegar Fly's Brain, Antenna, Sensilla Hairs and Eye Ion Concentrations. *Nucl. Instr. and Meth. B* **269** (20), 2292–2296 (2011).

6. A. Sickert, N. Barapatre, M. Rothermel, D. Teupser, T. Reinert. 3D Analysis of an Induced Atherosclerotic Lesion in a Murine Artery by PIXE Stacking. *Int. J. PIXE* **22** (01n02), 81–86 (2012).

Acknowledgement

to be with the fellow Ph.D. students in InterNeuro.

Above all, I'm highly indebted to my family for their unrelenting support and courage. They have left no stone unturned in order to give me the best education possible. I'm deeply grateful to my wife, Imon, for standing by me through thick and thin and for all the love and care.

I dearly miss my father-in-law Mr. Kalyan Bose, whose untimely death during the course of this work robbed us of this moment that I was eagerly looking forward to share with him.

Declaration of Authorship

I certify that the work presented here is, to the best of my knowledge and belief, original and the result of my own research work, except as acknowledged.

Curriculum vitae

Name:	Nirav Dinkar Barapatre
Date of birth:	15.03.1982
Place of birth:	Ahmedabad
Marital status:	married
Nationality:	India

Education:

1987 – 1992	Best Primary School, Ahmedabad
	Kendriya Vidyalaya, Suratgarh
	Kendriya Vidyalaya, Ahmedabad
1992 – 1999	Sainik School Balachadi, Jamnagar
1999	Completion of Higher Secondary School
1999 – 2002	B. Sc. in Physics, St. Xavier's College,
	Gujarat University, Ahmedabad
2002 – 2003	German Language Course, Goethe Institut, Pune
2003 – 2007	M. Sc. in Physics, University of Leipzig
2007	Master's thesis
	"In situ Trace Elements Analysis of Neuromelanin"
	in the Nuclear Solid State Physics group of
	Prof. Dr. T. Butz, University of Leipzig
2007 – 2008	Junior Researcher
	in the Nuclear Solid State Physics group of
	Prof. Dr. T. Butz, University of Leipzig
2008 – 2011	Doctoral Fellow in the Research Training Network
	InterNeuro, University of Leipzig, funded by DFG.
since 2007	Ph.D. student at the University of Leipzig

Leipzig, 07. June 2013